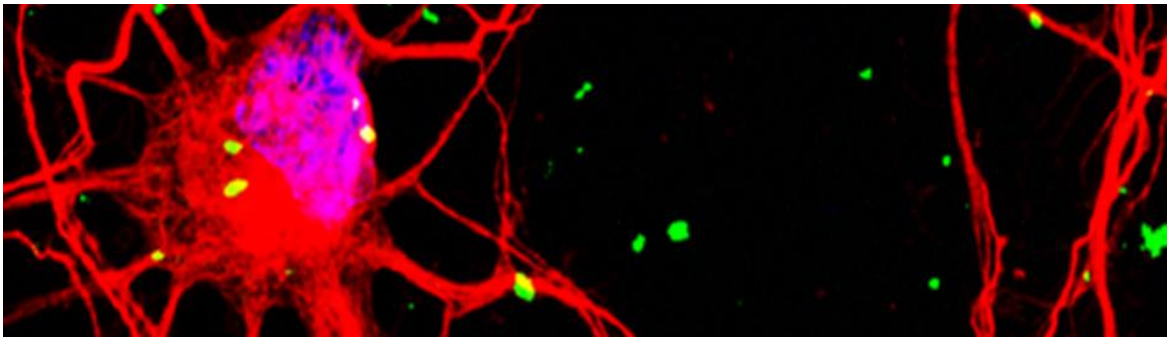

# Corso di Dottorato in Neuroscienze
# Curriculum Neuroscienze e Neurotecnologie
# Ciclo XXX

# Impact of graphene nanosheets on primary astrocytes

**Candidate: Martina Chiacchiaretta**
**Supervisors: Fabio Benfenati**
**Fabrizia Cesca**
**Mattia Bramini**

ISTITUTO ITALIANO DI TECNOLOGIA

UNIVERSITÀ DEGLI STUDI DI GENOVA

# Table of contents

# 1. SUMMARY

Graphene (G) has the potential to make a very significant impact on society, with new interesting and beneficial applications for both individuals and industrial organizations. The emerging interest toward applying G-based nanomaterials within the central nervous system (CNS) prompted us to focus our attention on the toxicity and biocompatibility of G nanostructures in contact with primary neuronal and glial cells. In this work we describe the interaction between G nanosheets and primary cortical astrocytes, which are key players in maintaining brain homeostasis, by exploring: (i) the molecular mechanisms of G nanosheets internalization, (ii) the changes in proteomic and lipidomic composition of G-treated cultures, (ii) the effects of G exposure on cell morphology and physiology and (iv) the indirect effects of G-exposed astrocytes on neuronal cells, in an astrocyte-neuron co-culture system.

Primary astrocytes were exposed to pristine graphene (GR) and graphene oxide (GO) nanosheets at 2 concentrations (1 and 10 μg/ml) for 24, 48 and 72 h; exposed and control cultures were investigated combining different techniques ranging from cell biology to microscopy, electrophysiology, and "omics" approaches. Our results show that, although GR and GO nanosheets exposure did not affect cell viability, it did nevertheless cause morphological and physiological changes, including: i) alteration of cell shape due to disruption of cytoskeleton, ii) up-regulation of Kir 4.1 channels and glutamate uptake, iii) dysregulation of calcium homeostasis, iv) alteration of the expression level of proteins involved in fundamental cellular pathways, like neural development, metabolism, and trafficking, and v) variation of lipid content. Moreover, G-

induced dysregulation of astrocyte physiology has an impact on the physiology of co-cultured neuronal cells.

Altogether, these results raise some concern on the safety of G nanosheets for future bio-applications, especially in the biomedical field. In this scenario, a detailed comprehension of the mechanisms controlling the interaction between G and CNS is mandatory, in the perspective of adopting this material for neuro-medical implants.

# 2. INTRODUCTION

## 2.1 What is graphene? From its discovery to mass-production.

G is a single- or few-layered sheet of $sp^2$ hybridized carbon atoms covalently bonded to three other atoms arranged in a honeycomb lattice, with a thickness of only 0.34 nm. G was firstly isolated in 2004 by Drs. Geim and Novoselov in Manchester. They described and characterized a monocrystalline graphitic film obtained by a simple "scotch-tape method", winning the Nobel prize in physics in 2010 for their groundbreaking work [1]. The method consisted in the repetitive mechanical exfoliation of graphite using adhesive tape, followed by pressing the tape against a substrate to obtain single or few layers of carbon atoms. Its unique structure endows G with a number of extraordinary properties: G is the thinnest compound ever known at one atom thick (a million times thinner than a human hair), the strongest compound discovered (between 100-300 times stronger than steel), it is light, transparent and flexible. It is extremely electrically and thermally conductive, which opens the possibility of using G in a broad spectrum of applications in electronics, optoeletronics, energy storage, medicine and environmental safety [2-4].

Since its discovery, the interest for G has increased exponentially in several scientific fields, with a high number of scientific publications per day reporting the general term "graphene". It is therefore necessary to precisely catalog the components of the "G family", since two-dimensional carbon materials with significant variations in layer number, lateral dimension, rotational faulting and chemical modification have been included under the same name (**Figure 1**)[5]. Materials made of no more than 10 layers, termed few layer graphene (layer numbers from 2 to about 5, FLG) and multi layer graphene (layer numbers between 2 and about 10, MLG) can be classified as graphene

related materials (GRMs). In addition to the number of layers, the proper nomenclature of GRMs should include the specification of the chemical modifications, i.e. graphene oxide (GO) and reduced graphene oxide (rGO), and of the lateral dimensions, i.e. G nanosheets if one dimension is less than 100 nm, graphene microsheets if in a range between 100 nm and 100 µm, and graphene quantum dots (GQDs) if less than 10 nm.

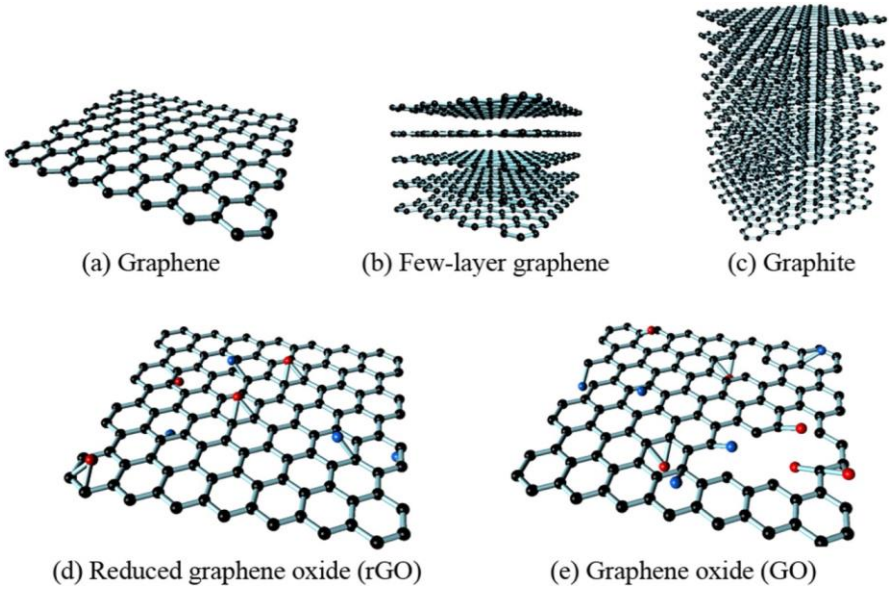


**Figure 1**. **Representative scheme of GRMs.** Modified from Kiev et al. [6].

The achievement of low cost and high yield production of G is still a major challenge. So far, depending on the final application of the material, the various synthesis methods can be categorized in: i) liquid phase and thermal exfoliation [7], ii) chemical vapor deposition (CVD) [8] and iii) synthesis on silicon carbide (Sic) substrates [9] (**Figure 2**). The process of liquid and thermal phase exfoliation consists in the ultrasonic exfoliation of graphite by solvent or thermal shock to obtain a single layer of G in suspension; in addition for G oxide production, graphite is firstly oxidized and then subjected to exfoliation. This technique has been applied for research purposes, in

particular G-based paints and inks are suitable for printable electronics [10] or biomedical applications, such as tissue engineering and regenerative medicine [11]. In the CVD process, a uniform G film is deposited on a surface of interest through a catalytic reaction between hydrocarbon gases and catalytic metal substrates. This method is suitable for applications in photonics, nanoelectronics [12] and for development of transparent biosensors and scaffolds to promote cells growth [4]. Finally, the synthesis of G on silicon carbide substrates is limited for *niche* applications like the manufacturing of high-frequency transistors and other advanced electronic devices [13].

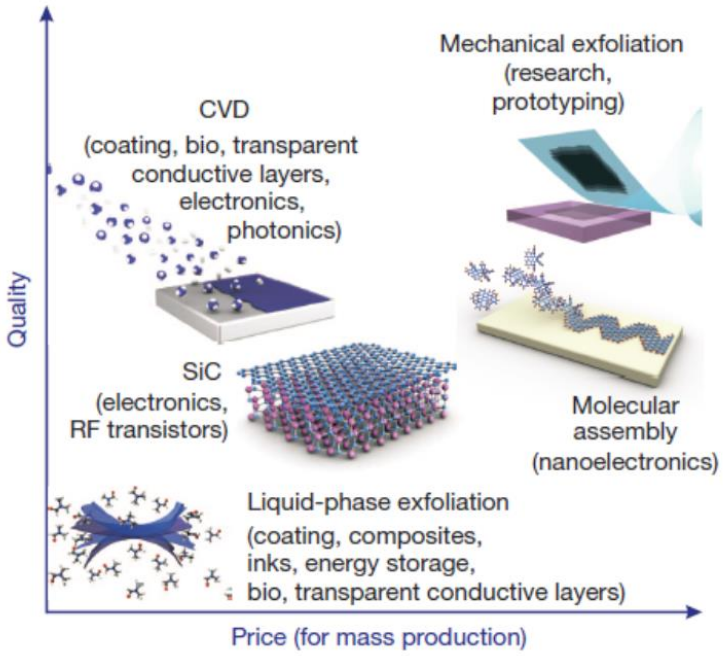


**Figure 2. Methods of mass-production of G for different purposes.** Modified from Novoselov et al. [2].

## 2.2 Biomedical applications: interfacing graphene with the central nervous system.

The central nervous system (CNS) is composed of two main cellular populations, neurons and glial cells, the latter category including astrocytes, microglia, pericytes and oligodendrocytes. Each cell type has specific functions and all together they contribute to maintain the homeostasis of CNS. Perturbations of any single component at the cellular and molecular level would disrupt this perfect equilibrium, leading to CNS pathologies. Traditional treatments for CNS disorders present a number of challenges; in this context, nanotechnology has emerged as a promising alternative for treating neurological diseases. Because of all its extraordinary properties, G has attracted attention for applications in the field of neurology. Possible applications of G and G-based materials include (i) the delivery to the brain of drugs/genes usually rejected by the blood-brain barrier (BBB), (ii) tissue engineering, as interfacing two (2D) or three dimensional (3D) G scaffolds with neural cells could be extremely advantageous for exploring and stimulating their electrical behavior to facilitate neuronal regeneration, and (iii) cell labeling and real-time monitoring of biological active molecules. All these points will be described in detail in the next paragraphs.

However, interfacing G with the CNS requires a preliminary detailed toxicity profile both *in vitro* and *in vivo*. In particular, specific characteristics of G materials are known to influence its toxicity, such as its concentration, lateral dimension, charge and surface structure of the nanosheets [14, 15].

### *2.2.1 Graphene for drug and gene delivery.*

One attractive possibility is to employ G for the therapeutic delivery of drugs that are usually rejected by the blood-brain barrier (BBB), loading cargoes to G via π-π stacking interactions, hydrogen bonding, or hydrophobic interactions [16]. To date, GO nanosheets are preferred with respect to GR nanosheets because of their major solubility and stability in biological fluids [17]. Moreover, the possibility to be functionalized with polyethylene glycol (PEG), poli(ε-caprolactone) (PCL), pluronic, amine, carboxyl and dextran groups to decrease toxicity and increase biocompatibility is a further advantage [18, 19].

Once injected intravenously, G can reach various locations through the bloodstream, and some side effects have to be taken into consideration because of the interaction with the biological environment. The interactions of G nanosheets with ions, salts and proteins result in the aggregation of the nanomaterial and in the formation of a protein corona that affects the biodistribution of the material and often triggers an inflammatory response [20]. Nanosheets can be phagocytosed by macrophages, inducing activation and release of pro-inflammatory cytokines [21], and interact with several blood components inducing haemolysis [22]. Last but not least, nanosheets could accumulate in the reticulo-endothelial system rather than in the tissue to which they are targeted [23].

Furthermore, crossing biological barriers is still a major concern. Particularly challenging is the passage through the BBB, that significantly limits the delivery of drugs, blocking ~100% of large-molecule neuro-therapeutics and more than 98% of all small-molecule drugs [24]. An ideal method for transporting drugs across the BBB would deliver molecules in a controlled and targeted way, additionally avoiding any damage to

the barrier. Accordingly to Mendonca et al., systemically injected rGO nanosheets crossed the BBB through a transitory decrease in the BBB paracellular tightness and accumulated in the thalamus and hippocampus of rats [25]. On the contrary, functionalization of rGO with polyethylene glycol (PEG) usually used to improve biocompatibility of nanoparticles, induced BBB breakdown and astrocyte dysfunctions *in vivo* [26]. Recently, Xiao et al. used GQDs conjugated to a neuroprotective peptide. Once injected intravenously (i.v.) in murine model of Alzheimer disease (AD), they increased learning and memory, dendritic spines formation, and decreased pro-inflammatory cytokine levels [27]. In addition, new approaches have been developed to target brain parenchyma overcoming the BBB. In a recent study, an innovative nano-delivery system has been investigated, with high loading capacity and a pH dependent behavior. Researchers created GO@$Fe_3O_4$ nanocomposites conjugated to lactoferrin (Lf), an iron-transporting serum glycoprotein that binds to receptors overexpressed at the surface of glioma cells and vascular endothelial cell of the BBB, in order to obtain Lf@GO@$Fe_3O_4$. Doxycycline, a drug used to treat glioma, was loaded on the surface of G by π-π stacking, creating Lf@GO@$Fe_3O_4$@DOX. *In vitro* studies of cytotoxicity and cellular uptake demonstrated that this system could be a suitable tool for drug delivery, as it is able to specifically target glioma cells [28].

All together, the aforementioned works provide good prospects for the development of G-based nanocarriers for drug delivery applications, keeping in mind that the biocompatibility and nanosafety of the material within the CNS has to be carefully evaluated in detail before thinking of applying this system to human patients.

Thanks to its high surface area, G can be loaded with both single-stranded DNA and RNA through hydrophobic and π–π stacking interactions, which makes it an extremely good candidate also for gene delivery [29]. Different strategies have been developed to optimize G as gene delivery platform. These include: the decoration with positively charged polymers (PEI, BPEI), dendrimers (PAMAM) and polysaccharides, which enhance gene transfection efficiency by promoting the interaction with the cell membrane and the electrostatic interactions with nucleic acids [30, 31]; the pegylation, previously demonstrated to enhance stability, biocompatibility and biodistribution of G *in vivo* [32]; functionalization with cell-penetrating peptides to enhance transfection efficiency [33]; combination with gold nanoparticles (AuNP) and gold nanorods (AuNr) to increase aqueous dispersibility and to improve photothermal effects upon NIR irradiation [34]; and functionalization with tumor specific cleavable linkers, in order to target specific types of tumors [35]. Unfortunately, to date very few studies successfully demonstrated therapeutic G-mediated gene delivery *in vivo*. Notably, Paul et al. developed a hydrogel able to release PEI-GO/pDNA$^{VEGF}$ complexes, to delivery vascular endothelial growth factor (VEGF) *in vitro* and successfully *in vivo* in a rat model of myocardial infarction [30]. In another interesting work, Choi et al. fabricated an mRNA delivery system employing GO-PEI to target iPS cells [36].

In conclusion, viral vectors still remain the most efficient tool for gene delivery. Nevertheless, the development of non-viral systems might allow overcoming some limitations, such as the difficulties in accommodating long nucleic acids, batch-to-batch variations, elevated costs and the immunogenicity of viral vector systems. G-mediated gene delivery is indeed a promising approach to overcome these issues, however most of

the published studies are limited to *in vitro* models, and the *in vivo* validation of this system is strongly awaited.

### *2.2.2 Graphene-based materials for tissue engineering and regenerative medicine*

Tissue engineering aims to restore and improve the disrupted functions of a tissue or an organ by interfacing them with suitable bioengineered materials. Active and dynamic implantable devices are extremely advantageous for both stimulating and recording electrical activity of neural cells. Researchers have developed various classes of implantable devices used as neural interfaces, including deep brain stimulation implants (DBI) for the electrical stimulation of deep structures in the brain, clinically used to treat dystonia and tremor in Parkinson disease [37], retinal and cochlear implants to electrically stimulate the surviving neurons in presence of retinal disease or to convert external sounds in electrical impulses [38, 39], central and peripheral nervous system stimulators, promising for motor rehabilitation after spinal cord lesions [40], and intracranial electrodes to map brain electrical activity, which are used for diagnostic purposes [41] (**Figure 3**).

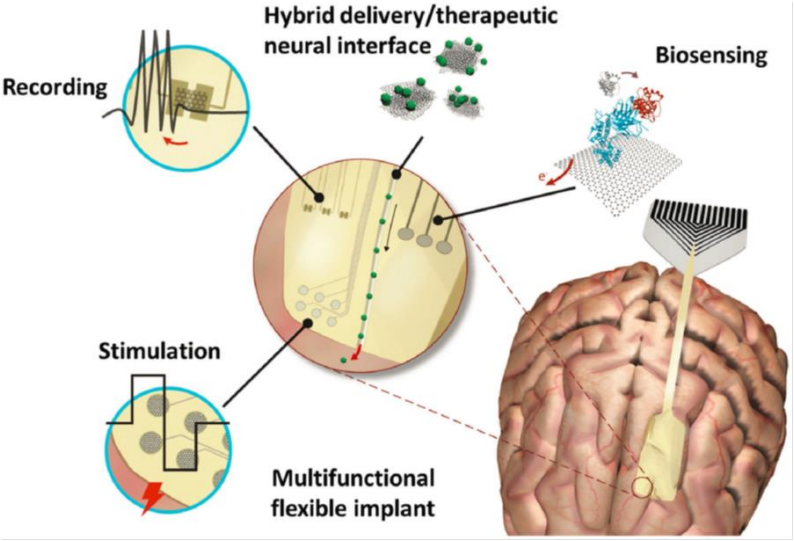


**Figure 3. G based neural interfaces for a variety of functionalities like recording, stimulation and biosensing.** Modified from Kostarelos et al. [4].

The intrinsic properties of G can be exploited to design G-based devices for neural interfaces. Fundamental requirements for a good neural implant are: i) biocompatibility with minimal inflammatory response, ii) adequate signal-to-noise ratio (SNR) and iii) minimal invasiveness, respecting tissue integrity. To date, *in vivo* studies demonstrate that G electrodes can stimulate and record neural activity, to map brain functions and implement neural prosthetics. Recently, Kuzum et al. [42] developed a flexible, low noise G electrode for simultaneous electrophysiology and imaging recording *in vivo*. After bicuculline injection to evoke epileptiform activity, it was possible to record simultaneously from rat cortical hemispheres with G-electrodes and Au-electrodes of the same size. G electrodes displayed 6 times lower SNR with respect to Au-electrodes, suggesting that the adoption of the new G-based recording system could offer clear advantages for studying brain electrical activity. In addition, thanks to the

transparency of G electrodes, it was possible to simultaneously image the cortical area, combining *in vivo* two-photon imaging and cortical electrophysiological recording [42].

A further progress has been achieved by developing G field effect transistors (G-FETs), which allow signal amplification, reducing external noise. Exploiting these advantages, Veliev et al. [43] reported the fabrication of G-FETs on various substrates. They detected *in vitro* spontaneous activity of hippocampal neurons grown on top of the G sensors, with high sensitivity and low noise level [43]. Additionally, Blaschke et al. [44] successfully demonstrated the recording of *in vivo* brain activity of rats using G-FETs. The researchers were able to record LFP during spontaneous slow oscillations, visually evoked activity, and pharmacologically-induced pre-epileptic spikes, with good biocompatibility, high spatial resolution and SNR, confirming the results obtained by *in vitro* studies and bringing an advance in G-based neural interface devices (**Figure 4**) [44].

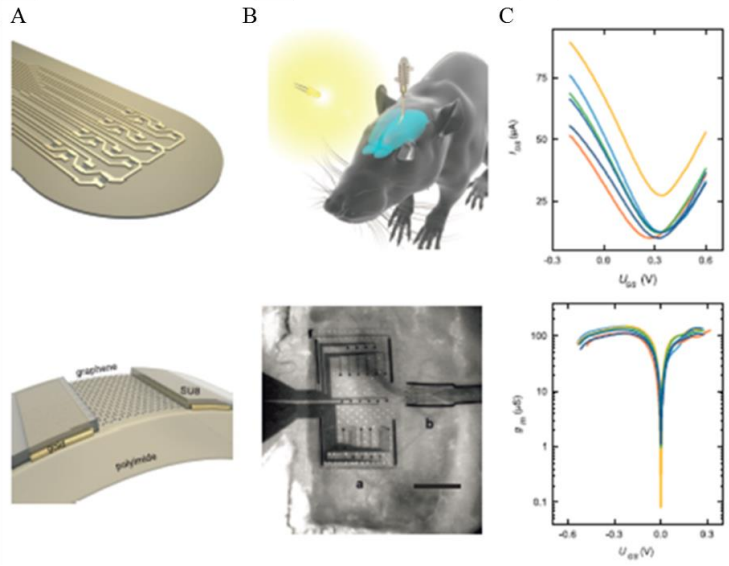


**Figure 4. Flexible G microtransitors to record brain activity. A.** Representation of the G implant. **B.** Representation of the implant located on the surface of the rat brain. **C.** Characterization of the device. Taken from Blaschke et al. [44].

### *2.2.3 Bioimaging and biosensing*

G materials have also been employed for bioimaging applications as imaging contrast agents due to their intrinsic fluorescent emission, raman scattering, and near infrared spectroscopy (NIR) absorbance [45], as carriers of dyes, like Cy5, Cy7, IRDye 800 and fluorescein [46], and as fluorescence quenchers *via* fluorescence resonance energy transfer (FRET) or charge transfer [47, 48]. Remarkably, the unique structure and optical properties of GQDs make them the most used G materials for cell and tissue imaging [49]. GQDs usually show typical absorption bands in the UV region, with a range of emission from ultraviolet to near-infrared, depending on the size and specific functionalization of the material [45]. A number of studies report good labeling of different cell types *in vitro* [50]; moreover, functionalization of GQDs with poly (l-lactide) PLA and PEG allow intracellular imaging of miRNA combined with gene delivery [51]. However, *in vivo* imaging presents many challenges due to autofluorescence of tissues and light scattering effects and until now the fluorescent signal of GQDs in deep tissues or organs has been neither detected nor demonstrated.

The fluorescence quenching ability of GO has been expoited to develop biosensors able to detect dye-labeled ssDNA [52]. Interestingly, the interaction between GO and dye-labeled ssDNA allows to quench the fluorescence of the fluorophor, making this tecnique suitable for sensing molecules like glucose [53]. Glucose detection is also possible through a G-based enzymatic reaction: the covalent attachment of the amine of glucose oxidase to the carboxylic groups of GO creates a biosensor able to detect glucose levels [54]. In addition, also NADH, cholesterol, cytocrome C, hemoglobin, $H_2O_2$ and other analytes could be detected by G-based enzymatic and non-enzymatic reactions [55].

Of note, G-based biosensors have been developed for detection of neurotrasmitters, exemplified in the work of Hess et al., in which enzyme-modified G FETs were developed to detect acethylcholine, a neurotrasmitter in CNS and PNS [56]. In a similar work, functionalized G was used for the detection of dopamine [57]. To conclude, different promising strategies have already been succesfully explored, especially in *in vitro* systems; however further studies are necessary to test and make this technologies working *in vivo.*

## 2.3 Toxicity of graphene materials in the central nervous system.

### *2.3.1 Characterization of graphene materials*

The determination of the common mechanisms of G toxicity when in contact with biological systems is still a major challenge, as multiple parameters that are specific for each G material have to be taken into account. The Graphene Flagship programme, a 10 year European project, was set up with the purpose to coordinate G research among European universities, research centers and companies, bringing together academic and industrial researchers. One of the main aims of the flagship is to reveal correlations between the material structure and its toxicological effects. So far, the biological correlation of G properties such as layer number, lateral dimension, surface chemistry, surface volume/ratio, and material purity has already been analyzed on different cell types [58]. The layer number determines the thickness, the specific surface volume/ratio, and bending elasticity. From a biological point of view, the absorption capacity of

biological molecules increases significantly as the surface/volume ratio increases. For monolayer G, the surface/volume ratio is maximized, due to atoms lying on its surface and exposed to the surrounding medium; by contrary, the increase in layer number leads to a reduction in surface volume/ratio, which in turn decreases the adsorption capacity of the material. Of note, as the lateral size of G ranges from the nanoscale to the microscale (i.e., 10 nm up to >20 μm), it is crucial to specify the lateral dimension of each sample to be able to predict its biological effects. Furthermore, it has been demonstrated that NPs with diameter size <100 nm can easily enter the cell, NPs <40 nm can enter nucleus, and if <35 nm may cross the blood-brain barrier [59]. Another fundamental parameter to take into consideration is the surface chemistry, being GR and GO extremely different in their surface hydrophobicity/hydrophilicity. GR surface is hydrophobic, while GO presents hydrophobic islands as well as hydrophilic regions, which confers the material highly dispersibility in biological media due to the presence of oxygenated functional residues like epoxide, carboxyl, and hydroxyl groups. Together with the lateral size, the exposed charge might also significantly affect G internalization in cells and tissues, as well as drive the cellular endocytosis pathways. The main internalization routes could be divided in 4 main categories: (i) clathrin-mediated endocytosis, (ii) caveolae-mediated endocytosis, (iii) micropinocytosis and (iv) phagocytosis. Notably, it has to be considered that the extent of G internalization is dependent on the cell type [60]. Macropinocytosis seems to be a general mechanism of internalization, however Linares et al. showed that besides macropinocytosis, pegylated-GO can enter osteoblasts cells through pathways dependent on microtubules, and through clathrin-dependent mechanisms in hepatocytes and macrophages cell lines [60].

In order to coordinate research in different biomedical fields, an in the attempt to obtain results that are comparable between different research groups, the Flagship Work Packages dealing with the investigation of the biological interaction of G with living systems have selected the few-layer GR and monolayer GO nanosheets used throughout this work and object of this thesis. The material was provided and characterized by Dr. Vazquez's group (University of Castella La Mancha, Spain). GR nanosheets were prepared by exfoliation of graphite through interaction with melamine by ball-milling treatment. After exfoliation, melamine could be easily removed by filtration to obtain stable dispersions of few-layer graphene to reach a final concentration 0.09 ppm in $H_2O$ [61]. Monolayer GO is commercially available and provided by the Grupo Antolin Ingenieria by oxidation of carbon fibers [62]. Initial GO suspensions were washed with water to remove the presence of acids and were fully characterized. The elemental analysis gave the following results (as percent weight): 47.71 ± 0.03 wt % C, 3.04 ± 0.02 wt % H, 0.15 ± 0.01 wt % N, and 0.27 ± 0.03 wt % S. Oxygen content was therefore calculated at ca. 48% by weight.

Zeta-potential, a measure of the electrostatic potential at the electrical double layer surrounding a nanoparticle in solution [63], was also measured. Nanoparticles with a zeta potential between -10 and +10 mV are considered approximately neutral, while nanoparticles with zeta potentials greater than +30 mV or less than -30 mV are considered strongly cationic and strongly anionic, respectively. Zeta-potential values for the G nanosheets used in this study were estimated around −35 mV at physiological pH. Dynamic light scattering (DLS) and transmission electron microscopy (TEM) analysis revealed a higher lateral size distribution of GR (500−2000 nm) compared to GO (100−

1500 nm) nanosheets. Moreover, Raman spectroscopy, a vibrational technique that is extremely sensitive to geometric structure and bonding within molecules, was used to provide a further characterization of G materials [64]. Even small differences in geometric structure lead to significant differences in the observed Raman spectrum of a molecule. The spectra of G materials are characterized by two principal bands designated as the G band and 2D bands; a third band, identified as D, band may also be present when there are defects within the carbon lattice (**Figure 5 A**). The G band is a sharp band that appears around 1587 $cm^{-1}$ in the spectrum and its position is highly sensitive to the number of layers; the intensity of the band is also a measurement of layer thickness (**Figure 5 B-C**). The 2D band is used to determine G layer thickness too, based on 2D band shape (**Figure 5 D**). In addition, the intensity ratio of the 2D to G band ($I_{2D}/I_G$) identify high quality (defect free) single layer G (when equal to 2) [64].

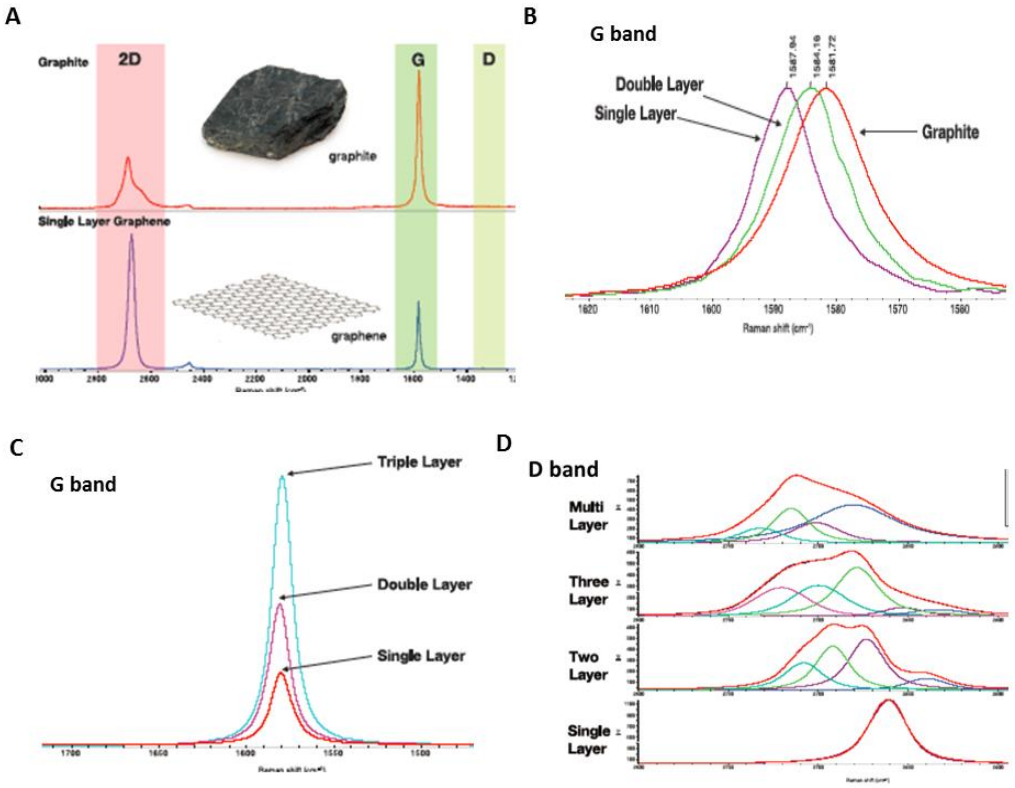

**Figure 5**. **A** The Raman spectra of graphite and graphene. **B**. The G band position is a function of layer thickness. As the number of layers increases, the band shifts to a lower wave number. **C.** There is a linear increase in G band intensity, as the number of G layers increases. **D.** The 2D band exhibits distinct band shapes depending on the number of layers. Modified by Wall [65].

The G nanosheets used through the next studies exhibited G and 2D modes around 1573 and 2700 $cm^{-1}$, respectively, which satisfy the Raman selection rules. When G is affected by defects Raman spectroscopy showed a D peak around 1345 $cm^{-1}$ (**Figure 6 A**). The intensity ratio between the D and the G band was calculated at different locations and used to quantify defects on the G surface, giving a significant low value for GR (0.22 ± 0.05; n = 5) compared to GO (0.81 ± 0.05; n = 5). Finally, thermogravimetric analysis (TGA) was also used to quantify the degree of functionalization of these materials. The low weight loss observed in GR (7%) corroborated the low quantity of oxygen groups generated by the exfoliation process in comparison to the values obtained for GO (46%) (**Figure 6 B**).

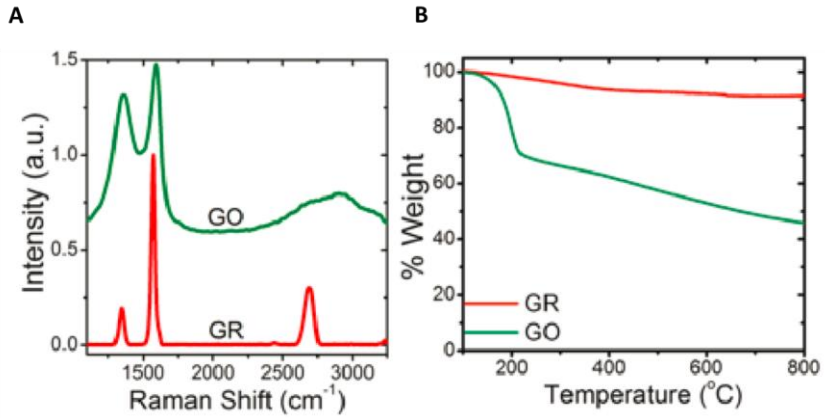


**Figure 6. Characterization of GR and GO nanosheets.** (**A**) Raman spectroscopy; (**B**) thermogravimetric analysis. Modified by Bramini et al. [62].

### *2.3.2 Graphene biocompatibility for applications to the central nervous system.*

Each biomedical application requires specific tests to assess G biocompatibility. For example, when using G-based materials for drug delivery purposes, it is fundamental to test concentration-dependent cytotoxicity, to investigate the mechanisms of cytotoxicity *in vitro* and to probe the biodegradability of the material *in vivo*. On the other hand, when employing G scaffolds for tissue engineering purposes, it is mandatory to monitor their chemical and mechanical stability, biocompatibility and long term toxicity, to avoid the onset of chronic inflammation.

Focusing on CNS, a recent work of Bramini et al. [66] pointed the attention on the effect of chronic and acute exposure of rat primary cortical neurons to GR and GO nanosheets, described in the previous paragraph (**Figure 7**). Chronic GR and GO exposure did not cause alterations in cell viability, excitability, and network formation. However, a more detailed investigation on cell functionality revealed some pathophysiological effects specific to GO exposure, such as the inhibition of excitatory transmission accompanied by a reduction in the number of excitatory synaptic contacts and by a concomitant enhancement of the inhibitory activity; the induction of autophagy; altered $Ca^{2+}$ dynamics, and downregulation of the main players in the regulation of $Ca^{2+}$ homeostasis, in both excitatory and inhibitory neurons (**Figure 8**) [62]. Accordingly, work from a different group confirmed that a concentration of 10 µg/ml of GO nanosheets interfered with synaptic signaling. In particular a reduction in frequency of spontaneous post-synaptic currents (PSC, mPSC), accompanied by a marked reduction in VGLUT1-positive puncta, was noticed. Moreover, a reduction in active neurons,

explored by $Ca^{2+}$ imaging, a decrease in recycled vesicles and alteration of the kinetic of vesicle recycling were also noticed upon GO treatment [66]. All these findings point the attention on the biocompatibility of G nanosheets within the CNS; studies on the effects of G nanosheets exposure with other CNS cell types are still missing and are mandatory for every future application, in order to improve the design and engineering of G based technologies.

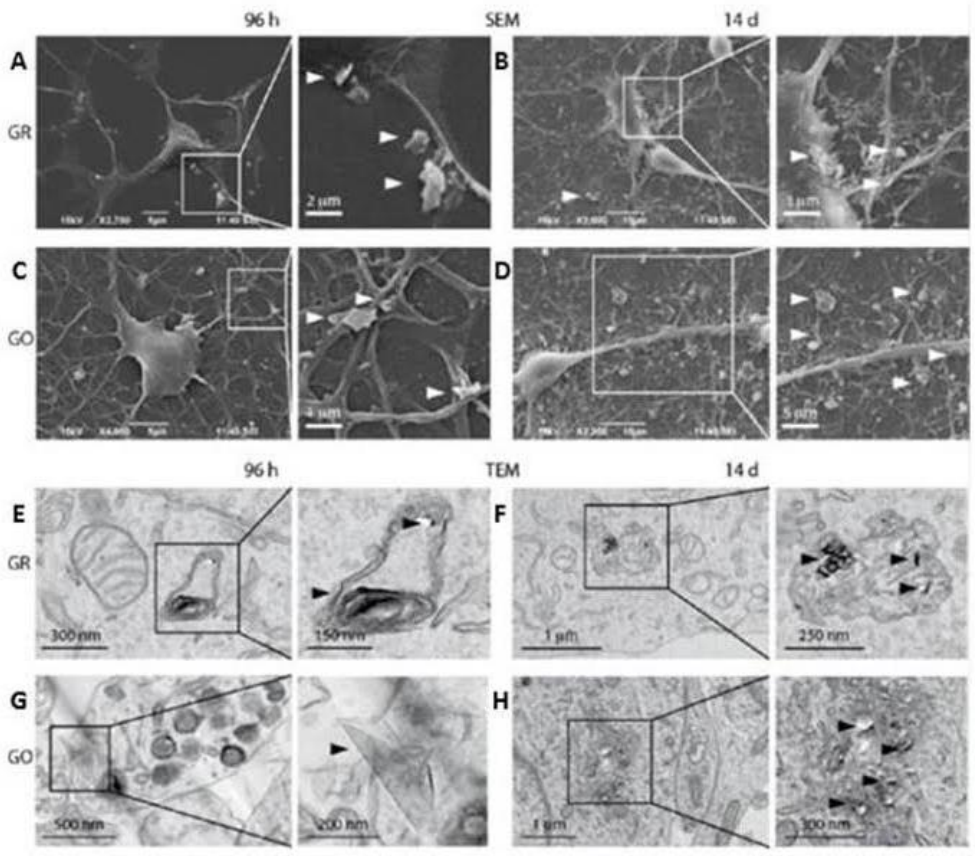


**Figure 7. G-nanosheets interaction with neuronal cells. A-D.** Neurons were exposed to GR and GO flakes 96 h, and 14 days, fixed, and prepared for SEM analysis. A large number of flakes (white arrowheads) were found in contact with the cell membrane; however, cell morphology and network development were substantially unaffected. **E-H.** Intracellular localization of G nanosheets was studied by TEM. Starting from 96 h of incubation G nanosheets were internalized

into intracellular vesicles (E, H black arrowheads) or free in the cytoplasm (H, black arrowheads). Modified from Bramini et al. [62].

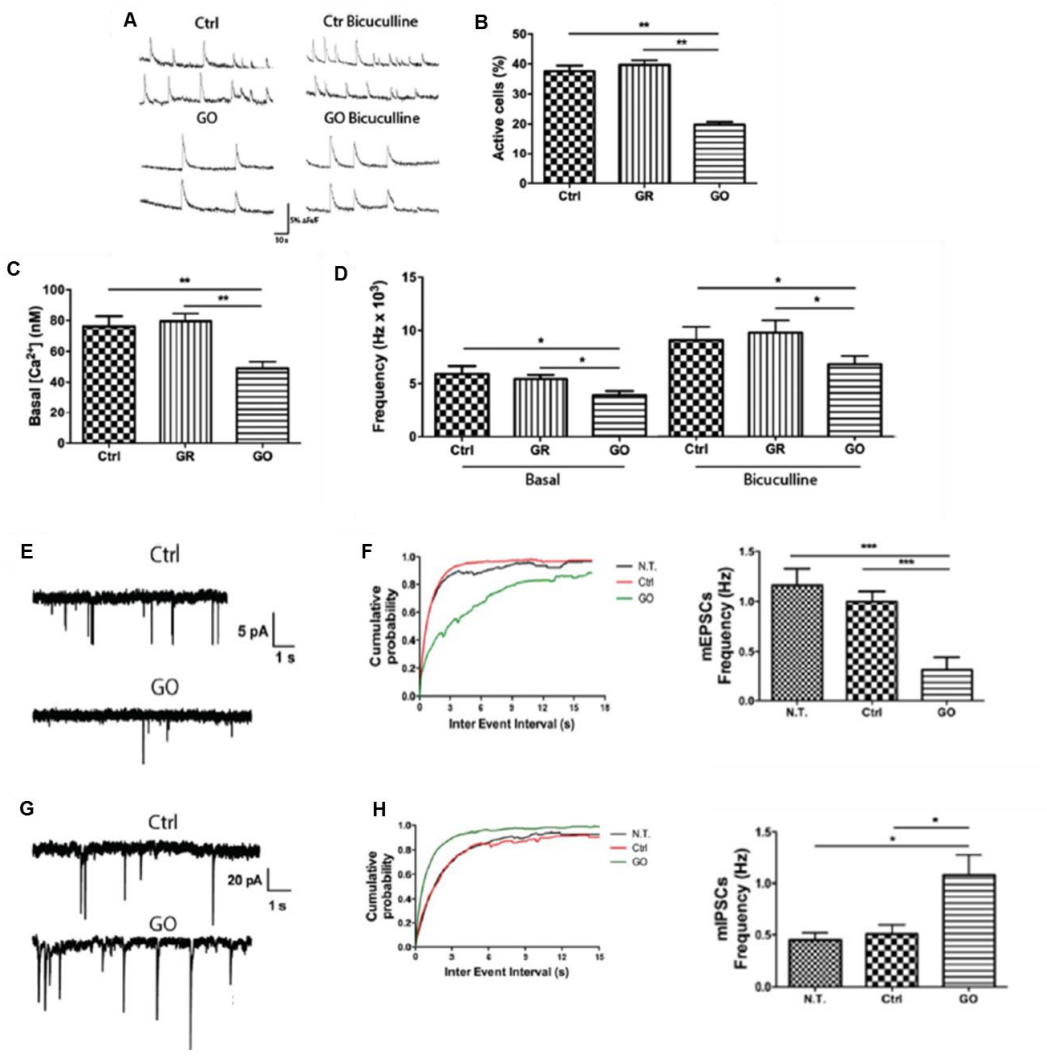


**Figure 8. $Ca^{2+}$ dynamics and spontaneous synaptic transmission in cortical neurons treated with GO for 14 DIV. A.** Representative spontaneous (left panels) or bicuculline-evoked (right panels) $Ca^{2+}$ oscillations recorded in 14 DIV cortical cultures treated with either vehicle (Ctrl) or 10 μg/mL GO for 14 days. (**B**) Percentages of spontaneously active cells (**C**) and mean resting $Ca^{2+}$ concentrations measured at the cell body level (**D**) The frequency of $Ca^{2+}$ oscillations under basal conditions or in the presence of bicuculline (20 μM) displayed lower values for GO-treated neurons. Data are means ± SEM. *p < 0.05, **p < 0.01, two-tailed Student's t-test; n = 30 cells per experimental condition, from 4 independent neuronal preparations. (**E-H**) Activity of excitatory and inhibitory synapses in primary cortical neurons treated with GO for 14 days. (**E**) Representative recordings of miniature excitatory postsynaptic currents (mEPSCs) in cortical

neurons treated with GO (10 μg/mL) or vehicle. (**F**) Cumulative distribution of inter-event intervals and mean (±SEM) frequency of mEPSCs in control and GO-treated neurons. (***$p < 0.001$, one-way ANOVA and Bonferroni's multiple comparison test; n = 15 cells from 2 independent neuronal preparations) (**G**) Representative recordings of miniature inhibitory postsynaptic currents (mIPSCs) in cortical neurons treated with GO (10μg/mL) or vehicle. (**H**) Cumulative distribution of inter-event intervals and mean (± SEM) frequency of mIPSCs in control and GO-treated neurons. Modified from Bramini et al.[62].

For what concerns G scaffolds, *in vitro* studies demonstrated the viability of neuronal cells grown on planar 2D G-substrates, highlighting the ability of G-scaffolds to promote neuronal growth and differentiation, and to stimulate neuronal activity [67]. Moreover, previous works established that G films promote differentiation of hNSCs toward neurons with respect to glia cells, compared to hNSCs grown on standard glass substrates (**Figure 9**) [68]. Accordingly to Wang et al. [69] fluorinated G substrates promote the differentiation of mesenchymal stem cells (MSCs) towards neuronal lineages via spontaneous cell polarization. These phenomena have been imputed to the G aromatic scaffold, which increases the local concentration of extracellular matrix (ECM) such as collagen, laminin and fibronectin by non-covalent binding. Intriguingly, interfacing mouse hippocampal neurons on 2D G-substrates resulted in an increase in neurite number and length compared to cells cultured on polystyrene substrates.

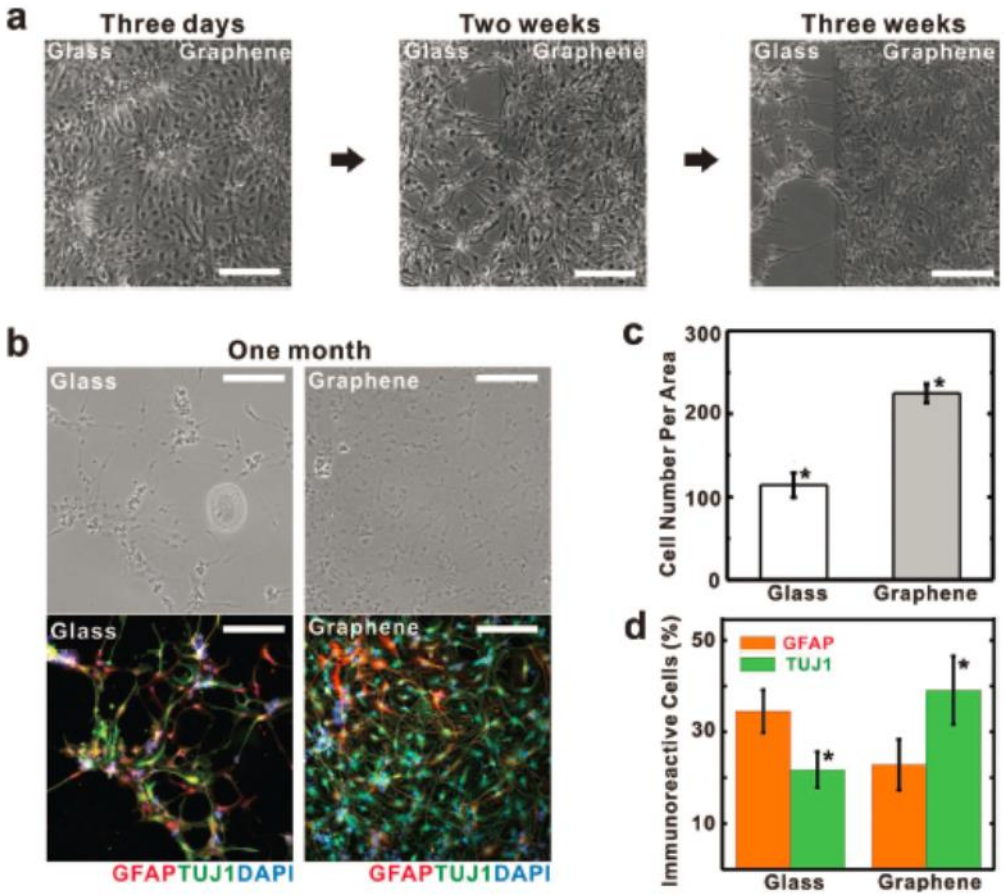


**Figure 9. Neuronal differentiation of hNSC on G films. A.** Bright-field images of the hNSCs differentiated at different time points. Note that the hNSCs on glass were gradually retracted and detached after two weeks, while those on G remained stable even after three weeks of differentiation. **B**. Bright-field (top row) and fluorescence (bottom row) images of hNSCs differentiated on glass (left) and G (right) after one month differentiation. The differentiated hNSCs were immunostained with GFAP (red) for astroglial cells, TUJ1 (green) for neural cells, and DAPI (blue) for nuclei. Note that more hNSCs were adhered to G than to glass. **C**. Cell counting per area on G and glass regions after one-month differentiation. (n = 5, $p < 0.001$). **D**. Percentage of immunoreactive cells for GFAP (red) and TUJ1 (green) on glass and G. ($n = 5$, $p < 0.05$). Modified from Park et al.[68].

However, the unique properties of planar 2D-G scaffolds are exceeded by 3D-G structures, which provide a microenvironment where cells are able to grow under conditions that are closer to the *in vivo* situation. In addition, 3D-G structures possess an enormous interface area and provide highly conductive pathways for charge transport, useful to support neural network formation and neural regeneration. Li et al. firstly described 3D-G foams (3D-GFs) as scaffold for NSCs growth and proliferation. NSCs grown on 3D-GFs were able to differentiate into neurons and astrocytes; moreover, it was also demonstrated that 3D-GFs were optimal platforms for electrical stimulation of NSCs in order to enhance their differentiation (**Figure 10**) [70]. Ulloa et al. [71] showed that hippocampal neurons cultured on 3D-GFs possess a more extensive connectivity associated with an higher synchronization of network with respect to 2D-G substrate systems, mimicking the physiological properties of the brain.

New generation of 3D-G scaffolds combine the advantages of hydrogels, able to mimic soft tissue, with the properties of G. Hybrid G-based hydrogels, synthesized mainly using GO, G oxide peroxide (GOP), or even rGO, are able to support neuronal growth and the development of synaptic activity [72]. These results underline the innovation of G scaffolds to engineer the neural interface devices of the future, introducing the importance of dimensionality, as well as electrical conductivity, in neuronal network dynamics and development.

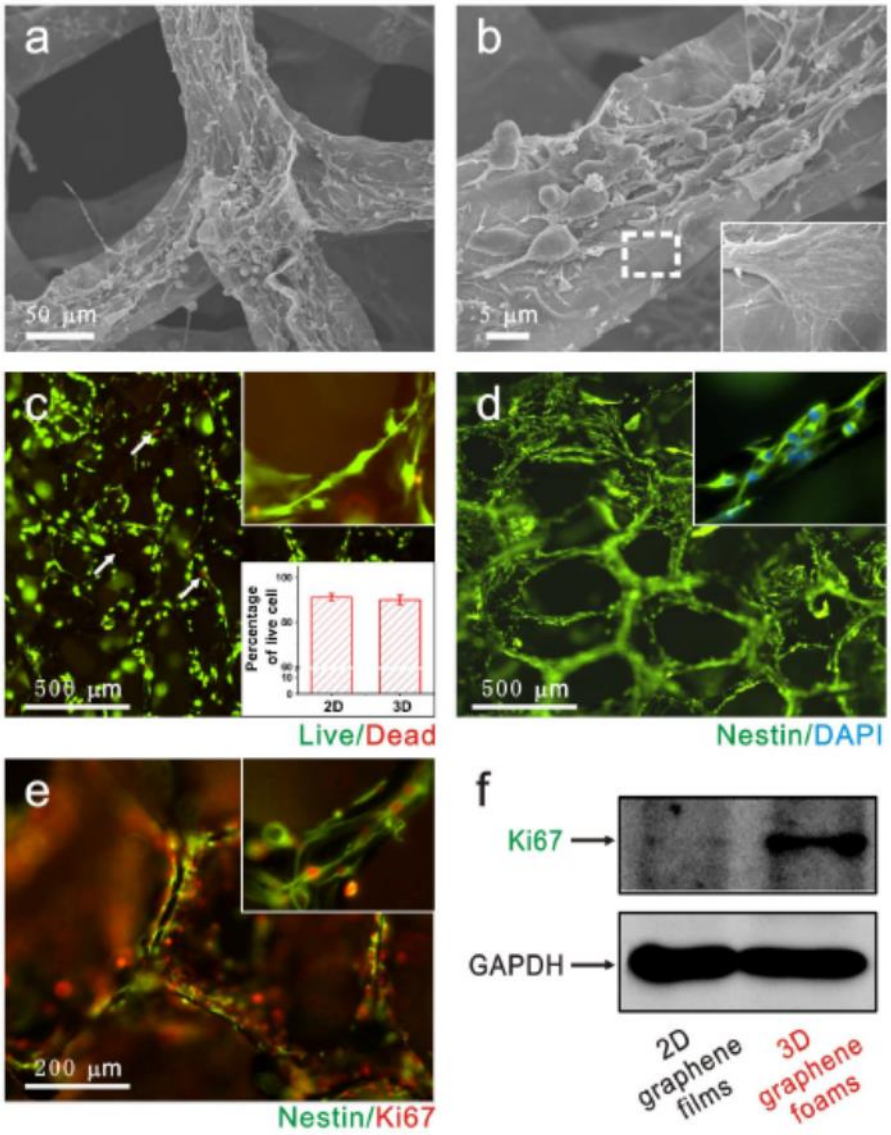


**Figure 10. NSC adhesion and proliferation on 3D-GF**. **A, B.** Low and high-magnified SEM images of NSCs. **C**. Cell viability assay of NSCs cultures on 3D-GFs. **D.** Immunostaining for Nestin (marker of NSCs, green) and DAPI (marker of nuclei, blue). **E-F** Immunostaining (E) and western blot analysis (F) of Nestin and Ki67 (marker of proliferation). Modified from Li et al. [70].

## 2.4. Astrocytes in physiology and pathology.

Astrocytes are part of multicomponent synapses formed by the presynaptic terminal, the postsynaptic neuron, the peri-synaptic processes of astrocytes, the processes of neighboring microglial cells that periodically contact the synaptic structure, and the extracellular matrix (ECM), which is present in the synaptic cleft and also extends extrasynaptically. *In vivo,* astrocytes can be categorized in different subtypes by cell morphology and anatomical locations. Protoplasmic astrocytes are found predominantly in gray matter, characterized by numerous fine branches, whereas fibrous astrocytes are found throughout all white matter, characterized by less fiber-like processes than the protoplasmic ones [73]. Moreover, the cerebellum contains specialized astrocytes called Bergmann glia; they are characterized by small cell bodies with few processes that form close contacts with synapses. It should be taken into account that astrocytes *in vitro* lose part of the complexity observed *in vivo*, exhibiting a flat, epithelioid morphology due to the nature of the standard, two-dimensional culturing system [74].

Nowadays astrocytes are no longer seen only as support cells; indeed, they play essential functions in CNS homeostasis. Since the discovery of voltage dependent ionic channels in their cell membrane, astrocytes gained an overall different biological significance in the regulation of brain physiology [75]. In fact, besides defining the brain micro-architecture, astrocytes control extracellular homeostasis regulating concentrations of ions, pH and transmitters in the extracellular milieu (**Figure 11**). Notably, they are involved in a process termed “potassium spatial buffering” thanks to inwardly rectifying potassium channel (Kir) [76]. Astrocytes also regulate neuronal activity by removing excess of glutamate via the glutamate transporters GLAST and GLT1, thus avoiding

network hyperexcitation [77]. The role of Kir channels and glutamate clearance in the physiology and pathology of astrocytes will be described in detail in the next paragraph.

In addition, astrocytes are the central elements of neurovascular units and control the local blood flow by releasing prostaglandins, nitric oxide, and arachidonic acid, that can increase or decrease CNS blood vessel diameter and blood flow [78].

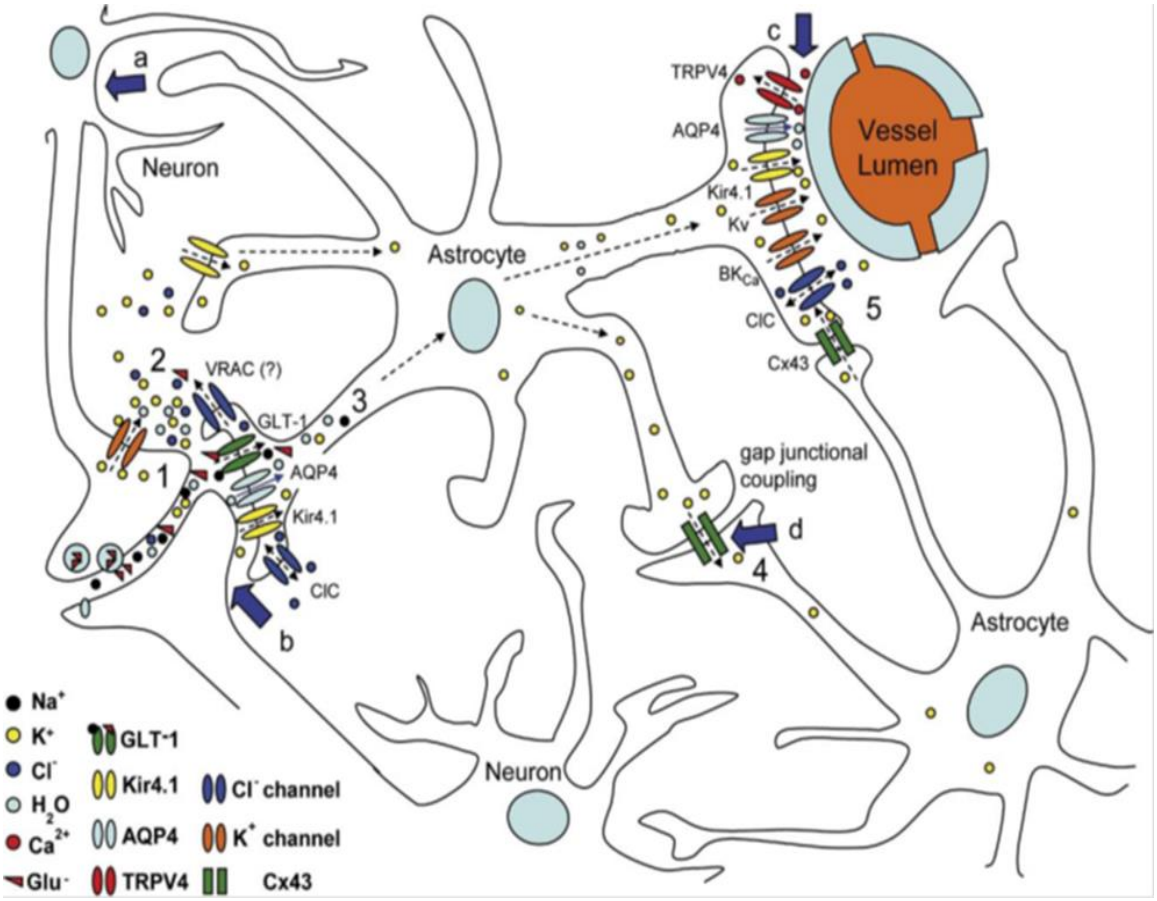


**Figure 11. Astroglial channels involved in extracellular homeostasis.** Modified from Ferroni et al. [79].

Astrocytes are also characterized by a complex modulation of $Ca^{2+}$ events that coordinate their major functions, and in turn influence neuronal activity. The dynamics of

intracellular astrocytic calcium $[Ca^{2+}]_i$ fluctuations have been intensely investigated in recent years. Increase of $[Ca^{2+}]_i$ can be triggered by transmitters released during neuronal activity, such as γ-aminobutyric acid (GABA) [80], glutamate [81], and ATP [82], which bind to G-protein-coupled receptors (GPCRs) that activate the pathway of inositol-3-phosphate ($IP_3$). Once at the ER, $IP_3$ binds to a ER-resident ligand-gated $Ca^{2+}$ channel, inducing the opening of the channel and the consequent diffusion into the cytoplasm of $Ca^{2+}$ stored in the ER, thus effectively rising $[Ca^{2+}]_i$ [83]. Increases of $[Ca^{2+}]_i$ in turn induce release of chemical transmitters, so called "gliotransmitters", from astrocytes. Gliotransmitters include ATP, glutamate, D-serine and GABA, which can modulate neuronal activity post-synaptically [84] and transmitter release probability at presynaptic sites [85, 86]. In addition, $[Ca^{2+}]_i$ rise spreads along astrocyte processes and even between adjacent glial cells through the gap junctions, permitting long-distance propagation of the $Ca^{2+}$ waves [84]. At vascular endfeets, $Ca^{2+}$ waves induce the release of vasoactive messengers such as arachidonic acid, prostaglandins, 20-hydroxyeicosatetraenoic acid, epoxyeicosatrienoic acids, phospholipase C and adenosine [78]. Various studies have reported that dysregulation or malfunctioning of $Ca^{2+}$ signaling in astrocytes could play a major role in different neurological disorders, like epilepsy [87], Alzheimer's disease [88] and Huntington's disease [89]. In fact, excess of $Ca^{2+}$ released from the ER stores induces an exaggerated gliotransmission, which can have important effects on neuronal activity and blood flow regulation [78].

Of note, astrocytes secrete factors involved in synaptogenesis, regulating fundamental processes such as the number of synapses [90, 91], postsynaptic activity by up-regulation of AMPA receptor expression [92], and presynaptic release by increasing

release probability [93]. Astrocytes are also involved in synapse elimination through two different mechanisms, i.e. the release of TGF-β, which in turn induces the expression of C1q on synapses to be pruned, activating complement-dependent phagocytosis by microglia [94-96], and the direct phagocytosis of silent synapses by recognizing specific signals on their surface [97].

Furthermore, astrocytes are able to respond to CNS insults such as infections, traumas, ischemia, and neurodegenerative diseases, by a process commonly referred as "reactive astrogliosis". This is characterized by an increase in astrocyte number, up-regulation of glial fibrillary acidic protein (GFAP), migration to the injury sites, formation of glial scar and modulation of the inflammatory response [98]. Reactive astrocytes belong to two different categories, termed A1 and A2 astrocytes, and are characterized by a specific proteomic profile [99]. In an elegant study by Lidellow et al. [100], it has been demonstrated that A1 astrocytes, activated by release of cytokines from microglia cells, are involved in neurodegeneration, including neural cell death and impairment in synapses formation. Indeed, A1 reactive astrocytes have been found in brain regions involved in neurodegeneration in a variety of human pathologies, including Alzheimer's disease, multiple sclerosis, Parkinson's disease, and Huntington's disease. By contrary, A2 astrocytes have neuroprotective functions trough release of neuroprotective factors, phagocytosis of synapses and clearance of debris and dead cells [100].

Investigations on the role of astrocytes in CNS are still open to clearly elucidate the link between microglia, astrocytes, neurons and the BBB under physiological and pathological conditions. In this scenario, development of new strategies to treat CNS

pathologies cannot overlook the potential of astrocytes as targets to promote repair in disease, as well as the pathological effects induced by astrocyte dysregulation.

### *2.4.2 Potassium and glutamate homeostasis of astrocytes under physiological and pathological conditions.*

Several pieces of evidence have identified ion channels and transporters as key players in the physiology of astrocytes. Therefore, any physiological and pathological conditions that alter the expression and/or the functionality of these plasma-membrane proteins will invariably affect the neuronal network [79]. Numerous studies have identified diverse ion channels and transporters whose expression and activity can be modified according to the functional states of the astrocytes. *In vivo* fully differentiated astrocytes express a large $K^+$ conductance, which is associated to the expression of inward rectifying $K^+$ channels [76]. There are 7 different Kir subtypes, classified according to their different electrophysiological and molecular properties; however astrocytes predominantly express the weakly rectifying Kir 4.1 channels, encoded by the *KCNJ10* gene [101]. Low expression of heteromeric channels formed by Kir 2.1 and Kir 5.1 subunits has also been reported [102]. In astrocytes, Kir 4.1 expression is heterogeneous throughout the brain and spinal cord [103-105] and increases during development [106, 107]. The role of Kir-mediated current in buffering extracellular $K^+$ has been widely reported; under physiological conditions, during normal neuronal activity, astrocytes remove excess $K^+$ from the extracellular space through Kir 4.1 channels, redistributing it at distant sites where extracellular $K^+$ is low [108]. Genetic ablation of Kir4.1 in astrocytes impairs the homoeostasis of extracellular $K^+$ [109, 110]. Since Kir4.1 displays weakly rectifying

properties and lack of intrinsic voltage dependence, it allows both the influx end efflux of $K^+$ according to the electrochemical gradient, thus contributing to set the very negative resting membrane potentials of astroglial cells *in situ* [110]. Of note, this negative resting membrane potential is critical also for the regulation of the $Na^+$-dependent uptake of glutamate, which is favoured by negative membrane potentials [109].

Decreased Kir current in astrocytes is a hallmark of epileptic tissue [111, 112], and downregulation of Kir channels was also reported in reactive astrocytes few days following global cerebral ischemia [113]. Moreover, $K^+$ conductance was found to be depressed few days after traumatic brain injury, a condition that causes $K^+$ accumulation in the extracellular space and an alteration of neuronal activity [114]. Additionally, reduced Kir 4.1 expression was displayed by mouse models of neurodegenerative diseases characterized by an impairment of $K^+$ homeostasis such as amyotrophic lateral sclerosis (ALS) and Huntington's disease (HD) [115-117].

Astrocytes are also responsible for regulating neuronal activity by removing excess of glutamate via the glutamate transporters. Five transporters for glutamate have been cloned, named Excitatory Amino Acid Transporter (EAAT)1-5 [118, 119]. Among these, EAAT1 (GLAST) and EAAT2 (GLT-1) are the most expressed at astrocytic plasma membrane. GLT1 and GLAST have different localization in the brain [120] and are developmental regulated [121]. While GLAST is present in rat forebrain and cerebellum at birth, GLT-1 is expressed at postnatal week 3 and reaches the adult pattern by week 5. In the adult brain, GLT-1 expression is most abundant in forebrain regions [122], with the highest astrocyte GLT-1 levels in caudate nucleus, cortex, and

hippocampus. A recent work demonstrated that neuronal factors determine the specific expression of GLT-1 and GLAST in different brain areas

At the synaptic cleft glutamate concentration can increase transiently from <20 nM to 1 mM following action potentials [123],while cytosolic glutamate ranges from 1 to 10 mM in different cell types [124]. As glutamate is not metabolized upon release, under physiological conditions astrocytes maintain extracellular glutamate concentration below toxic level to prevent neuronal hyperexcitability or receptors desensitization [77]. They regulate glutamate clearance both by the changing the expression of glutamate transporters, and by modifying the transporter activity. It is known that treatment with dibutyryl-cAMP or other growth factors, associated with morphological and biochemical astrocyte maturation, induces expression of GLT-1 and increases expression of GLAST in astrocyte cultures. Altered expression of GLT-1 and GLAST is linked to neurodegenerative diseases, including traumatic brain injury, hypoxic/ischemic insults [125], epilepsy [126, 127], glioma [128] and amyotrophic lateral sclerosis [129]. The levels of GLT-1 and/or GLAST proteins are also lower in brain tissue from patients with amyotrophic lateral sclerosis [130], epilepsy [131], Alzheimer's disease [132] and Huntington's disease [133].

Glutamate clearance is also regulated by changes in transporters activity; in fact, GLT-1 and GLAST are antiporters that carry one molecule of glutamate inside the cells along with three $Na^+$ and one $H^+$, while exporting one $K^+$. These transporters are electrogenic, taking up glutamate much more effectively at negative resting potentials. Considering that Kir 4.1 channels are responsible for maintaining a negative resting potential in astrocytes cells, Kir 4.1 channels ensure maximal glutamate transport rates

via GLT-1 or GLAST. As matter of fact, knock-down of Kir 4.1 by RNA interference, as well as inhibition of Kir channels with 100 μM $Ba^{2+}$, inhibits glutamate clearance, highlighting the role of membrane hyperpolarization in glutamate clearance [134]. Moreover, it has also been demonstrated that knockout of Kir4.1 *in vivo* reduced glutamate uptake [109] leading to seizure susceptibility in mouse [112].

### *2.4.3 Interaction between astrocytes and graphene materials.*

In view of its many potential biomedical applications, it is critical to understand the effects that G have on astrocytes due to their key role in regulating brain homeostasis. So far very limited data are available on this topic. Rauti et al. [66] demonstrated that GO nanosheets do not alter astrocyte viability *in vitro*, but affect the ability of astrocytes to release synaptic-like microvesicles that are involved in neuron-astrocyte communication. Mendonca et al. [25], instead, focused their studies on the effects of rGO nanosheets *in vivo*. After systemic administration of rGO, no changes in astrocyte viability and glia reactivity were found in the hippocampus of rats. By contrast, they demonstrated that PEGylation of rGO induced cytotoxicity of astrocytes *in vitro* affecting cell viability, morphology and ROS production at the very high concentration of 100 μg/ml for 24 h (**Figure 12**). *In vivo* studies demonstrated that the intravenous injection of pegylated rGO (rGO-PEG) leads to a reduction in GFAP expression in rats hippocampus after 3 h and 7 days post injection and to the concomitant increase in antioxidant enzymes involved in detoxification of excess ROS. These data demonstrated the dose- and time-dependent toxicity of rGO-PEG for astrocytes, speculating oxidative stress-mediated damage as a possible mechanism of toxicity [26]. These few studies highlight the

importance of a specific toxicity profile for each G-materials also when working with astrocytes.

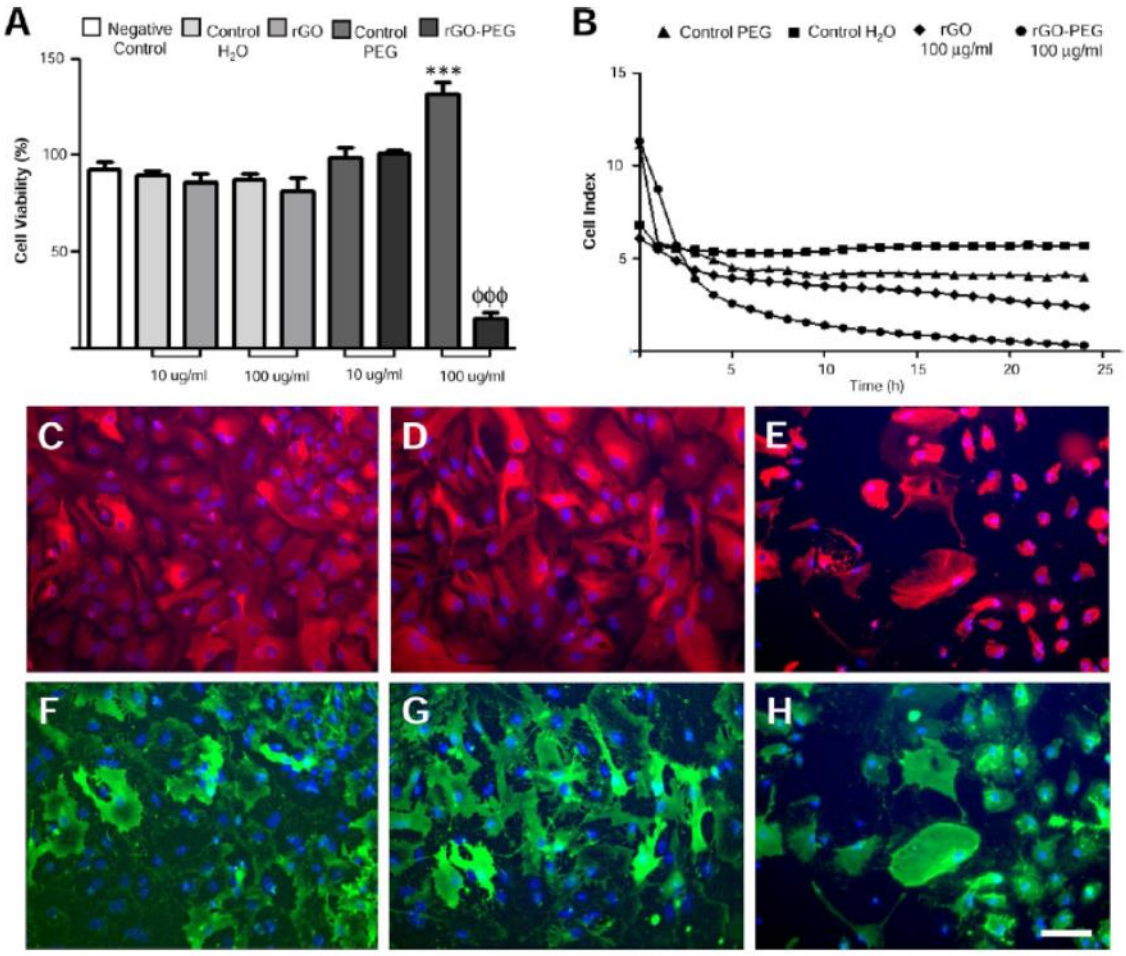


**Figure 12. Effects of rGO and PEG rGO on astrocyte cultures. A**. Astrocyte viability after 24 h incubation with 10 and 100 µg/ml of rGO and rGO-PEG. The percentage is given in relation to control medium and the columns are mean ± SEM (n=4). **B.** Analysis of cell viability using xCELLigence system. The curves represent the average of four individual well ± SEM of a representative experiment. **C-H** Representative images of GFAP (red) and aquaporin 4 (green) after incubation with vehicle (**C,F**), rGO 100 µg/ml and (**D**,**G)** rGO-PEG 100 µg/ml incubation (**E**,**H**). Modified from Mendonca et al. [26].

As far as G scaffolds are concerned, *in vitro* studies demonstrated that 2D and 3D G-scaffolds enhance glial differentiations from adipose stem cells [135] and neural stem

cells [70], supporting the biocompatibility of G substrates and their ability to promote cellular differentiation. *In vivo* studies reported that G scaffolds implanted in different brain regions reduce glial activation and the formation of the glia scar, compared to scaffolds not G-functionalized [136]. However, most of these *in vitro* and *in vivo* studies present limitations, of which the main is that astrocyte viability and reactivity is evaluated only based on the quantification of glial fibrillary acidic protein (GFAP). Little or nothing has been reported on the functionality, proteomic, lipidomic and gene expression profile of astrocytes exposed to GRMs, neither the mechanisms of G toxicity have been elucidated. Further studies are then needed to clarify these points and represent the aim of this thesis.

## 2.5 Impact of graphene nanosheets on primary astrocytes

On the basis of these considerations, previous work of our group aimed at testing the biocompatibility of GR and GO nanosheets with primary astrocytes cell. GR nanosheets were prepared by exfoliation of graphite through interaction with melamine by ball-milling treatment [137]; GR/$H_2O$ dispersions were obtained at a final concentration of 0.09 mg/ml in Milli-Q water, with a lateral size distribution of 500−2000 nm. Melamine traces were estimate to be 0,09 ppm. Monolayer GO was provided by the Grupo Antolin Ingeniería (Burgos, Spain) by oxidation of carbon fibers; GO/$H_2O$ dispersions were obtained at a final concentration of 0.5 mg/ml in Milli-Q water, with a lateral size distribution of 100-1500 nm (**Figure 13**). G nanosheets characterization has been described in detail in paragraph 2.3.1.

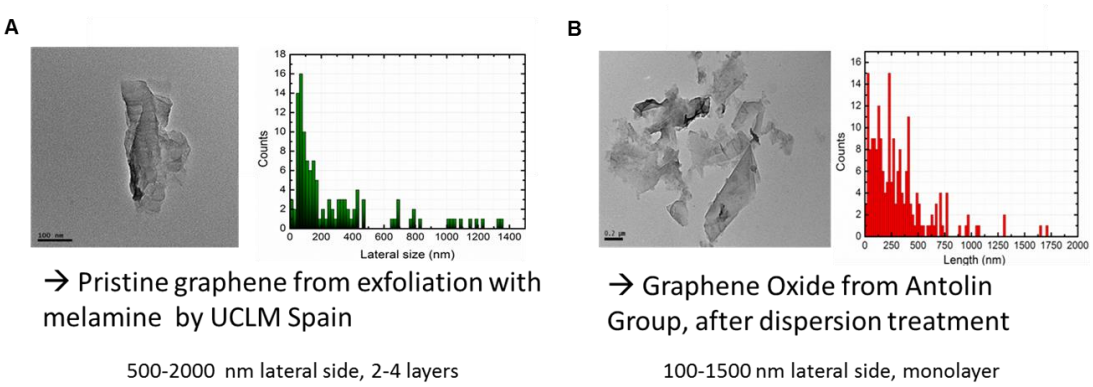


**Figure 13. A**, **B** Representative images of GR (**A**) and GO (**B**) nanosheets by transmission electron microscopy. Lateral dimension distribution of GR (A; 500-2000 nm) and GO (B; 100-1500 nm) nanosheets by dynamic light scattering analysis. Modified from Bramini et al. [62]

Astrocyte physiological response to prolonged exposure to G nanosheets was characterized. Primary astrocytes were isolated from neonatal rat brain cortices were exposed to either GR or GO nanosheets for 1-3 days to assess the effects of short- and long-term G exposure (**Figure 14**). Exposure to G-materials was not harmful to primary astrocytes at any of the concentrations and exposure times tested (**Figure 14a-d**). No appreciable effects on cell viability were also observed when confluent mature astrocytes were treated for 48 h with either GR and GO nanosheets, similarly to what observed upon early exposure (**Figure 14 d**). In summary, these results clearly indicate that exposure to G nanosheets did not affect astrocyte survival and therefore did not induce astrogliopathy caused by a loss of astrocyte viability [138].

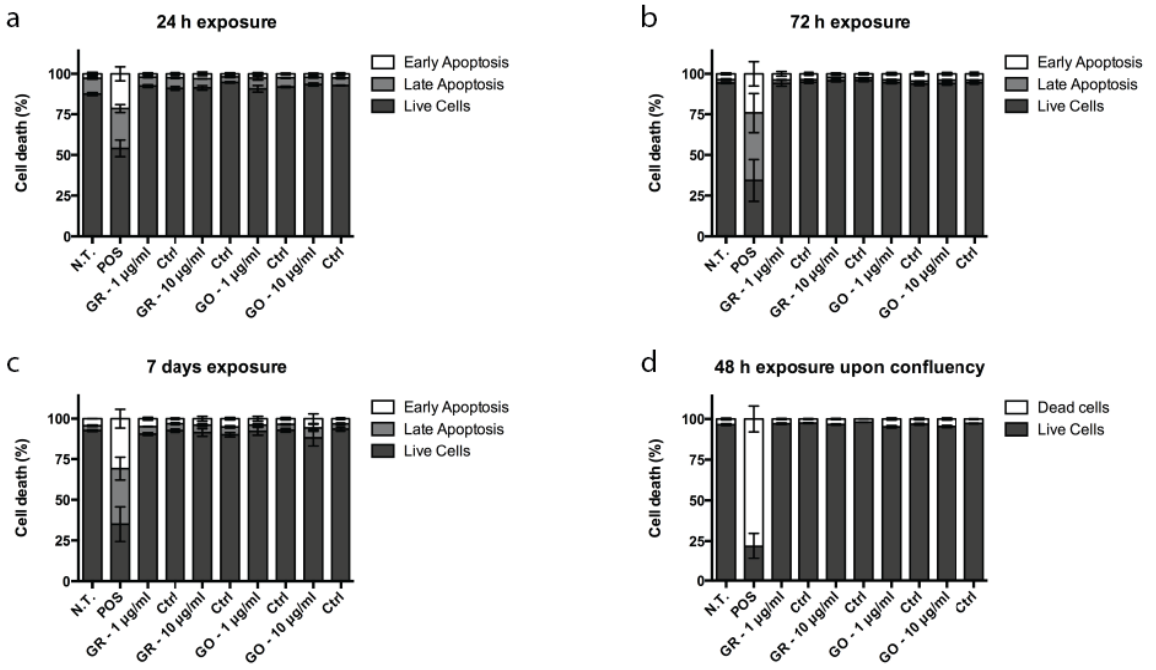


**Figure 14. Viability of primary astrocytes exposed to GR and GO nanosheets.**

(**a**-**c**). Primary rat astrocytes were exposed to GR and GO nanosheets (1 and 10 μg/ml) for 24 h (**a**), 72 h (**b**) and 7 days (**c**), or to the equivalent volume of the respective vehicles (Ctrl: 0.09 ppm melamine / $H_2O$ for GR flakes, $H_2O$ for GO flakes). Staurosporine (POS; 1 μM) was used as a positive control for apoptosis. Cell death was evaluated by flow cytometry analysis of Annexin-V (AxV, for early apoptotic events) and Propidium Iodide (PI, for late apoptosis) staining. The percentages of AxV- and PI-positive cells with respect to the total number of cells were calculated for each experimental group. (**d**) The same experimental procedure was carried out for primary glial cultures at confluence, exposed for 48 h to either GR or GO nanosheets. No significant changes in cell death were observed under all the experimental conditions (45,000 cells from n = 3 replicates per experimental condition, from 3 independent preparations) (Bramini et al, unpublished data).

To get a comprehensive understanding of the intracellular pathways that are affected by G materials, proteomic analysis was carried out on independent preparations of primary astrocytes treated with either GR or GO nanosheets for 72 h, in collaboration with the IIT D3 Pharmachemistry department (Drs. Armirotti and Bandiera). Untargeted LC-MS/MS based proteomics was performed by labellng proteins from astrocytes exposed to GO, GR and their corresponding control samples with TMT isobaric tags [139]. Roughly 1500 proteins were unambiguously identified in the 3 biological replicates and more than 45% of them gave useful over/under expression data. A final list of 594 and 755 proteins were used for protein expression analysis for GR and GO treatment respectively. From this data set, more than 87% of the proteins showed a marked (>20% in the module) upregulation following GR/GO treatment and were subjected to PANTHER gene ontology analysis [140]. The pathways identified were then clusterized according to their corresponding biological process. **Figure 15a** reports the top 10 biological processes enriched in comparison with their corresponding controls for GR and GO respectively. The corresponding percent distribution, calculated on the basis of the total biological pathways mapped by PANTHER, is also reported. Intriguingly, the exposure of the same biological system to two different GRMs triggers the upregulation of different biological processes: mostly metabolism-related pathways for GR (32% of the total) and mostly trafficking-related pathways for GO (55% of the total). A close investigation of the proteins related to calcium metabolism, previously reported to be altered in neurons exposed to G materials [62] was also performed by using STRING[141]. As reported in **Figure 15b**, calmodulin (Calm1) shows opposite expression trends in GR (+21%) and GO (-31%). Some of its closest functional

interactors, such as calmodulin-binding proteins calponin 1 (Cnn1) and caldesmon 1 (Cald1), are among the major upregulated proteins following GR treatment. Several other calcium-related proteins such as calcium-transporting ATPase1 (Atp2b1), calcium-dependent-calmodulin stimulated phosphatase (Ppp3r2), $Ca^{2+}$-binding proteins (calreticulin (Calr) and calumenin (Calu)), calcium and integrin binding family member 2 (Cib2), calpain 2 (Capn2), and calnexin (Canx) are upregulated following exposure to GO. These preliminary results set the basis for further functional investigations, object of this thesis.

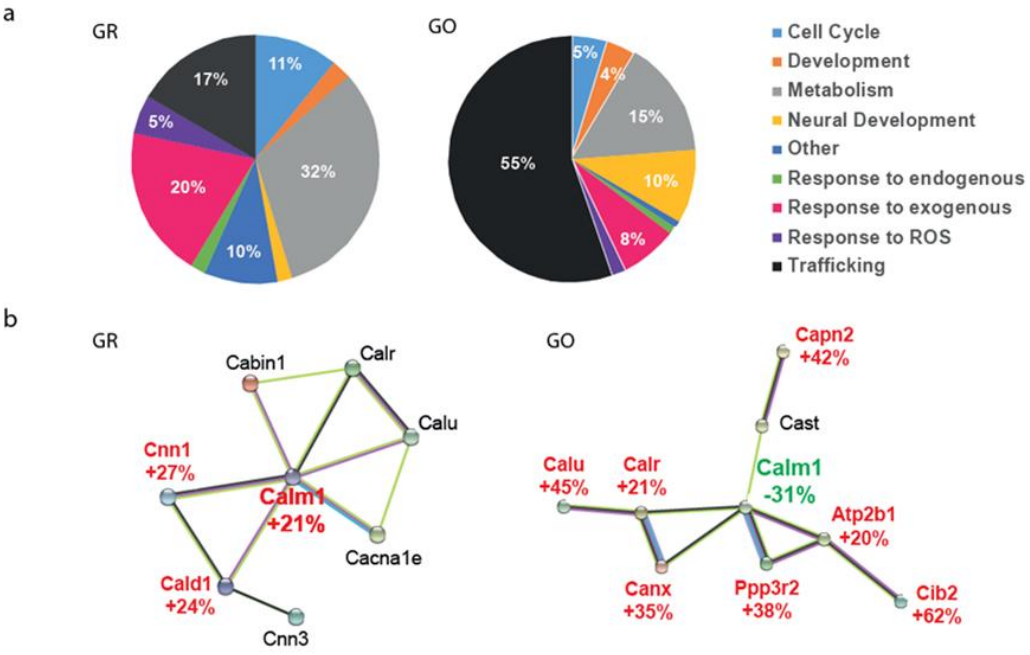


**Figure 15. Proteomic and lipidomic profiles of primary astrocytes exposed to GR and GO nanosheets.**

(**a**) Most upregulated biological processes following exposure of astrocytes to GR and GO. The percent value for each process is calculated on the basis of the total number of altered pathways detected by PANTHER. (**b**) Expression dynamics of Calmodulin protein interaction network following exposure to different GRMs, as reported by STRING. (Bramini et al, unpublished data).

# 3. AIM OF THE THESIS

G-related materials are the focus of intense research efforts to devise novel nanomaterial-based theranostic strategies for targeting the CNS. Previous work published by our group pointed the attention on effects of GO nanosheets on neuronal network transmission and functionality, warning on the safety of G materials once in contact with neuronal cells. However, brain parenchyma is composed also of other cells besides neurons, namely glial cells, which are involved in fundamental activities related to maintaining the functional and structural homeostasis of the CNS. Thus, to support the view that G could be a suitable material for neurobiology application *in vivo*, its biocompatibility with glial cells must also be tested. Thus, we extended the study of the bio-interactions of GR and GO nanosheets in CNS by addressing the effects of nanosheet exposure on primary astrocytes.

Considering the different properties of the two G materials analyzed (i.e lateral size, layer number, surface charge), we expect to detect a different biological response. A complete analysis was conducted for each material by exploring (i) the molecular mechanisms of G nanosheets internalization, (ii) the effects of G exposure on cell morphology and physiology and (iii) the physiological changes induced by nanosheet-exposed astrocytes to co-cultured primary neurons. The investigation of astrocyte response to G and GRMs will be helpful to find novel nanotechnology-based therapeutic strategies for a variety of CNS conditions, and it is at the same time necessary to understand whether exposure to GRMs can lead to the onset of pathologies of astrocytes *per se* or due to alterations in glia-neuron interaction.

# 4.MATERIALS AND METHODS

***Preparation of primary astrocytes and astrocyte/neuron co-coltures***.

All experiments were carried out in accordance with the guidelines established by the European Community Council (Directive 2010/63/EU of 22 September 2010) and were approved by the Italian Ministry of Health (Authorization #306/2016-PR on March 24, 2016). Primary cultures were prepared from wild-type Sprague-Dawley rats (Charles River, Calco, Italy). All efforts were made to minimize suffering and to reduce the number of animals used. Rats were sacrificed by $CO_2$ inhalation, and 18-day embryos (E18) were removed immediately by caesarean section. Briefly, enzymatically dissociated astrocytes were plated on poly-D-lysine-coated (0.01 mg/ml) cell culture flasks and maintained in a humidified incubator with 5% $CO_2$ for 2 weeks. At confluence astrocytes were enzymatically detached using trypsin–EDTA and plated on glass coverslips (Thermo-Fisher Scientific, Waltham, MA) at a density of 20,000-40,000 cells/ml, depending on the experiment. Cultures were incubated at 37 °C, 5% $CO_2$, 90% humidity in medium consisting of DMEM (Gibco/Thermo-Fisher Scientific) supplemented to reach final a concentration of 5% glutamine, 5% penicillin/streptomycin and 10% Foetal Bovine Serum (FBS; Gibco/Thermo-Fisher Scientific). For experiments involving G treatments, cultures were incubated at 1 day *in vitro* (DIV) in a medium containing either 1 or 10 µg/ml of either GR or GO nanosheets. Control samples were subjected to the same medium change with the addition of equivalent volumes of the respective vehicle (0.09 ppm melamine/$H_2O$ for GR flakes, $H_2O$ for GO flakes). Cultures were used at DIV 2, 4 and 8 (i.e., after 24 h, 72 h and 7 days of GR/GO incubation, respectively). For experiments involving astrocyte/neuron co-cultures, astrocytes were

seeded on poly-D-lysine-coated (0.01 mg/ml) glass coverslips at a density of 40,000 cells/ml. After 72 h of incubation with GR/GO or the respective vehicle (see above), enzymatically dissociated cortical neurons obtained from 18-day rat embryos (E18) were plated on the top of astrocytes at a density of 40,000 cells/ml in Neurobasal (Gibco/Thermo-Fisher Scientific) supplemented to reach a final concentration of 5% glutamine, 1% penicillin/streptomycin, and 2% B27 (Gibco/Thermo-Fisher Scientific). All chemicals were purchased from Life Technologies/Thermo-Fisher Scientific unless stated otherwise. All experiments on co-cultures were performed at 10 DIV.

***Immunofluorescence staining and confocal imaging***.

Primary astrocytes were fixed in phosphate-buffered saline (PBS)/4% paraformaldehyde (PFA) for 20 min at RT. Cells were permeabilized with 1% Triton X-100 for 5 min, blocked with 2% FBS in PBS/Tween 80 0.05% for 30 min at RT and incubated with primary antibodies in the same buffer for 45 min. The primary antibodies used were: rabbit polyclonal anti-Iba1 (#01919741, Wako, Japan), mouse monoclonal anti-glial fibrillary acidic protein (GFAP, #G3893, Sigma-Aldrich, Milan, Italy), guinea pig polyclonal anti-vesicular glutamate transporter-1 (VGLUT1, #AB5905, Millipore, Milan, Italy), rabbit polyclonal anti-vesicular GABA transporter (VGAT, #131003, Synaptic System, Gottingen, Germany), rabbit polyclonal anti-microtubule-associated protein 1A/1B-light chain 3 (LC3, #2775, Cell Signaling Technology, Danvers, Massachusetts, USA), rabbit polyclonal anti-astrocyte potassium channel KIR4.1 (KIR4.1, #APC-035, Alomone, Jerusalem, Israel) and rabbit polyclonal anti-glutamate transporter 1 (EAAT2, #3838, Cell Signaling Technology). After the incubation with primary antibodies and

several PBS washes, neurons were incubated for 45 min with the secondary antibodies in blocking buffer solution. Fluorescently conjugated secondary antibodies were from Molecular Probes (Thermo-Fisher Scientific; Alexa Fluor 488 #A11029, Alexa Fluor 568 #A11036, Alexa Fluor 647 #A21450). Samples were mounted in ProLong Gold antifade reagent with DAPI (#P36935, Thermo-Fisher Scientific) on 1.5 mm-thick coverslips. For EEA1, LAMP1, VGLUT1/VGAT-positive terminals and LC3 vesicles, image acquisition was performed using a confocal laser scanning microscope (SP8, Leica Microsystems GmbH, Wetzlar, Germany) at 63x (1.4 NA) magnification. Z-stacks were acquired every 300 nm; 10 fields/sample (n=2 coverslips/sample, from 3 independent culture preparations). Offline analysis was performed using the ImageJ software and the JACoP plugin for co-localization studies. For each set of experiments, all images were acquired using identical exposure settings. For VGLUT and VGAT quantification experiments, values were normalized to the relative cell volume calculated on the basis of β-tubulin III labeling. For cholesterol investigation, filipin (F-9765, Sigma-Aldrich) staining was carried out. Briefly, cells were fixed as described above and incubated with 1.5 mg/ml of glycine in PBS for 10 min at RT to quench the PFA. Cells were incubated for 2 h at RT with 0.05 mg/ml of filipin in 10% FBS-PBS solution. Images were acquired at a confocal microscope at 63x (1.4 NA) magnification, using 405 nm excitation wavelength and filter-set 430 nm long pass filter. For sodium azide ($NaN_3$) experiments, cells were treated with 1 mg/ml $NaN_3$ (Sigma-Aldrich) for the all the time of G exposure.

***Scanning and Transmission Electron Microscopy***.

For scanning electron microscopy (SEM) analysis, primary astrocytes treated with GR/GO nanosheets or with the respective vehicle for 24 h, 72 h and 7 days were fixed with 1.5% glutaraldehyde in 66 mM sodium cacodylate buffer and post-fixed in 1% $OsO_4$. Sample dehydration was performed by 5 min washes in 30%, 50%, 70%, 80%, 90%, 96% and 100% EtOH solutions. In order to fully dry the samples, overnight incubation with 99% hexamethyldisilazane (HMDS) reagent (#440191, Sigma-Aldrich) was performed. Before SEM acquisition, coverslips were sputter-coated with a 10 nm layer of 99% gold (Au) nanoparticles in an Ar-filled chamber (Cressington, Sputter Coater 208HR), and imaged using a JEOL JSM-6490LA scanning electron microscope. For transmission electron microscopy (TEM) analysis, astrocytes treated with GR/GO nanosheets or with the respective vehicle for 24 h, 72 h and 7 days were fixed with 1.2% glutaraldehyde in 66 mM sodium cacodylate buffer, post-fixed in 1% $OsO_4$, 1.5% $K_4Fe(CN)_6$ 0.1 M sodium cacodylate, en bloc stained with 1% uranyl acetate dehydrated and flat embedded in epoxy resin (Epon 812, TAAB). After baking for 48 h at 60 °C, the glass coverslip was removed from the Epon block by thermal shock using liquid $N_2$. Astrocytes were identified by means of a stereomicroscope, excised from the block and mounted on a cured Epon block for sectioning using an EM UC6 ultramicrotome (Leica Microsystem). Ultrathin sections (70 nm thick) were collected on copper mesh grids and observed with a JEM-1011 electron microscope operating at 100 kV and equipped with an ORIUS SC1000 CCD camera (Gatan Inc., Pleasanton, CA). For each experimental condition, at least 6 images were acquired at a magnification up to 10,000x. Electron microscopy experiments were performed by Dr. Bramini (IIT-NSYN, Genova).

***Patch-clamp electrophysiology.***

All experiments were performed using an EPC-10 amplifier controlled by the PatchMaster software (HEKA Elektronik, Lambrecht/Pfalz, Germany) and an inverted DMI6000 microscope (Leica Microsystems GmbH). Patch electrodes fabricated from thick borosilicate glasses were pulled to a final resistance of 4−5 MΩ. Recordings with leak current > 100 pA were discarded. All recordings were acquired at 50 kHz. Primary rat cortical astrocytes exposed for 72 h to GR/GO nanosheets (1 and 10 μg/mL) or to the respective vehicle were used for patch-clamp recordings. The standard bath saline contained (in mM): 140 NaCl, 4 KCl, 2 $MgCl_2$, 2 $CaCl_2$, 10 HEPES, 5 glucose, pH 7.4, with NaOH and osmolarity adjusted to ∼315 mOsm with mannitol. The intracellular (pipette) solution was composed of (in mM): 144 KCl, 2 $MgCl_2$, 5 EGTA, 10 HEPES, pH 7.2 with KOH; osmolarity ∼300 mOsm. Experiments were carried out at RT (20–24°C).

For co-culture experiments, primary rat cortical neurons were seeded on top of astrocytes previously exposed to GR/GO flakes for 72 h (10 μg/mL) or to the respective vehicle and used for patch-clamp experiments after 10 DIV. Recordings of evoked firing activity in current-clamp configuration were performed in Tyrode's extracellular solution in which D-(−)-2-amino-5-phosphonopentanoic acid (AP5, 50 μM), 6-cyano-7 nitroquinoxaline-2,3-dione (CNQX, 10 μM), bicuculline methiodide (BIC, 30 μM), and (2*S*)-3-[[(1*S*)-1-(3,4-Dichlorophenyl)ethyl]amino-2-hydroxypropyl](phenylmethyl) phosphinic acid hydrochloride (CGP, 5 μM) were added to block NMDA, non-NMDA, GABAA, and GABAB receptors, respectively. The internal solution (K-gluconate) was composed of (in mM): 126 K gluconate, 4 NaCl, 1 $MgSO_4$, 0.02 $CaCl_2$, 0.1 BAPTA, 15 glucose, 5 Hepes, 3 ATP, and 0.1 GTP, pH 7.3. Current-clamp recordings were

performed at a holding potential of −70 mV, and action potential firing was induced by injecting current steps of 10 pA lasting 500 ms. All parameters were analyzed using the Fitmaster (HEKA Elektronik,) and Prism6 (GraphPad Software, Inc.) software.

Spontaneous miniature excitatory postsynaptic (mEPSCs) currents and spontaneous miniature inhibitory postsynaptic (mIPSCs) currents were recorded in voltage-clamp configuration in the presence of tetrodotoxin (TTX, 300 nM) in the extracellular solution to block the generation and propagation of spontaneous action potentials. To isolate mEPSCs currents, 30 μM BIC was added to Tyrode's extracellular solution, in the presence of the internal solution (K-gluconate) described above. To isolate mIPSC currents, 10 μM CNQX was added to Tyrode's extracellular solution, in presence of internal solution composed of (in mM): 120 KGluconate, 4 NaCl, 20 KCl, 1 $MgSO_4$, 0.1 EGTA, 15 Glucose, 5 HEPES, 3 ATP, 0.1 GTP (pH 7.2 with KOH). mPSCs were acquired at 10 kHz sample frequency, filtered at half the acquisition rate with an 8-pole low-pass Bessel filter, and analyzed by using the Minianalysis program (Synaptosoft, Leonia, NJ, USA). The amplitude, frequency, rise time and decay time of mPSCs were calculated using a peak detector. All reagents were purchased from Sigma Aldrich or Tocris (Tocris, Avonmouth, Bristol, UK).

***Protein extraction and western blotting analysis***.

Total protein lysates were obtained from cells lysed in RIPA buffer (10 mM Tris-HCl, 1 mM EDTA, 0.5 mM EGTA, 1% Triton X-100, 0.1% sodium deoxycholate, 0.1% sodium dodecyl sulfate, 140 mM NaCl) containing protease and phosphatase inhibitor cocktails (Roche, Monza, Italy). The soluble fraction was collected and protein concentration was

determined using the BCA Protein Assay Kit (Thermo-Fisher Scientific). For Western blotting, protein lysates were denatured at 99 °C in 5X sample buffer (62.5 mM Tris-HCL, pH 6.8, 2% SDS, 25% glycerol, 0.05% bromophenol blue, 5% β-mercaptoethanol, deionized water) and separated on SDS-polyacrylamide gels (SDS-PAGE). The following antibodies were used: mouse monoclonal anti-LC3 (#0231, Nanotools, Teningen, Germany), mouse monoclonal anti-glial fibrillary acidic protein (GFAP, #G3893, Sigma-Aldrich), rabbit polyclonal anti-astrocyte potassium channel KIR4.1 (KIR4.1, #APC-035, Alomone) and rabbit polyclonal anti-glutamate transporter 1 (EAAT2, #3838, Cell Signaling Technology). Signal intensities were quantified using the ChemiDoc MP Imaging System (GE Healthcare BioSciences, Buckinghamshire, UK).

***Calcium imaging.***

Cultures were loaded for 30 min at 37 °C with 1 μg/ml cell-permeable Fura-2 AM (#F1221, ThermoFisher Scientific) in the culture medium. Cells were then washed in recording buffer (140 NaCl, 4 KCl, 2 $MgCl_2$, 2 $CaCl_2$, 10 HEPES, 5 glucose, pH 7.4, with NaOH) for 30 min at 37 °C to allow hydrolysis of the esterified groups. Coverslips with cells were mounted on the imaging chamber and loaded with 0.5 ml of recording buffer. Fura-2-loaded cultures were observed with an inverted epifluorescence microscope Leica DMI6000 (Leica Microsystems GmbH) using a 63x (1.4 NA) oil-immersion objective, and recordings were performed from visual fields containing 5 ± 2 astrocytes on average. During the analysis, we selected the cells by drawing regions of interest (ROI) around their bodies to reduce any background. Samples were excited at 340 and 380 nm by a mercury metal halide lamp, LEICA EL6000 (Leica Microsystems

GmbH). Excitation light was separated from the emitted light using a 395 nm dichroic mirror. Images of fluorescence emission > 510 nm were acquired continuously for a maximum of 2400 s (200 ms individual exposure time) by using a Hamamatsu Orca-ER IEEE1394 CCD camera (Hamamatsu Photonics, Hamamatsu City, Japan). The imaging system was controlled by an integrating imaging software package (Leica LAS AF software, Leica Application Suite Advance Fluorescence, version 3.3, Leica Microsystems). In order to monitor spontaneous $Ca^{2+}$ oscillations, astrocytes were recorded for 15 min under baseline conditions. For ATP (#A2383, Sigma-Aldrich) experiments, after 1 min of baseline acquisition, astrocytes were stimulated with 10 µM of ATP. For thapsigargin (#1138, Tocris), experiments, cells were perfused with a standard $Ca^{2+}$-free extracellular solution in which $Ca^{2+}$ was replaced with 5 mM EGTA, after 30 sec of baseline acquisition, 5 µM of thapsigargin was added. After $[Ca^{2+}]_i$ returned to baseline levels, EGTA was replaced by $CaCl_2$ (2 mM) in the extracellular medium to induce $Ca^{2+}$ entry.

Fluorescence intensity ratios (R) were calculated for the time course of the experiment according to the equation below:

$$R = \frac{MV\ (\lambda_x 340 - \lambda_e 510) - MV\ background}{MV\ (\lambda_x 380 - \lambda_e 510) - MV\ background}$$

where MV (mean value) is the average pixel intensity for each ROI, and λx-λe is the excitation (collection) wavelength. For quantitative analysis, the percentage total increase fluorescence signal (ΔF) was calculated by subtracting $F_0$ and ΔF, and normalized to $F_0$ fluorescence values.

***Glutamate uptake assay.***

For glutamate uptake experiments, astrocytes were plated at concentration of 1 x 10^5 cell/ml in 6 well plate. Astrocytes cultures were washed three times with pre-warmed (37°C) HEPES-buffered Hanks' balanced salt solution, 1 μCi/ml of l-[2.3-$^{3}$H]glutamate (NET490001MC, Perkin Elmer, Milan, Italy) was added to unlabeled l-glutamate (#G8415, Sigma) to a final concentration of 50 μM. To isolate $Na^{+}$-dependent transport, cultures were exposed to 1μCi/ml of l-[2.3-$^{3}$H]glutamate in the presence or absence of $Na^{+}$. In the $Na^{+}$-free buffer, NaCl was replaced by choline chloride (Sigma). To isolate Kir4.1 mediated glutamate uptake, 100 μM $Ba^{2+}$ (Sigma) was added to $Na^{+}$ solution. To block glutamate transporters 100 μM TBOA (Tocris) was added to $Na^{+}$ solution. Cultures were incubated with the isotope on a heating plate at 37°C for 10 min. After three washes with PBS, cells were harvested into 400 ml of 1 M NaOH solution. The samples for radioactivity detection were transferred to vials containing 2 ml of aqueous scintillation mixture and counted using a liquid scintillation counter (1450 LSC & Luminescence Counter, MicroBete TriLux, Perkin Elmer).

***Statistical Analysis.***

Data are expressed as means ± SEM of number of cells (n) and mouse preparations detailed in the figure legends. Normal distribution of data was assessed using the D'Agostino-Pearson's normality test (for n>8 values/experimental group) or the Kolmogorov–Smirnov test (n<8 values/experimental group). Significance level was preset to $p<0.05$. To compare two normally distributed sample groups, data were analyzed by the paired/unpaired Student's *t*-test or, in case of more than 2 experimental

groups, by one- or two-way analysis of variance (ANOVA) followed by the Bonferroni's *post-hoc* multiple comparison test. To compare two groups that were not normally distributed, the Mann–Whitney's non-parametric *U* test was used, while in case of more than 2 experimental groups, the Kruskal-Wallis test followed by Dunn's post hoc test was performed. Statistical analysis was carried out using the Prism (GraphPad) software.

# 5. RESULTS

## 5.1 GR and GO nanosheets induce morphological changes in primary astrocytes due to reorganization of cell cytoskeleton.

We firstly evaluated whether G nanosheets could alter glial morphology. To this end, parallel samples were processed for confocal laser-scanning microscopy (CLSM) using antibodies specific for the glial cytoskeleton (anti-glial fibrillary acidic protein; GFAP) and Hoechst staining to visualize nuclei, or subjected to scanning electron microscopy (SEM) (**Figure 1a**). Fluorescence microscopy revealed that exposure to G sheets induced a clear change in the shape of astrocytes that, from regular and flat-shaped (typical of non-activated *in vitro* cultured primary astrocytes), became irregular and characterized by multiple thin processes and elongated protrusions, resembling the morphology of *in vitro* activated/mature glia [142, 143]. To quantitatively analyze this phenomenon, we employed the circularity index (ImageJ) as measure of symmetry and regularity of the cell shape. **Figure 1b** shows that upon exposure to G nanosheets, astrocytes are characterized by a significantly lower index, indicative of a more elongated and asymmetrical shape.

The observed morphological transformation could be due to nanosheet-induced cytoskeletal reassembling [144], a phenomenon reported also for other carbon materials [145]. To confirm this hypothesis, astrocytes were fixed and stained after 72 h of G exposure using fluorescently labeled phalloidin to visualize actin filaments and antibodies for microtubules (anti-α-tubulin). Three-dimensional Z-stack images were acquired by CLSM, adopting the reflection light acquisition modality to visualize G

nanosheets [62, 146]. Control cells showed well-organized actin and tubulin filament bundles, in contrast, G nanosheets induced breakdown of actin fibers (**Figure 1c**) and rearrangement of α-tubulin that irregularly aggregated upon G exposure (**Figure 1 d)**. These data indicate that both GR and GO exposure alter the astrocyte cytoskeleton, driving the observed morphological changes.

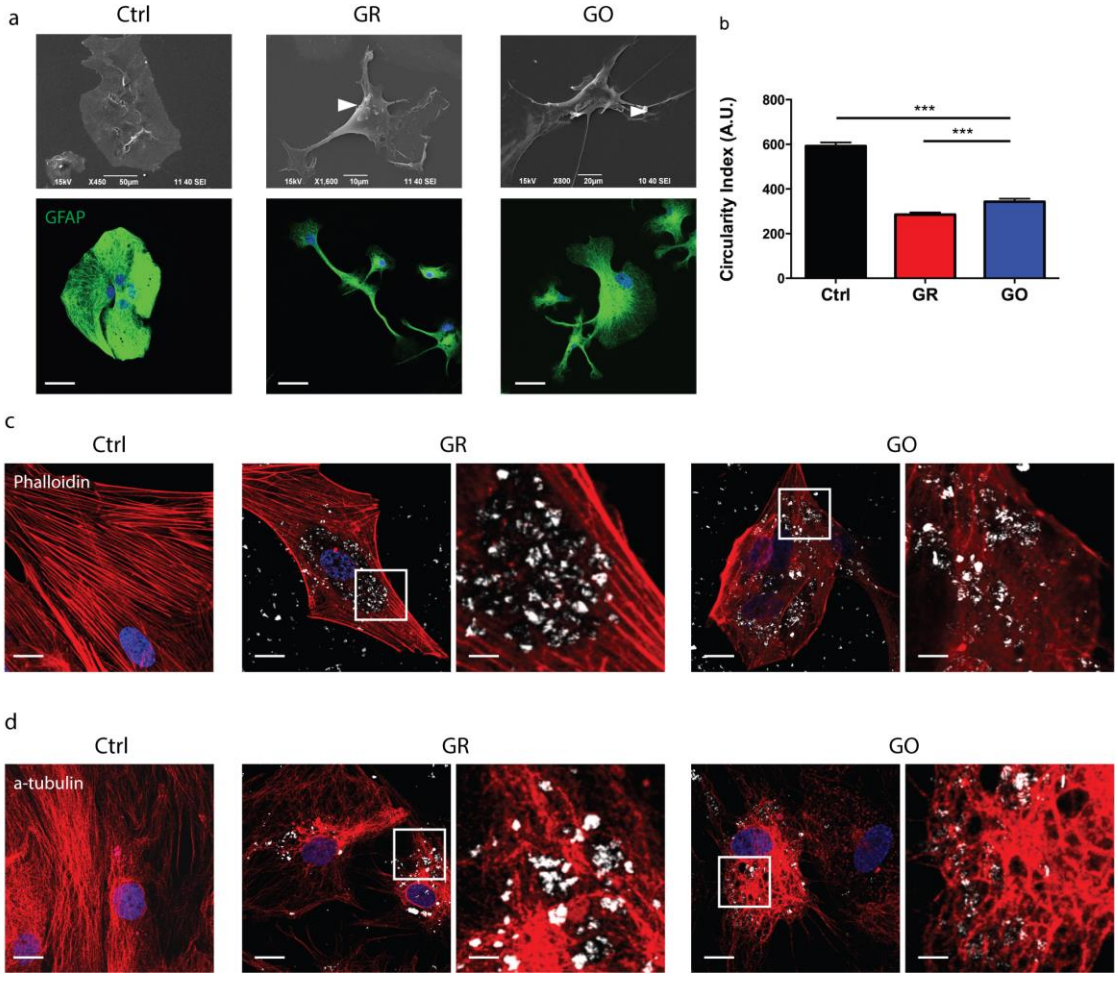


**Figure 1**. **Interactions of GR and GO nanosheets with primary astrocytes.** (**a**) GR and GO-induced changes in cell morphology were investigated by SEM and fluorescence microscopy. Astrocytes were exposed to GR and GO nanosheets for 72 h, fixed and prepared for either SEM

analysis or confocal immunostaining with anti-GFAP antibodies (green)/Hoechst33342 (blue). Few nanosheets could be seen in adhesion to the cell membrane (white arrowheads, upper panel). Cell morphology of astrocytes exposed to GR and GO nanosheets was severely affected when compared to untreated samples. Scale bars, 50 μm. (**b**) Mean ± SEM of circularity index for each experimental condition. ***p<0.001, one-way ANOVA and Bonferroni's multiple comparison test, n = 130 cells, from 3 independent cell preparations. (**c**,**d**) Confocal images of astrocytes fixed and stained with phalloidin to visualize actin filaments (red, upper panel) and anti-αtubulin (red, low panel). Scale bars, 5 μm and 1 μm for low and high magnification, respectively.

## 5.2 GR and GO nanosheets are mainly internalized through the endolysosomal pathway in the absence of autophagic reaction.

To get more insights on the intracellular localization of the internalized nanosheets, the uptake rate and fate of GR and GO nanosheets were firstly investigated by quantifying the percentage of material overlapping with GFAP fluorescence using CLSM. The vast majority of astrocytes were found to internalize GR and GO nanosheets, with a very high amount of uptaken nanosheets already at 24 h of exposure (**Figure 2a**; mean ± SEM: GR 40 ± 2.2%; GO 35 ± 1.1%). To identify the nature of the organelles containing the G nanosheets, we focused on the endo-lysosomal pathway, known to be the preferential route of entry of nanoparticles and nanomaterials [147-150]. Astrocytes were fixed after 24 h, 48 h and 7 days of G nanosheet exposure, and labelled with antibodies for early-endosomes (EEA1) and lysosomes (LAMP1). Three-dimensional Z-stack images were acquired and GR and GO were visualized using reflection light acquisition modality [62, 146]. Following this procedure, a precise quantification of nanosheet uptake and intracellular location was possible (**Figure 2b-e**). The evaluation of the co-localization ratios between G and EEA1 or LAMP1 over the total amount of intracellular G revealed that the material was internalized with a time-dependent transition from EEA1-positive

early endosomes (up to 72 h) to LAMP1-positive lysosomes (**Figure 2b-e**). These results are in line with previous studies describing the intracellular trafficking of nanomaterials in living systems [148-151].

To better investigate the physical interaction of GR and GO nanosheets with glial cells, transmission electron microscopy (TEM) was used. The nanosheets were identified by their characteristic laminated shape, high electron-dense structure and typical reflected bright shadow in their proximity [152, 153]. As shown in **Figure 2 f-h**, both GR and GO flakes (black arrowheads) were present inside cells as aggregates of various sizes and compactness, mainly localized within membrane-bound vesicles (**Figure 2g,h**), possibly belonging to the endo-lysosomal pathway. As discussed above, the non-homogenous nanosheets dispersion in solution may explain the formation of aggregates, although we cannot exclude that these agglomerates are formed inside cells, upon fusion of multiple vesicles into larger intracellular structures.

Finally, the expression and maturation of LC3, a marker of autophagosome membranes, were investigated by immunofluorescence and western blotting (data not shown). Our results showed complete absence of LC3 in GR/GO treated astrocytes, opposite to what we observed in primary neurons, which upon G nanosheet exposure display a strong autophagy response [62].

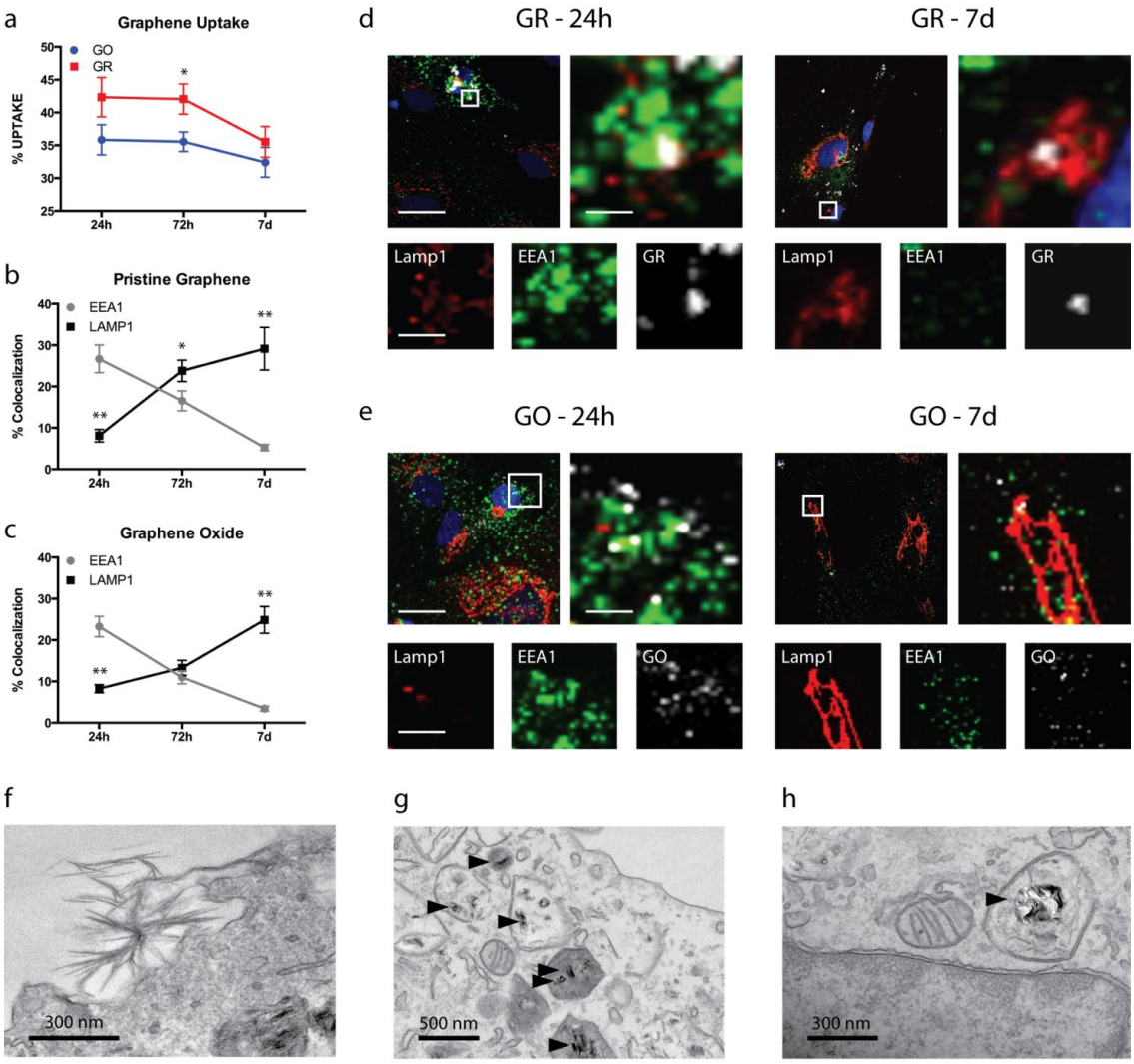


**Figure 2. Interactions of GR and GO nanosheets with primary astrocytes.**

(**a-e**) Internalization of G nanosheets in primary astrocytes. Primary rat astrocytes were exposed to GR or GO nanosheets (10 μg/ml) for 1, 3 and 7 days. Astrocytes were fixed and stained with anti-EEA1 and anti-LAMP1 antibodies for early endosome and lysosome identification, respectively, and Hoechst33342 for visualization of cell nuclei. (**d**, **e**) Astrocytes were imaged by confocal fluorescence microscopy and three-dimensional images were acquired (scale bars: 20 μm in main images, 2 μm in zoomed images, 5 μm in single-channel boxes). (**a**) Total internal GR and GO nanosheet internalization was quantified over time and expressed as percent uptake (mean±SEM) with respect to the total G-nanosheets profile. Quantification of the extent of co-localization of nanosheets with EEA1 (**b**) and LAMP1 (**c**) positive organelles analyzed using the

JACOP plugin of the ImageJ software (*p<0.05, **p<0.01, one-way ANOVA and Bonferroni's multiple comparison test, 50 cells from n = 3 coverslips per experimental condition, from 3 independent glial preparations). (**f-h**) The cell uptake of GR and GO and the intracellular location of G nanosheets were confirmed by TEM. Large nanosheets were found to be outside the cells in close proximity to the cell membrane (**f**). Large amounts of nanosheets (black arrowheads) were observed into intracellular vesicles, such as lysosomes (**g**) and larger lipid-containing vesicles (**h**).

## 5.3 Exposure to GO alters calcium dynamics in primary astrocytes.

As detailed in the Introduction, our proteomic analysis revealed a strong perturbation of the cellular pathways involved in $Ca^{2+}$ homeostasis. To better understand these changes, we exposed primary astrocytes to G nanosheets for 72 h and then we investigated the effects of GR/GO on $Ca^{2+}$ dynamics by live imaging using the ratiometric $Ca^{2+}$ indicator Fura2-AM (**Figure 3**). Both GR- and GO-treated cultures were characterised by significantly lower basal $Ca^{2+}$ levels, by a smaller number of cells showing spontaneous $[Ca^{2+}]_i$ transients (**Figure 3a,b,e)** as well as by a reduction in the frequency of $[Ca^{2+}]_i$ oscillations (**Figure 3c**), although these effects reached statistical significance only for GO-treated astrocytes. Similar results were obtained when $Ca^{2+}$ transients were evoked by stimulation of astrocytes with ATP, with a significantly impaired response by GO-treated astrocytes (**Figure 3d-f**).

To gain some insights into the mechanisms underlying the observed phenotype, we asked whether GO-exposure impairs the release of $Ca^{2+}$ from intracellular stores and/or the influx of $Ca^{2+}$ from the extracellular medium [154]. To address this issue, we exposed GO-treated astrocytes to thapsigargin, a blocker of the SERCA pump that transports cytosolic $Ca^{2+}$ into the endoplasmic reticulum, in $Ca^{2+}$-free extracellular medium, to promote the depletion of the intracellular $Ca^{2+}$ stores [155]. Interestingly,

under these conditions, GO-treated astrocytes showed an impaired response to thapsigargin, indicating defective $Ca^{2+}$ storage mechanism. In addition, when the extracellular $Ca^{2+}$ concentration was restored to 2 mM to assess $Ca^{2+}$ entry through the plasma membrane calcium release activated channels (CRAC), GO-treated astrocytes displayed only a moderate increase in $[Ca^{2+}]_i$, which was significantly lower than that evoked in control astrocytes (**Figure 3g,h**). These results suggest the existence of a complex dysregulation of $Ca^{2+}$ homeostasis and signalling in astrocytes exposed to GO nanosheets; the data are consistent both with the marked alterations of proteins involved in $Ca^{2+}$ signalling depicted by the proteomic screening, and with the observed alterations of cytoskeleton [156].

It is well known that cholesterol, a constituent of lipid raft, is involved in the signaling between endoplasmic reticulum and plasma membrane refilling [157]. To verify whether the GO-induced dysregulation of $Ca^{2+}$ homeostasis and signalling was associated with alteration in cholesterol content of the plasma membrane, we targeted membrane cholesterol by labelling primary astrocytes with the cholesterol-specific fluorescent marker filipin. Indeed, a significant two-fold increase in membrane cholesterol was observed in astrocytes treated with GO for 72 h with respect to control cultures (**Figure 4a, b**).

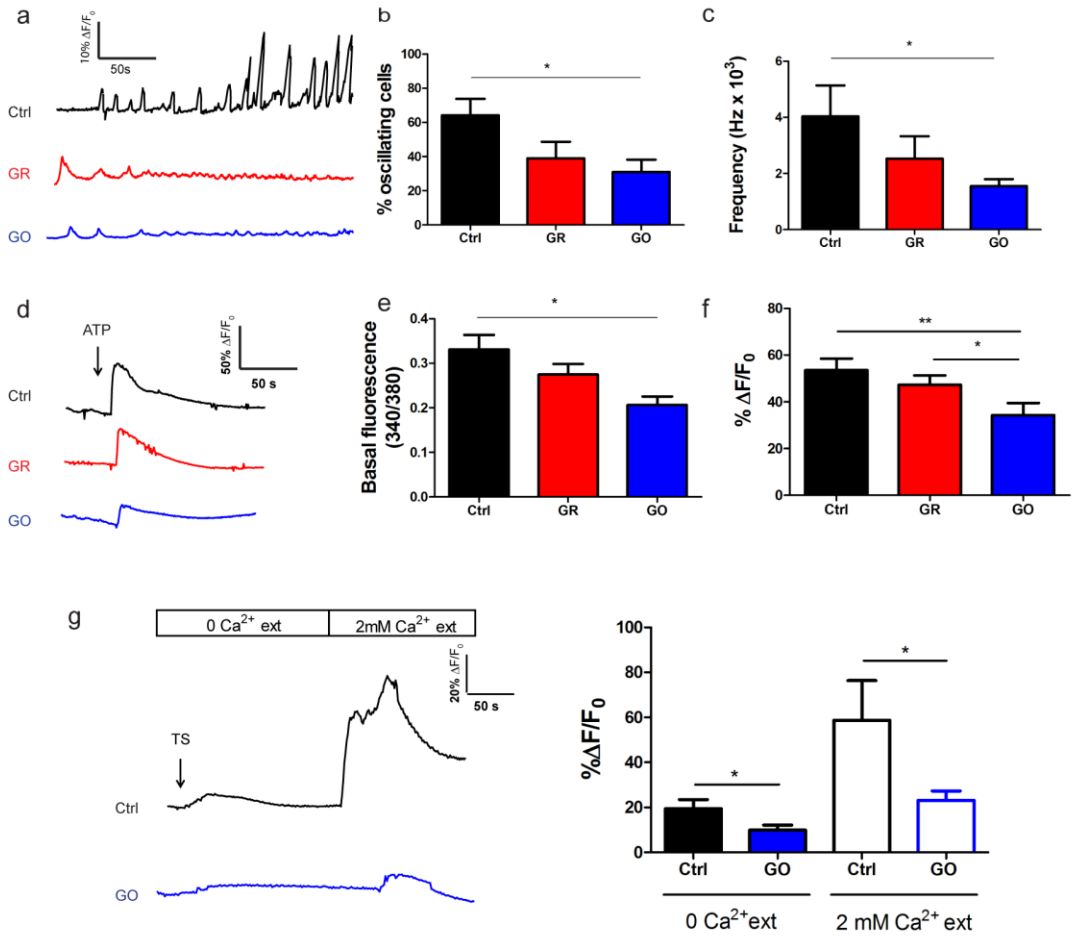


**Figure 3. $Ca^{2+}$ dynamics in primary astrocytes treated with GR and GO nanosheets.**

(**a**) Representative spontaneous $Ca^{2+}$ oscillations recorded in astrocytes treated with GR and GO nanosheets (10 μg/ml) for 72 h. Percentage of spontaneously active cells (**b**) and frequency of $Ca^{2+}$ oscillations (**c**) under basal conditions. Means ± SEM of n=10 coverslips per experimental condition from 4 independent glial preparations (Ctrl, n = 32; GR, n = 31; GO, n = 23 cells). *p < 0.05, one-way ANOVA/Bonferroni's multiple comparison tests. (**d**) Representative $Ca^{2+}$ responses evoked by ATP (10 μM) in astrocytes treated for 72 h with G-nanosheets. Quantification of the basal $Ca^{2+}$ levels (**e**) and changes in ΔF (i.e., $[F-F_0]/F_0$) values upon ATP addition (**f**). Means ± SEM of n=10 coverslips per experimental condition from 3 independent preparations (Ctrl, n = 21; GR, n = 25; GO, n = 21 cells). *p < 0.05, **p < 0.01 Kruskal-Wallis/Dunn's multiple comparison tests. (**g**) Representative traces of $Ca^{2+}$ transients (left) and changes in ΔF values triggered by thapsigargin (TS, 1 μM) in $Ca^{2+}$-free external medium (0 $[Ca^{2+}]_{ext}$) and after replacement of the external solution with $Ca^{2+}$-containing extracellular

medium (2 mM $[Ca^{2+}]_{ext}$). Means ± SEM of n=10 cells per experimental conditions from 3 independent preparations. *p < 0.05, Mann Whitney *U*-test.

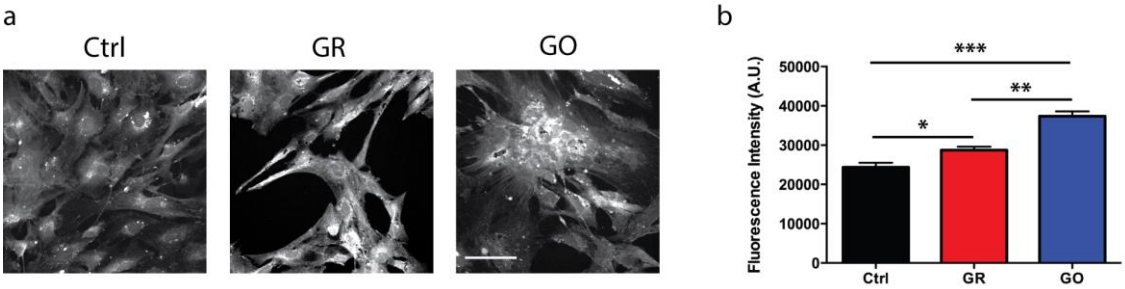


**Figure 4. Cholesterol content after GR and GO exposure.** (**a**) Filipin staining was performed to investigate the cholesterol membrane distribution in untreated astrocytes (Ctrl) and astrocytes exposed to GR and GO nanosheets for 72 h. Cells were imaged by CLSM; scale bars, 20 μm. (**b**) Astrocytes treated with GR and GO displayed higher levels of filipin staining compared to control samples (means ± SEM are shown; *p<0.05, **p<0.01, ***p<0.001; one-way ANOVA and Bonferroni's multiple comparison test; n = 30 cells from 2 independent primary glial preparations).

## 5.4 Differential effects of GR and GO on the electrical membrane properties of cultured primary astrocytes.

To assess whether GR and GO nanosheets affect astrocyte electrical membrane properties, we recorded $K^+$ currents before and after chronic exposure to either GR or GO (1-10 µg/ml; 72 h) or their respective vehicles. It is well known in fact that cultured astrocytes express mainly outward rectifying $K^+$ channels and, only upon their functional differentiation, they acquire a more physiological $K^+$ current profile, owing to the additional expression of inward rectifier $K^+$ channels (Kir) [158, 159]. Astrocytes were voltage clamped at a holding potential of −60 mV and were challenged with a voltage ramp or step protocol (inset to **Figure 5a,b**). Typical current traces elicited with both protocols in astrocytes exposed to GR are shown in **Figure 5a,b**. The results show that the treatment with GR did not significantly affect the amplitude and slope of the ramp currents. Current density measured at 120 mV was not significantly different between GR-treated and vehicle-treated samples (25.1 ± 4.8 pA/pF for Ctrl, 29.4 ± 6.7 pA/pF for GR) (**Figure 5c)**. Addition of barium ($Ba^{2+}$, 100 µM), which prevalently blocks inwardly rectifying $K^+$ channels [160], slightly inhibited (~ 20%) the current response at 120 mV to a similar extent in vehicle- and GR-treated astrocytes (**Figure 5d**). To unveil the time-dependent kinetics of the elicited current, we then applied a step protocol. Upon step depolarization, rapidly activating and non-inactivating outward currents typical of delayed rectifier $K^+$ conductance were evoked at potential more positive than -20 mV (**Figure 5e**). The voltage and temporal kinetics of the currents were not significantly different in vehicle- and GR-treated cells. Finally, analysis of the current-voltage relationship depicted a similar voltage-dependent profile between vehicle- and GR-

treated astrocytes (**Figure 5e**). Compared to vehicle-treated astrocytes, GR exposure did not affect the resting membrane potential (-28 ± 6 mV for Ctrl, -35 ± 5 mV for GR), the input resistance (686 ± 51 MΩ for Ctrl, 756 ± 133 MΩ for GR), and the specific conductance (0.037 ± 0.005 nS/pF for Ctrl, 0.038 ± 0.005 nS/pF for GR) (**Figure 5f-h**).

By contrast, an increase in outward rectifying current was observed in GO-treated astrocytes compared to vehicle-treated cells (**Figure 5i,j**). Analysis of current density values recorded at 120 mV showed an almost three-fold increase in GO-treated cells (26.9 ± 5.4 pA/pF for Ctrl, 67.1 ± 11.4 pA/pF for GO) (**Figure 5k**). Moreover, administration of $Ba^{2+}$ produced a significantly larger (~ 40%) decrement of the ramp current measured at 120 mV compared to vehicle-treated astrocytes (**Figure 5l**). The time and voltage-dependent kinetics of the current evoked with the voltage stimulation protocol (**Figure 5m**) were similar under the two experimental conditions. The analysis of the current-voltage relationships shows that in GO-treated astrocytes there was an increment in current amplitude at negative membrane potentials (**Figure 5m**). Moreover, astrocytes exposed to GO nanosheets had a more hyperpolarized membrane potential (-30.9 ± 6.5 mV for Ctrl and -50 ± 8 mV for GO), displayed a significant decrease in input resistance (706 ± 50 MΩ for Ctrl, 487 ± 67 MΩ for GO), and an increase in specific conductance (0.03 ± 0.003 nS/pF for Ctrl, 0.06 ± 0.01 nS/pF for GO) (**Figure 5n-p**). Similar results were obtained with lower doses (1 μg/ml) of GO, highlighting the specificity of this effect (**Figure 6**). These data suggest that $Ba^{2+}$ sensitive, weakly rectifying Kir channels, which are upregulated in differentiated cultured cortical astrocytes, may be responsible for mediating, at least in part, the increase in outward current and the variation in passive membrane currents depicted in GO-treated astrocytes.

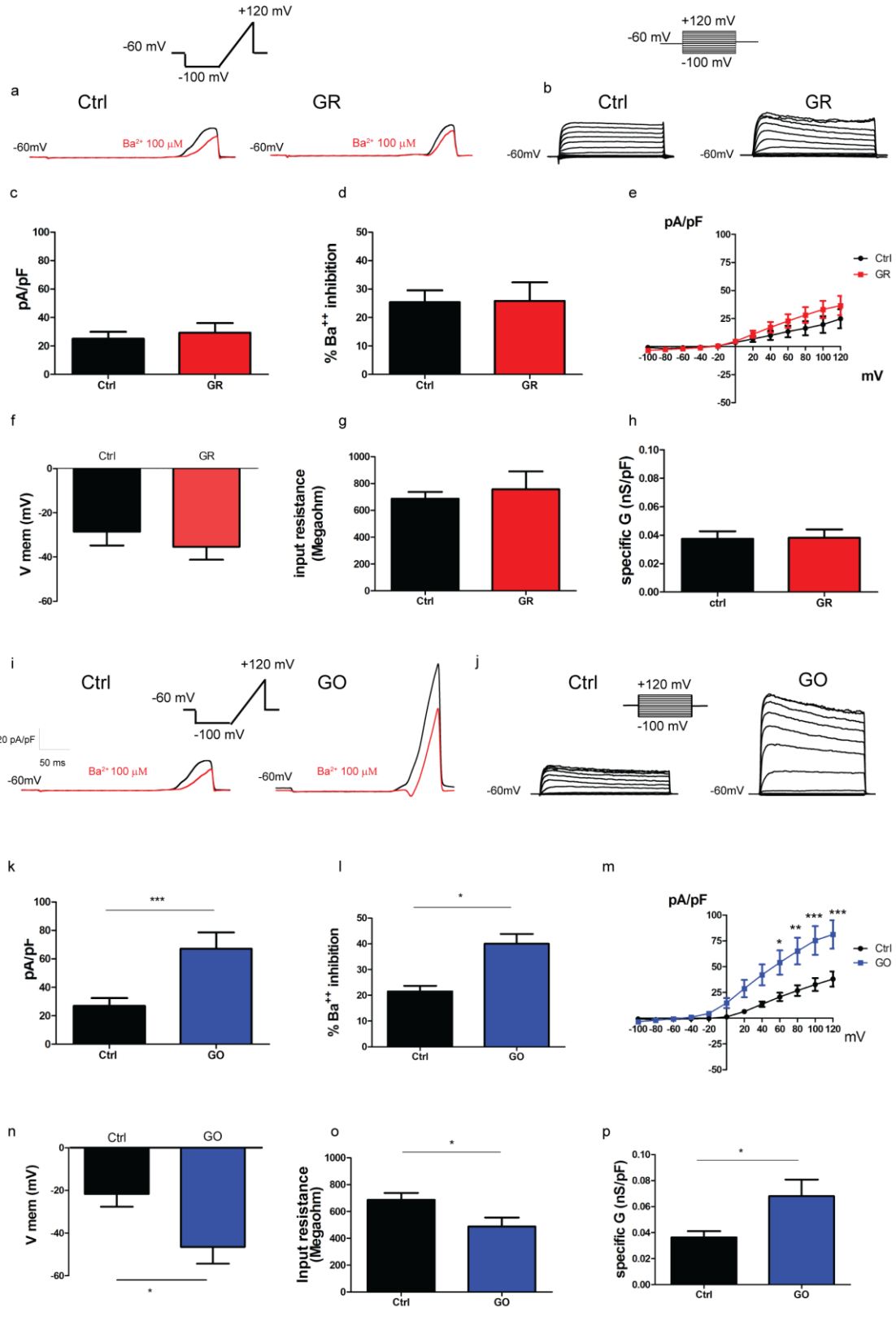
+120 mV
-60 mV
-100 mV
a
Ctrl
GR
-60mV
Ba2+ 100 µM
b
c
pA/pF
d
% Ba++ inhibition
e
pA/pF
Ctrl
GR
mV
f
V mem (mV)
g
input resistance (Megaohm)
h
specific G (nS/pF)
ctrl
i
GO
20 pA/pF
50 ms
j
k
l
m
n
o
Input resistance (Megaohm)
p

**Figure. 5. Electrophysiological properties of astrocytes upon GR and GO nanosheet exposure.**

(**a,b**) Whole-cell patch clamp recordings of primary astrocytes exposed to GR. (**a**) Representative current traces evoked with a voltage ramp protocol in astrocytes treated for 3 days with either GR (10 µg/ml) or vehicle before (black traces) or after the addition of $Ba^{2+}$ (100 µM, red traces) to the recording medium. (**b**) Representative traces of whole-cell currents evoked with a family of voltage steps in astrocytes treated with GR (10 µg/ml) or vehicle. (**c-e**) GR exposure does not affect the characteristics of outward currents in astrocytes. (**c**) Mean ± SEM of current density values at 120 mV (n = 19 cells from 3 independent preparations). (**d**) Mean (± SEM) percentage of current inhibition at 120 mV after application of 100 µM $Ba^{2+}$ (n = 10 cells per experimental condition). (**e**) Current-voltage relationships in astrocytes exposed to GR (red) or vehicle (black). Data are plotted as means ± SEM (n = 12 cells from 3 independent preparations). (**f-h**) Electrophysiological properties of astrocytes treated for 72 h with GR (10 µg/ml). The parameters describing the passive membrane properties of astrocytes, i.e. resting membrane potential (mV; **f**) mean input resistance (MΩ; **g**), specific conductance (ns/pF; **h**), showed no significant changes. Means ± SEM of n = 19 cells per experimental condition from 3 independent preparations. (**i-p**) Whole-cell patch-clamp recordings of primary astrocytes exposed to GO. (**i**) Representative current traces evoked with a voltage ramp protocol in astrocytes treated for 72 hrs with either GO (10 µg/ml) or vehicle before (black traces) or after the addition of $Ba^{2+}$ (100 µM, red traces) to the recording medium. (**j**) Representative traces of whole-cell currents evoked with a family of voltage steps in astrocytes treated with GO (10 µg/ml) or vehicle. (**k-m**) GO exposure markedly increases outward $K^+$ conductance in astrocytes. (**k**) Mean ± SEM current density values at 120 mV. ***p< 0.001 Mann-Whitney *U*-test (n = 19 cells from 3 independent preparations). (**l**) Mean (± SEM) percentage of current inhibition at 120 mV after application of 100 µM $Ba^{2+}$. *p < 0.05 two-tailed Student's *t*-test (n = 10 cells per experimental condition). (**m**) Current-voltage relationships in astrocytes exposed to GO (red) or vehicle (black). Data are plotted as means ± SEM (n = 12 cells from 3 independent preparations). (**n-p**) GO exposure for 72 h affects the passive membrane properties of astrocytes. Resting membrane potential (mV; **n**), mean input resistance (MΩ; **o**), specific conductance (ns/pF; **p**), are shown as means ± SEM of n = 19 cells per experimental condition from 3 independent preparations. *p < 0.05, two-tailed Student's *t*-test.

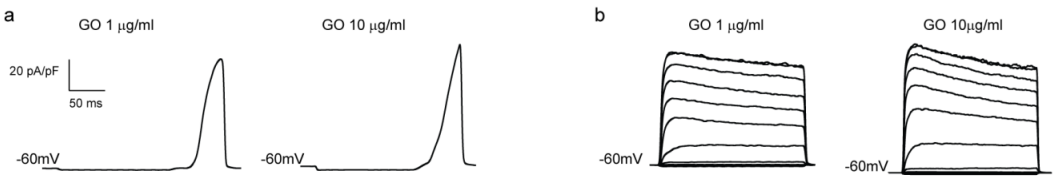


c

| | Resting membrane potential (mV) | Input Resistance (MΩ) | Specific G (ns/pF) | Current density +120mV (pA/pF) |
|---|---|---|---|---|
| GO 1 μg/ml | -43,1 ±4,1 | 574,7±73,1 | 0,05 ± 0,01 | 77,9 ± 13,4 |
| GO 10 μg/ml | -46,5 ± 7,8 | 487,7 ± 67,8 | 0,06 ± 0,01 | 67,1 ± 11,4 |

**Figure 6. Modulation of outward currents in astrocytes treated with 1 and 10 μg/mL of GO nanosheets.**

(**a,b**) Representative traces of whole-cell currents evoked in astrocytes treated for 72 h with GO (1 and 10 μg/ml) with a voltage ramp protocol (**a**) or a voltage-step protocol (**b**). (**c**) Summary of the mean (± SEM) passive membrane properties of astrocytes treated for 72 h with 1 and 10 μg/ml GO. No significant changes were observed as a function of the GO concentration (1μg/ml GO, n=10; 10 μg/ml GO, n=19; from 3 independent preparations).

## 5.5 GO effects on electrical membrane properties of cultured astrocytes are linked to the enhanced expression of Kir 4.1 channel.

We next investigated whether the expression of Kir 4.1 channels, the main component of Kir current in astrocytes [76], was affected by G exposure. Primary astrocytes treated with either GR or GO nanosheets were stained with anti-Kir 4.1 antibodies. The fluorescence intensity was quantified in comparison with vehicle-treated samples (**Figure 7a**,**b**). By avoiding the permeabilization step in the immunostaining procedure, we were able to monitor the expression of Kir 4.1 channels only on the plasma membrane, which represents the pool of functional channels. The results indicate that Kir 4.1 membrane labelling was markedly more intense and widespread in GO-treated astrocytes, whereas it

was indistinguishable from control astrocytes in GR-treated cells (**Figure 7a**,**b**). To confirm the immunofluorescence results, GO-treated and control astrocytes were solubilized and subjected to Western blotting for Kir 4.1. The total cell expression of Kir 4.1 was increased upon exposure to GO nanosheets, with a significant upregulation of both the monomeric and tetrameric forms of the channel (**Figure 7c-e**). These data confirm that the increase in outward current and the variation in passive membrane currents in GO-treated astrocytes can be attributed to the enhanced expression of Kir 4.1 channel.

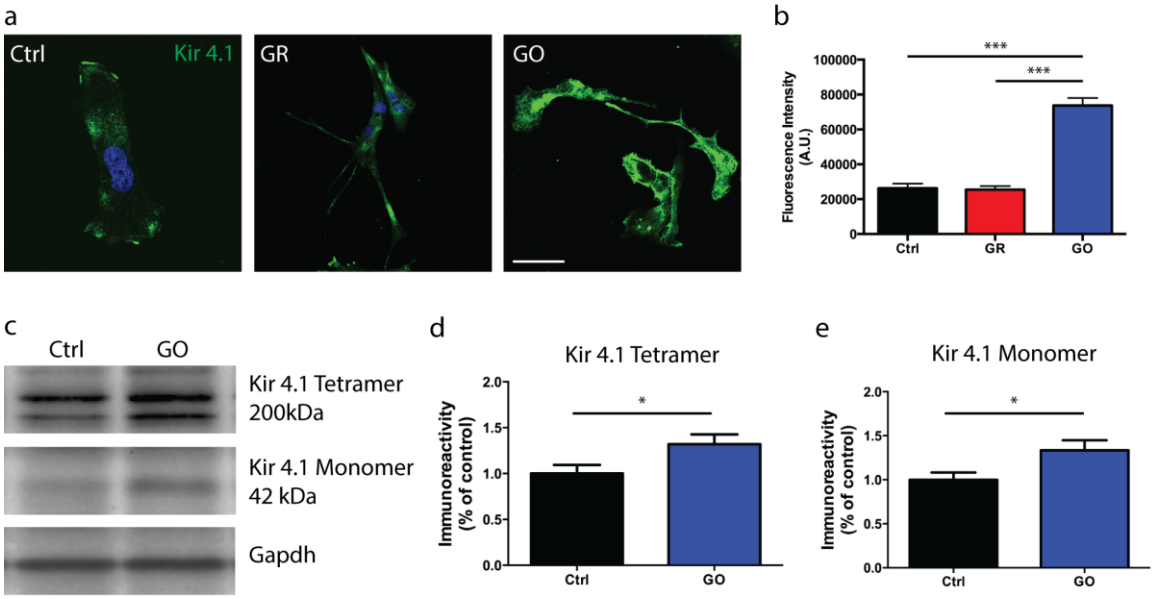


**Figure 7. Kir 4.1 channel expression is increased in astrocytes upon exposure to GO nanosheets.** (**a,b**) Primary astrocytes were exposed to GR and GO nanosheets (10 μg/ml) for 72 h, fixed and stained with anti-Kir 4.1 antibodies and Hoechst33342. (**a**) Astrocytes were imaged by confocal fluorescence microscopy and three-dimensional images were acquired (scale bars, 20 μm). (**b**) The mean ± SEM intensity of Kir 4.1 immunoreactivity was calculated for each experimental condition. ***p<0.001, one-way ANOVA/Bonferroni's multiple comparison tests (n = 40 cells from n = 2 coverslips per experimental condition from 2 independent preparations). (**c-e**) The overexpression of Kir 4.1 upon GO nanosheets exposure was confirmed by Western

blotting. (**c**) A representative experiment is shown, in which the tetrameric and monomeric forms of Kir 4.1 are electrophoretically resolved. Gapdh was used as loading control. Quantitative densitometry analysis of the immunoblots (means ± SEM) shows the overexpression of both the tetrameric (**d**) and monomeric (**e**) forms of Kir 4.1. *p< 0.05, two-tailed Student's *t*-test (n = 3 from 3 independent preparations).

Kir 4.1 channels control extracellular homeostasis through the regulation of glutamate dynamics. In rat, the expression of Kir 4.1 has been linked to a positive modulation of glutamate clearance by astrocytes mediated by the $Na^+$-dependent uptake through the GLT-1 transporter [112, 134]. To address the possibility that the increase in Kir 4.1 current could increase glutamate clearance, we evaluated the ability of cultured astrocytes to uptake tritium-labeled glutamate ($^3$H-Glu). Cultured astrocytes were exposed to GR or GO nanosheets for 72 h and then incubated with a mixture of labeled/unlabeled glutamate in Hank's buffer, in the presence or absence of choline (to isolate the $Na^+$-dependent glutamate transport) or following administration of $Ba^{2+}$ (to inhibit Kir 4.1 channels) (**Figure 8a**). Interestingly, while GR did not promote any variation in glutamate uptake compared to control, GO-treated astrocytes showed a marked increase in their ability to clear glutamate. Importantly, in GO-treated cells both the replacement of $Na^+$ and the challenge with $Ba^{2+}$ diminished the glutamate uptake to the same extent as the treatment with 100 μM dl-threo-β-benzyloxyaspartic acid (DL-TBOA), which is a competitive blocker of glutamate transporters [161], indicating the strong contribution of Kir 4.1 to the $Na^+$-dependent uptake of glutamate. We next investigated whether the increase in glutamate uptake could be due to enhanced expression of the GLT-1 transporter. Immunofluorescence analysis of treated and control cultures evidenced an increase in GLT-1 fluorescence in GO-treated astrocytes (**Figure 8b**), which was not evident in GR-

treated astrocytes. In summary, these data support the view that the long-term challenge of cultured cortical astrocytes with GO produces an increment of their homeostatic capacity by regulating various cellular mechanisms involved in extracellular glutamate dynamics.

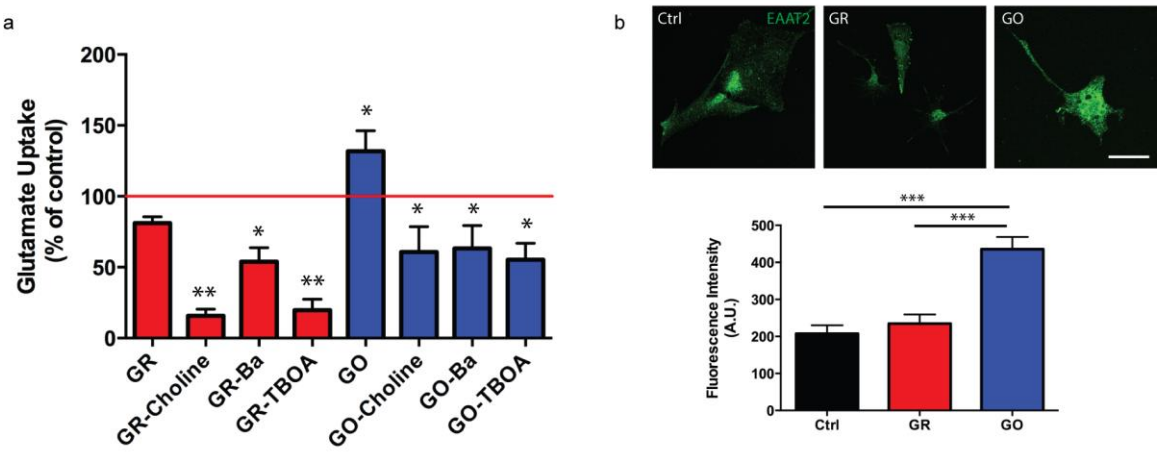


**Figure 8. Glutamate uptake is enhanced in GO-treated astrocytes.** (**a**) Quantitative analysis of glutamate uptake of astrocytes after 72 h of GR and GO exposure. Data are normalized to untreated samples. Mean ± SEM of n = 3 independent preparations. *p<0.05, **p< 0.01 One-way ANOVA and Bonferroni's multiple comparison test. (**b**) Representative images (upper panel, scale bar, 20μM) and quantification of EAAT2 immunoreactivity for each experimental conditions (lower panel). ***p<0.001 vs control samples, One-way ANOVA and Bonferroni's multiple comparison test. Data are expressed as mean ± SEM of n = 30 cells, from 2 independent preparations.

## 5.6 GO nanosheets internalization causes shape changes and Kir 4.1 channel upregulation in primary astrocytes.

The effects of G nanosheets on the shape and electrical properties of primary astrocytes could be in principle attributable to membrane shear stress induced by macro-flakes adhering to the external surface of the membrane, or to active internalization of nanosheets. In the attempt to discern between these two possibilities and investigate a mechanistic explanation for the biological effects induced by GO, we examined the effects of G exposure under conditions in which nanosheet internalization is prevented. As a general non-specific blocker of endocytosis we used sodium azide, an ATPase inhibitor that is commonly used to block cell metabolism [162]. Primary astrocytes were pre-treated with low doses of sodium azide that inhibit endocytosis but do not cause cell death, and subsequently exposed to either GR or GO nanosheets for 72 h. Cells were then either fixed and processed for immunofluorescence (**Figure 9a-e**), or lysed and subjected to Western blotting for Kir 4.1 (**Figure 9f-h**). As reported above, exposure to either GR or GO nanosheets induced a shape change characterized by a sharp decrease of the circularity index, while the sodium azide treatment *per se* did not alter the shape with respect to vehicle-treated astrocytes. Interestingly, sodium azide treatment substantially rescued the shape and circularity index of astrocytes treated with both GR and GO (**Figure 9b-d**), a result likely due to the reduced flake internalization (**Figure 9c-e**). Notably, sodium azide pretreatment completely antagonized the upregulation of Kir 4.1, without altering its expression in vehicle-treated cells (**Figure 9f-h**). These results directly link GR/GO internalization to the observed changes in astrocyte shape and

plasma membrane $K^+$ conductance, suggesting the uptake of the material is triggering the observed changes in physiological activity.

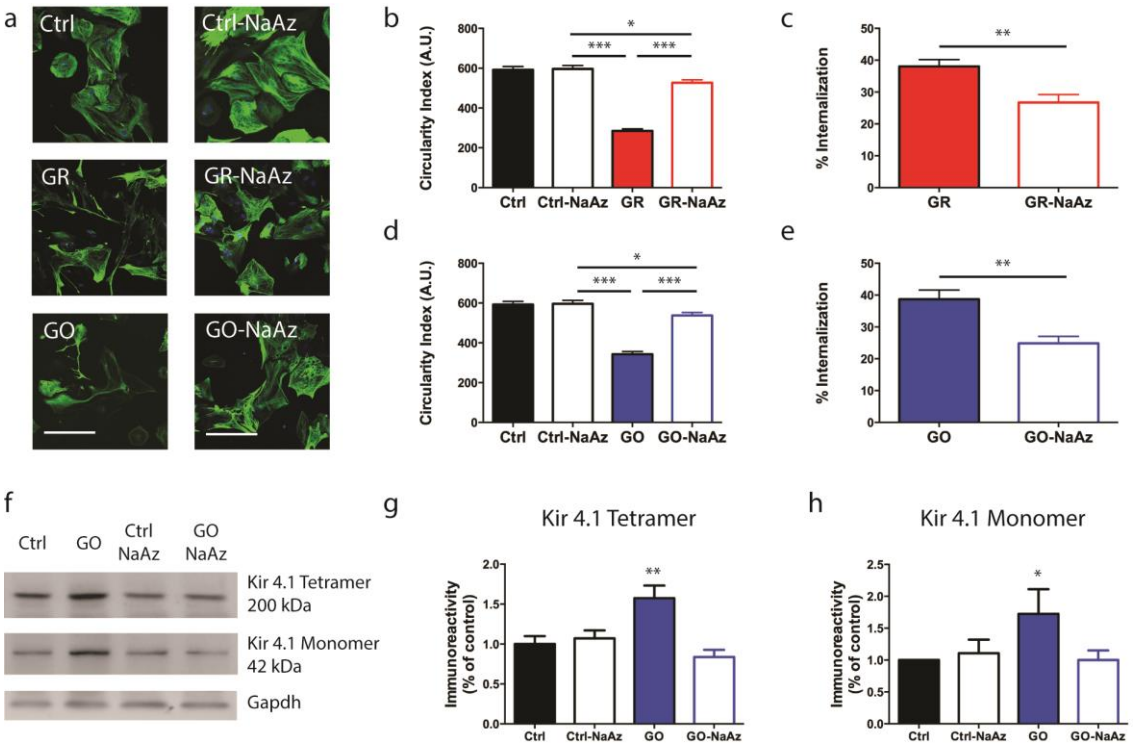


**Figure 9. Block of endocytosis with sodium azide reduces the internalization of GR and GO nanosheets, and rescues astrocyte shape changes and GO-induced Kir 4.1 channel overexpression.**

(**a**) Primary rat astrocytes were exposed to either GR or GO nanosheets (10 μg/ml) for 72 h with or without prior incubation with 0.05% sodium azide (NaAz). Astrocytes were stained for GFAP and Hoechst33342 and imaged by CLSM. Representative three-dimensional images are shown (scale bars, 50 μm). (**b-e**) The circularity index was quantified as a measure of the shape change of cells after GR (**b**) or GO (**d**) exposure. The amount of internalization of GR (**c**) and GO (**e**) flakes was also quantified. Means ± SEM. *p<0.05, ***p<0.001, one-way ANOVA/Bonferroni's multiple comparison tests (n = 100 cells from n = 2 coverslips per experimental condition, from 2 independent preparations). (**f-h**) The expression of Kir 4.1 upon GO exposure with or without prior incubation with NaAz was investigated by Western blotting. (**f**) A representative immunoblot is shown with the resolved tetrameric and monomeric species of Kir 4.1 and Gapdh

used as loading control. Quantitative densitometric analysis of the immunoblots (means ± SEM) shows that the increased levels of both tetrameric (**g**) and monomeric (**h**) species of Kir 4.1 are rescued upon NaAz treatment. *p<0.05, **p<0.01, two-tailed Student's *t*-test (n = 3 from 3 independent preparations).

## 5.7 Astrocytes primed for 72 h with GO nanosheets alter inhibitory synaptic transmission and intrinsic excitability of co-cultured primary cortical neurons.

Astrocytes secrete factors involved in synaptogenesis, regulating the number of synapses [90, 91], postsynaptic activity [92] and presynaptic neurotransmitters release [93]. In addition, astrocytes are fundamental for maintaining brain homeostasis, and the dysregulation of $K^+$ and glutamate uptake is linked to alteration of neuronal excitability and to the onset of neural disorders [163, 164]. Thus, having characterized the alteration of glia morphology and functionality by G nanosheet internalization, we extended our studies to an astrocyte-neuron co-culture system in order to understand the indirect effect of G exposure, by determining the influence of astrocyte dysregulation on neuronal cells.

To determine the effect of G-treated astrocytes on neuronal synaptic transmission and synaptic density, glial cells were treated with GR and GO nanosheets for 72 h, and then primary cortical neurons were plated on top of the astrocyte layer. We performed patch clamp recordings in neuronal cells at 10 DIV to monitor the frequency and amplitude of miniature excitatory (mEPSCs) and inhibitory (mIPSCs) postsynaptic currents. We found that the frequency and amplitude of mEPSCs were similar to control co-cultures under all the experimental conditions (**Figure 10a-f**). Double-staining of cortical neurons with antibodies for β-III tubulin to identify neuronal processes and the

vesicular glutamate transporter VGLUT1 to label excitatory synaptic contacts, revealed no difference in the density of excitatory synaptic contacts, supporting the electrophysiological data (**Figure 10g**). Surprisingly, we found a significant increase in mIPSCs frequency in GO samples in comparison with GR and control samples, in the absence of changes in the amplitude and in the current rise and decay times (**Figure 10h-l**). To determine whether the changes in frequency were determined by an increase in the density of inhibitory synapses, we co-immunostained for β-III tubulin and VGAT to label inhibitory boutons, and found an higher density of inhibitory synaptic boutons in GO-treated samples compared to GR-treated and control samples. These studies indicate that GO nanosheets influence the ability of astrocytes to promote formation and maturation of inhibitory GABAergic synapses (**Figure 10m**).

We next assessed the intrinsic excitability of neurons in the co-culture system, a measure of maturation of voltage-dependent conductances in developing neurons. We performed patch-clamp recordings in current-clamp configuration by injecting constant current pulses of 500 ms of increasing amplitude of 10 pA and measuring the resulting action potential firing rate. The analysis of firing rate *versus* injected current revealed that GO treated astrocytes significantly enhanced the mean neuronal firing activity and the mean instantaneous firing frequency evoked by depolarizing current pulses in co-cultured neurons (**Figure 11a-c**). To better analyze the shape of the action potentials, we generated phase-plot graphs by plotting the first derivative of the membrane potential over time (d*V*/d*t*) *versus* membrane potential. The first component of the phase plot is due to spike initiation in the axon initial segment (AIS) and to its fast antidromic propagation to the soma that generates a sudden voltage increase from baseline called '*kink*'[165].

The invasion of the soma by the AIS spike generates a delayed activation of $Na^+$ channels in the somatodendritic portions that leads to the second component of phase-plot, the somatodendritic spike. Interestingly, phase-plots revealed a more prominent '*kink*' in GO treated samples (**Figure 11d**). To quantify such differences, the changes in the kink were quantified by a linear regression fit of the 10 experimental points that follow the threshold, set at 5 mV/ms [165]. This analysis showed that the phase-slope was significantly increased in GO-treated samples (**Figure 13e**). Altogether, these results suggest that GO-treated astrocytes are able to influence the intrinsic excitability of cortical neurons by affecting voltage-gated channels expressed not only in the cell soma, but also at the AIS.

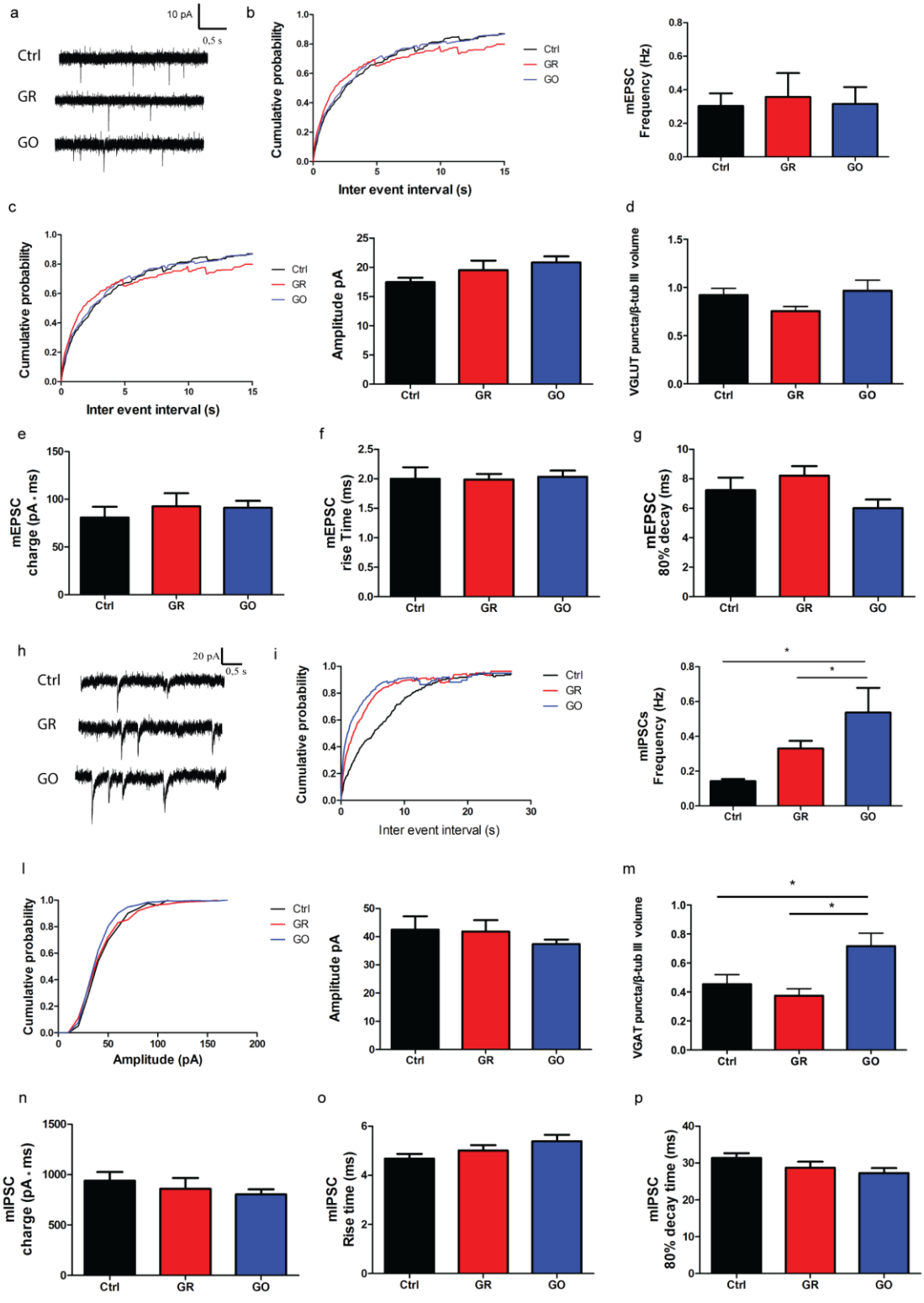
a
10 pA
0,5 s
Ctrl
GR
GO
b
Cumulative probability
Inter event interval (s)
Ctrl
GR
GO
mEPSC Frequency (Hz)
c
Cumulative probability
Inter event interval (s)
Amplitude pA
d
VGLUT puncta/β-tub III volume
e
mEPSC charge (pA . ms)
f
mEPSC rise Time (ms)
g
mEPSC 80% decay (ms)
h
20 pA
0,5 s
i
Cumulative probability
Inter event interval (s)
mIPSCs Frequency (Hz)
l
Cumulative probability
Amplitude (pA)
Amplitude pA
m
VGAT puncta/β-tub III volume
n
mIPSC charge (pA . ms)
o
mIPSC Rise time (ms)
p
mIPSC 80% decay time (ms)

**Figure 10. Astrocytes primed for 72h with GO nanosheets affect spontaneous activity of primary neurons.**

(**a-g**) Effects of GR and GO-treated astrocytes on miniature excitatory postsynaptic currents (mEPSCs). (**a**) Representative recordings of mEPSCs. (**b**) Cumulative distribution of inter-event intervals and mean ± SEM of mEPSCs frequency. (**c**) Cumulative distribution and mean ± SEM of mEPSC amplitude. (n = 10 cells from Ctrl, n = 10 cells for GR, n = 15 cells for GO, from 3 independent preparations). (**d**) Density of VGLUT1-positive excitatory synapses (n = 30 cells, from 3 independent preparations). Mean ± SEM of mEPSC charge (**e**) rise (**f**) and decay time (**g**) (n = 10 cells from Ctrl, n = 10 cells for GR, n = 15 cells for GO, from 3 independent preparations). No statistically significant differences were observed amongst the various experimental groups. (**h-p**) Effects of GR/GO-treated astrocytes on miniature inhibitory postsynaptic currents (mIPSCs). (**h**) Representative recordings of mIPSCs. (**i**) Cumulative distribution of inter-event intervals and mean ± SEM frequency of mIPSCs (*$p<0.05$, one-way ANOVA and Bonferroni's multiple comparison test, n = 10 cells per experimental condition from 3 independent preparations). (**l**) Cumulative distribution and mean ± SEM of mIPSC amplitude. (**m**) Density of VGAT-positive inhibitory synapses (n = 30 cells, from 3 independent preparations; *$p<0.05$, one-way ANOVA and Bonferroni's multiple comparison test). Mean ± SEM of mIPSC charge (**n**) rise (**o**) and decay time (**p**). No statistically significant differences were observed (n = 10 cells per experimental condition from 3 independent preparations).

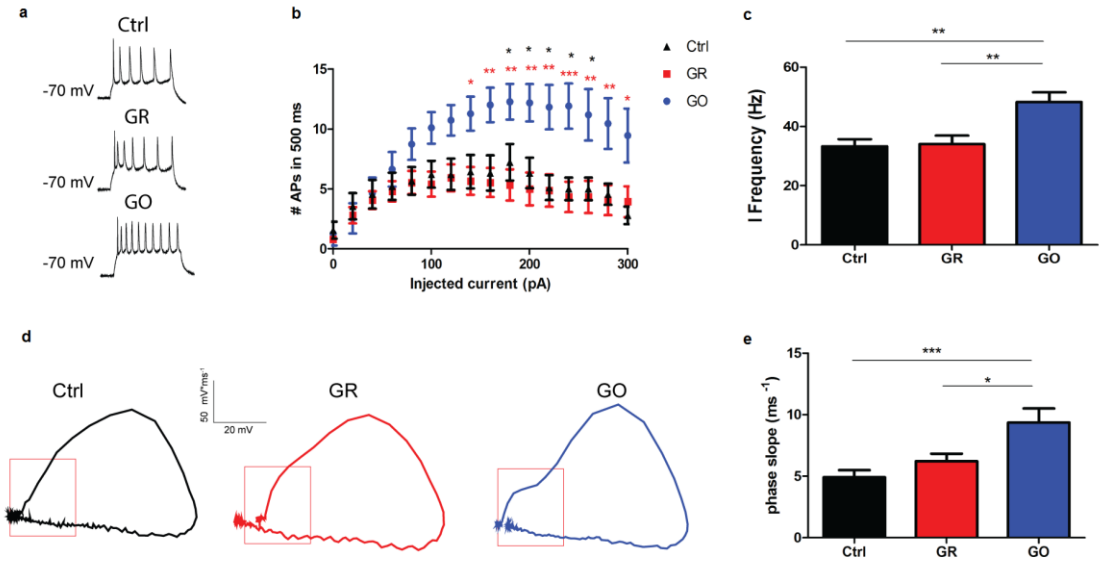


**Figure 11 Astrocytes primed for 72 h with GO nanosheets affect intrinsic excitability of primary neurons.**

(**a**-**c**) Effects of GR and GO-treated astrocytes on the firing properties of primary cortical neurons. (**a**) Representative traces of action potentials induced by the injection of 200 pA current steps for 500 ms. Plots of the mean of firing frequency versus injected current per experimental conditions (**b**) and quantification of instantaneous firing frequency (**c**). Mean ± SEM of n = 21 cells for Ctrl, n = 15 cells for GR, n = 25 cells for GO, from 3 independent preparations (*p<0.05, **p<0.01, ***p<0.001 two-way ANOVA and Bonferroni's multiple comparison test). (**d**) Representative plots of the first derivative of the membrane voltage (d*V*/d*t*) versus membrane voltage ($V_m$) (phase-plots) per experimental condition. (**e**) Mean ± SEM of phase-slope measured at voltage more positive of 5 mV/ms. n = 21 cells for Ctrl, n = 15 cells for GR, n = 25 cells for GO, from 3 independent preparations (*p<0.05, ***p<0.001, one-way ANOVA and Bonferroni's multiple comparison test).

# 6. DISCUSSION

The main objective of this study was to perform a detailed analysis of the effects of chronic exposure of G nanosheets on the biology of astroglial cells, which are the principal cellular interface of the neurons in the CNS and whose functionality deeply influences the neuronal network [166]. To date, this is the first study providing a thorough description of the biological interactions between G nanosheets and astroglial cells, and complements the information on the effects caused by the same materials on neuronal circuits *in vitro* [62]. Previous studies showed that the interaction with carbon related materials impact on the morphological and functional phenotype of astrocytes both *in vitro* and *in vivo* [145, 167], stressing the urgency of assessing a detailed toxicity profile for each specific material for future biomedical applications. Here we include a detailed characterization of astrocyte functionality upon GR and GO nanosheet exposure, combining different techniques ranging from cell biology to microscopy, electrophysiology, and live $Ca^{2+}$ imaging.

Although previous experiments showed that the viability of cultured astrocytes was not affected by long-term exposure to GR and GO up to 7 days of treatment, nanosheets caused marked morphological changes that shifted cells from an epithelioid to a differentiated phenotype. Treated astrocytes were characterized by the development of cytoplasmic processes with little ramifications, as previously observed in cells exposed to carbon nanotubes [145]. The observed G-induced morphological alterations resembled those of astrocytes that underwent long-term treatment with a membrane-permeable analogue of cyclic AMP [142, 159, 168, 169]. The relevance of this treatment to the *in vivo* situation is still matter of debate; indeed, cAMP-treated astrocytes have long been

considered as reactive astrocytes [169], whereas recent work suggests that they may reflect a more mature phenotype [142]. It is well known that reactive astrocytes display an increase in GFAP expression both in *vitro* and *in situ* [170, 171], which however was not found under our experimental conditions upon exposure to G materials, (data not shown). This suggests that in our case the observed morphological changes were driven by nanosheet-mediated rearrangement of intracellular actin and tubulin filaments, in agreement with previous finding showing that GO nanosheets can insert into the inter-strand gap of actin tetramers, leading to the disruption of actin filaments [172].

Notably, a larger amount of nanosheets were internalized by astrocytes compared to what we observed in neuronal cells [62]. Astrocytes possess a complex intracellular vesicular network that plays a fundamental role in both physiological and pathophysiological processes of the CNS [173]. The endo-lysosomal pathway resulted the preferential route of G-nanosheets intracellular trafficking. A significant percentage of material was internalized into endosomes within 24 h, ending up in lysosomes after 7 days. Clearly, large flake aggregates (micrometer-size) remained mostly adherent to the cell membrane, while nanosheets were actively taken up and internalized.

Thanks to proteomic and lipidomic analysis, we elucidated the specific effects of GR and GO nanosheets on major intracellular pathways. Interestingly, a close investigation of the proteins related to calcium metabolism, previously reported to be altered in neurons exposed to G materials [62], revealed that calmodulin (Calm1) and many other $Ca^{2+}$-binding proteins were differentially altered after exposure to either GR and GO. Calmodulin is a $Ca^{2+}$-binding protein that mediates the $Ca^{2+}$ regulation of a wide range of physiological processes throughout the eukaryotic kingdom [174]. These data

drew our attention toward further and more detailed investigations. Astrocytes are indeed characterized by a complex modulation of $Ca^{2+}$ events that coordinate their major functions, and in turn influence neuronal activity. They respond both *in vitro* and *in situ* to paracrine molecules released from neurons and other cell types of the CNS with fluctuations of intracellular $Ca^{2+}$ levels, and inducing the release of a variety of diffusible molecules (called gliotransmitters) that can affect neuronal cells and interact in an paracrine fashion with neighboring astrocytes [84, 175]. One of the most important signaling molecules released in the extracellular milieu is ATP, which mediates astrocyte-to-astrocyte $Ca^{2+}$-mediated communication, in particular via the activation of specific ligand gated P2X and G-protein-coupled metabotropic P2Y receptors [176]. Of note, astrocytes respond to ATP with a propagating wave of intracellular $Ca^{2+}$, which underlies the synchronization of $Ca^{2+}$ oscillations [177].

Our results showed that G nanosheets depress spontaneous $Ca^{2+}$ oscillations. This effect was statistically significant only for GO-treated astrocytes and was associated with a significant reduction of ATP-evoked $Ca^{2+}$ transients. Since $Ca^{2+}$ oscillations are linked to $IP_3$-mediated $Ca^{2+}$ release from endoplasmic reticulum [178, 179], this outcome could be attributable to a reduction of $Ca^{2+}$ release from endoplasmic reticulum and/or $Ca^{2+}$ entry, because the influx of $Ca^{2+}$ to refill the stores was also significantly depressed in astroglial cells exposed to GO. The relative contribution of the different pathways in the lower ATP response in GO-treated astrocytes will be clarify in future studies. The P2 purinoceptor-mediated $[Ca^{2+}]_i$ signaling is extremely complex [180]. In particular, $P2X_7$ and $P2Y_1$ receptors are mainly involved in ATP-induced $[Ca2^{+}]_i$ elevations, while additional receptors (i.e., $P2X_2$, $P2X_4$, $P2X_5$, $P2Y_2$, $P2Y_4$, and $P2Y_{14}$) may also contribute

to this phenomenon [181]. The mechanisms whereby GO affects $Ca^{2+}$ signaling can only be speculated upon, and include an effect on membrane cholesterol [182] and cell cytoskeleton [156]. As a matter of fact, cholesterol is an important constituent of lipid rafts, which are membrane platforms involved in the signaling between endoplasmic reticulum and plasma membrane also in astroglial cells [157]. Our results are complementary to those generated in cell transfected with STIM1 and ORAi, which are essential molecular components of store-operated $Ca^{2+}$ entry (SOCE), showing that depletion of membrane cholesterol causes an increase in SOCE signaling [182]. In this case, a dynamic interaction of STIM1 and ORAi, driven by cell cytoskeleton, is required for the correct intracellular signaling mediating $Ca^{2+}$ influx [156]. Thus, we cannot exclude that the GO-mediated reorganization of actin and tubulin filaments plays a role in triggering the effects observed in our experimental system.

An important result of this study is that long-term treatment of cultured astrocytes with GO (but not GR) changed the electrical passive properties of cultured astrocytes, which could be ascribed to the higher expression of a background $K^+$ conductance. The functional and molecular properties of this $K^+$ current were consistent with the activation of Kir 4.1 channels, and corroborated by immunocytochemical and western blot analyses, indicating that Kir 4.1 expression was augmented in GO-treated astrocytes compared to vehicle-treated cells. Kir 4.1 channels preferentially localize at cell processes and perivascular end-feets, and are responsible for maintaining glial negative resting membrane potential and high $K^+$ permeability [76]. In the literature, enhanced expression of Kir 4.1 has been associated with mature astrocytes [76], and with an increased glutamate uptake, which is favored by membrane hyperpolarization [183]. In agreement

with published data, we found an enhanced $Na^+$-dependent glutamate uptake specifically in GO-treated astrocytes, suggesting that the morphological and functional alterations induced by GO exposure are features of a more mature phenotype, resembling the *in vivo* situation. Interestingly, Kir 4.1 dysfunctions have been related to a variety of CNS pathologies, such as Huntington's disease [117], amyotrophic lateral sclerosis [115] and Alzheimer's disease [81]. In addition, astrocytes of mice conditionally ablated of the *KCNJ10* gene, the gene encoding Kir 4.1, show impairments in $K^+$ channel activity and glutamate uptake associated with seizure susceptibility [184]. Thus, the physio-pathological meaning of the effects of GO nanosheets on astrocytes has to be thoroughly evaluated and further investigations *in vivo* are needed to better clarify this point.

Different putative mechanisms have been associated with G cytotoxicity [58]; in our case active internalization through energy dependent pathways seems to be the main cause of the above-described effects. This is suggested by the fact that the effects of GO nanosheets on cell morphology and ion channel expression were abrogated by inhibiting endocytosis upon pretreatment of cultured astrocytes with sodium azide [185], which indicates that internalization of GO nanosheets is necessary to promote its modulatory action.

It is well-known that astrocytes shape neuronal network functions by maintaining the extracellular homeostasis trough $K^+$ and glutamate clearance, and by regulating the properties of synapses thanks to a bidirectional signaling between neurons and astrocytes mediated by intracellular $Ca^{2+}$ waves [166]. Thus, we expected that functional alterations in astrocytes could affect neuronal network properties. To verify this hypothesis, we performed astrocytes neuron co-cultures and monitored electrophysiological properties of

neurons cultured for 10 DIV on G-treated astrocytes. We found an increase in frequency of spontaneous inhibitory postsynaptic current accompanied by an increase of inhibitory synaptic density specific for GO treated samples. These results indicate that astrocytes, after long term GO treatment, selectively promote the formation and functional maturation of inhibitory GABAergic synapses via secreted factors, an effect previously reported to be mediated by neurotrophin signaling [186]. In addition, GO-treated astrocytes significantly enhanced neuronal firing activity evoked by depolarizing current pulses. A possible explanation for this phenomenon is that astrocytes exposed to GO accelerate the functional maturation of neuronal cells, affecting voltage-gated channels expressed not only in the cell soma, but also at the AIS.

This is not the first study addressing the interaction of astroglial cells with nanomaterials. In previous work, mouse cortical astrocytes grown on a single-walled carbon nanotube films displayed an increase in their proliferative rate, a dedifferentiated morphological phenotype and a decrease in GFAP immunoreactivity [145, 187] ,which was interpreted as a nonreactive phenotype. By contrast, the same nanomaterial delivered as colloidal solute promoted the stellation of cultured astrocytes, an increase in GFAP immunoreactivity [188] and an increment in glutamate uptake [167]. Cortical astrocytes plated on synthetic polyamide nanofibers were reported to acquire a stellate morphology caused by activation of Rho GTPases [189] and to promote neurite outgrowth when co-cultured with neurons [190]. This result was associated to the ability of astrocytes grown onto the above-mentioned nanofibers to secrete growth factors into the medium [191]. Whether G nanosheets may also act by stimulating the release of growth factors from

astrocytes to influence the electrical activity of neighboring neurons remains to be addressed. This is another issue to be addressed in our future investigations.

In conclusion, our analysis revealed that, although exposure to G nanosheets does not impact primary astrocyte viability, it has important effects on their functionality and on the physiology of co-cultured neuronal cells. In particular, GO nanosheets, which are the most promising material for biological applications, have a much higher impact on astrocyte cells with respect to GR nanosheets, probably due to their surface charge and higher surface area and reactivity with the biological environment. On one hand, these data raise some concern about the safety of GO nanosheets, suggesting that GR nanosheets are safer in a biological framework. On the other hand, however, our data indicate that the observed GO-induced morphological and functional alterations could be attributed to a more mature astrocyte phenotype rather than to a reactive condition. In addition, considering that potassium and glutamate homeostasis play an important role in regulating neuronal excitability, we can speculate that the increase in potassium and glutamate uptake induced by GO nanosheets could have a neuroprotective role, favorable to prevent the development of seizures and cell death. Furthermore, the possibility of GO nanosheets to be functionalized with polyethylene glycol (PEG), poli(ε-caprolactone) (PCL), pluronic, amine, carboxyl and dextran groups to decrease toxicity and increase biocompatibility plays definitely a major role for further safer applications.

Future studies *in vivo* will address whether GR/GO nanosheets are beneficial or detrimental for the functionality of the CNS and could be used safely for different purposes in clinical neuroscience. A schematic model, summarizing the most relevant finding of this work, is reported in **Figure 12**.

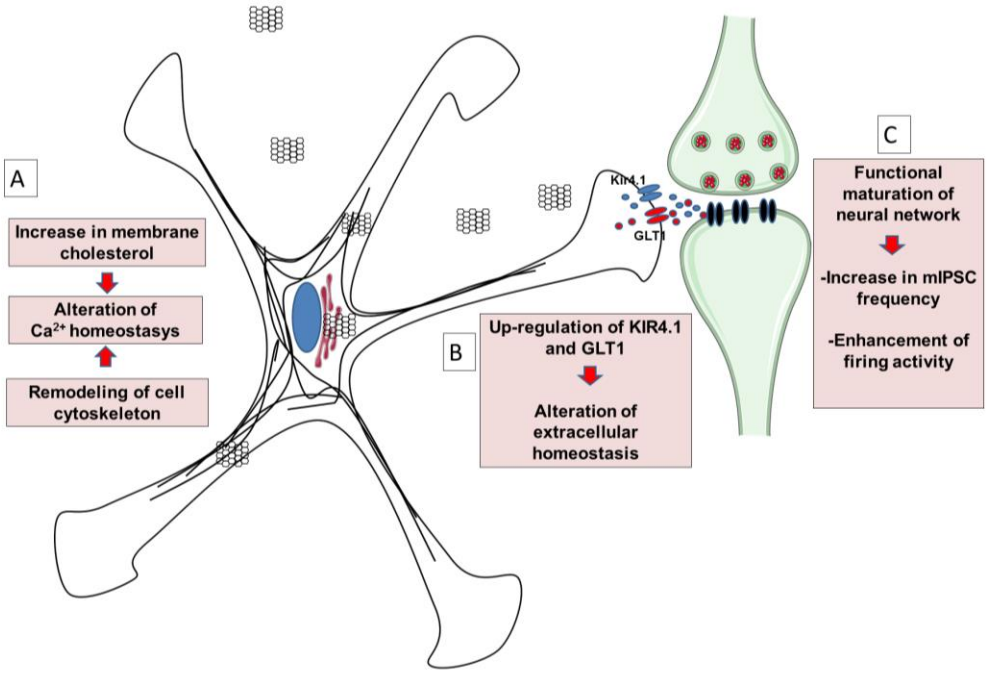


**Figure 12. Schematic representation of the effects of chronic exposure of GO in primary astrocytes.**

**A.** Increase in membrane cholesterol and alteration of cell cytoskeleton impact on $Ca^{2+}$ homeostasis. **B.** Upregulation of Kir4.1 and GLT1 shapes extracellular homeostasis. **C.** Functional alterations in astrocytes accelerate the maturation of neuronal functional properties, including increase in mIPSC frequency and firing activity.

# 7. FUTURE PERSPECTIVES

In future, as follow up of the investigation of G interactions with the CNS, we plan to proceed with *in vivo* brain administration of G (intra-cerebroventricular and intra-parenchimal) to the mouse and study: i) inflammatory response triggered by astrocytes and microglia cells; ii) the behavioral, functional and "omics" profiles *in vivo*; and iii) the physiology of well characterized neuronal circuits (e.g. hippocampus, cerebellum) in acute *ex vivo* brain slices. This will allow researchers to have a complete overview over the bio-interactions of this innovative material with the CNS, ranging from detailed *in vitro* studies, to understand the cellular and molecular mechanisms of interactions, to *in vivo* exposure to investigate a more physiological situation and have a better picture of the physiological effects of graphene. The final aim will be to understand the biological behavior of G, in order to engineer the material and increase its biocompatibility to address biomedical applications.

# 8. ACKNOWLEDGEMENTS

I thank Professor Fabio Benfenati for his mentoring, for solving my PhD related problems and to get me involved in this project.

I want to thank Dr. Fabrizia Cesca for useful discussions, experimental advices and for contributing to the production of this thesis.

Thanks also to Professor Stefano Ferroni for experimental advices and for continuing to follow me after so many years.

A special thanks to Dr. Mattia Bramini, for having introduced me to the world of nanomaterials, for contributing to the production of this thesis and for his scientific and friendly advice.

Finally, I want to thank my colleagues, you have been a nice environment of friendship and of intellectual stimulation.

# 9. BIBLIOGRAPHY


1. Novoselov, K.S., et al., *Electric field effect in atomically thin carbon films.* Science, 2004. **306**(5696): p. 666-9.
2. Novoselov, K.S., et al., *A roadmap for graphene.* Nature, 2012. **490**(7419): p. 192-200.
3. Casaluci, S., et al., *Graphene-based large area dye-sensitized solar cell modules.* Nanoscale, 2016. **8**(9): p. 5368-78.
4. Kostarelos, K., et al., *Graphene in the Design and Engineering of Next-Generation Neural Interfaces.* Adv Mater, 2017.
5. Wick, P., et al., *Classification framework for graphene-based materials.* Angew Chem Int Ed Engl, 2014. **53**(30): p. 7714-8.
6. S.F Kiew et al., *Assessing biocompatibility of graphene-based nanocarriers: A review.* journal of controlled release, 2016. **226**: p. 217-228.
7. Hernandez, Y., et al., *High-yield production of graphene by liquid-phase exfoliation of graphite.* Nat Nanotechnol, 2008. **3**(9): p. 563-8.
8. Li, X., et al., *Large-area synthesis of high-quality and uniform graphene films on copper foils.* Science, 2009. **324**(5932): p. 1312-4.
9. Aristov, V.Y., et al., *Graphene synthesis on cubic SiC/Si wafers. perspectives for mass production of graphene-based electronic devices.* Nano Lett, 2010. **10**(3): p. 992-5.
10. Torrisi, F., et al., *Inkjet-printed graphene electronics.* ACS Nano, 2012. **6**(4): p. 2992-3006.
11. Shin, S.R., et al., *Graphene-based materials for tissue engineering.* Adv Drug Deliv Rev, 2016. **105**(Pt B): p. 255-274.
12. Bao, Q. and K.P. Loh, *Graphene photonics, plasmonics, and broadband optoelectronic devices.* ACS Nano, 2012. **6**(5): p. 3677-94.
13. Lin, Y.M., et al., *100-GHz transistors from wafer-scale epitaxial graphene.* Science, 2010. **327**(5966): p. 662.
14. Singh, Z., *Applications and toxicity of graphene family nanomaterials and their composites.* Nanotechnol Sci Appl, 2016. **9**: p. 15-28.
15. Hasan, S.A., et al., *Transferable graphene oxide films with tunable microstructures.* ACS Nano, 2010. **4**(12): p. 7367-72.
16. Georgakilas, V., et al., *Noncovalent Functionalization of Graphene and Graphene Oxide for Energy Materials, Biosensing, Catalytic, and Biomedical Applications.* Chem Rev, 2016. **116**(9): p. 5464-519.
17. Chowdhury, I., et al., *Colloidal properties and stability of graphene oxide nanomaterials in the aquatic environment.* Environ Sci Technol, 2013. **47**(12): p. 6288-96.
18. Chen, D., H. Feng, and J. Li, *Graphene oxide: preparation, functionalization, and electrochemical applications.* Chem Rev, 2012. **112**(11): p. 6027-53.
19. Wojtoniszak, M., et al., *Synthesis, dispersion, and cytocompatibility of graphene oxide and reduced graphene oxide.* Colloids Surf B Biointerfaces, 2012. **89**: p. 79-85.
20. Dell'Orco, D., et al., *Modeling the time evolution of the nanoparticle-protein corona in a body fluid.* PLoS One, 2010. **5**(6): p. e10949.
21. Zhou, H., et al., *The interactions between pristine graphene and macrophages and the production of cytokines/chemokines via TLR- and NF-kappaB-related signaling pathways.* Biomaterials, 2012. **33**(29): p. 6933-42.
22. Liao, K.H., et al., *Cytotoxicity of graphene oxide and graphene in human erythrocytes and skin fibroblasts.* ACS Appl Mater Interfaces, 2011. **3**(7): p. 2607-15.

23. McCallion, C., et al., *Graphene in therapeutics delivery: Problems, solutions and future opportunities.* Eur J Pharm Biopharm, 2016. **104**: p. 235-50.
24. Upadhyay, R.K., *Drug delivery systems, CNS protection, and the blood brain barrier.* Biomed Res Int, 2014. **2014**: p. 869269.
25. Mendonca, M.C., et al., *Reduced graphene oxide induces transient blood-brain barrier opening: an in vivo study.* J Nanobiotechnology, 2015. **13**: p. 78.
26. Mendonca, M.C., et al., *PEGylation of Reduced Graphene Oxide Induces Toxicity in Cells of the Blood-Brain Barrier: An in Vitro and in Vivo Study.* Mol Pharm, 2016. **13**(11): p. 3913-3924.
27. Xiao, S., et al., *Graphene quantum dots conjugated neuroprotective peptide improve learning and memory capability.* Biomaterials, 2016. **106**: p. 98-110.
28. Song, M.M., et al., *Lactoferrin modified graphene oxide iron oxide nanocomposite for glioma-targeted drug delivery.* Mater Sci Eng C Mater Biol Appl, 2017. **77**: p. 904-911.
29. Yan, L., et al., *Chemistry and physics of a single atomic layer: strategies and challenges for functionalization of graphene and graphene-based materials.* Chem Soc Rev, 2012. **41**(1): p. 97-114.
30. Paul, A., et al., *Injectable graphene oxide/hydrogel-based angiogenic gene delivery system for vasculogenesis and cardiac repair.* ACS Nano, 2014. **8**(8): p. 8050-62.
31. Liu, X., et al., *Polyamidoamine dendrimer and oleic acid-functionalized graphene as biocompatible and efficient gene delivery vectors.* ACS Appl Mater Interfaces, 2014. **6**(11): p. 8173-83.
32. Yin, D., et al., *Functional graphene oxide as a plasmid-based Stat3 siRNA carrier inhibits mouse malignant melanoma growth in vivo.* Nanotechnology, 2013. **24**(10): p. 105102.
33. Imani, R., S.H. Emami, and S. Faghihi, *Synthesis and characterization of an octaarginine functionalized graphene oxide nano-carrier for gene delivery applications.* Phys Chem Chem Phys, 2015. **17**(9): p. 6328-39.
34. Xu, C., et al., *Encapsulating gold nanoparticles or nanorods in graphene oxide shells as a novel gene vector.* ACS Appl Mater Interfaces, 2013. **5**(7): p. 2715-24.
35. Yang, X., N. Zhao, and F.J. Xu, *Biocleavable graphene oxide based-nanohybrids synthesized via ATRP for gene/drug delivery.* Nanoscale, 2014. **6**(11): p. 6141-50.
36. Choi, H.Y., et al., *Efficient mRNA delivery with graphene oxide-polyethylenimine for generation of footprint-free human induced pluripotent stem cells.* J Control Release, 2016. **235**: p. 222-235.
37. Perlmutter, J.S. and J.W. Mink, *Deep brain stimulation.* Annu Rev Neurosci, 2006. **29**: p. 229-57.
38. Picaud, S. and J.A. Sahel, *Retinal prostheses: clinical results and future challenges.* C R Biol, 2014. **337**(3): p. 214-22.
39. Spelman, F.A., *Cochlear electrode arrays: past, present and future.* Audiol Neurootol, 2006. **11**(2): p. 77-85.
40. Hatsopoulos, N.G. and J.P. Donoghue, *The science of neural interface systems.* Annu Rev Neurosci, 2009. **32**: p. 249-66.
41. Chang, E.F., *Towards large-scale, human-based, mesoscopic neurotechnologies.* Neuron, 2015. **86**(1): p. 68-78.
42. Kuzum, D., et al., *Transparent and flexible low noise graphene electrodes for simultaneous electrophysiology and neuroimaging.* Nat Commun, 2014. **5**: p. 5259.
43. Veliev, F., et al., *Recording Spikes Activity in Cultured Hippocampal Neurons Using Flexible or Transparent Graphene Transistors.* Front Neurosci, 2017. **11**: p. 466.

44. Blaschke, B.M., *Mapping brain activity with flexible graphene micro-transistors.* 2D Materials, 2017. **4**(025040).
45. Yoo, J.M., J.H. Kang, and B.H. Hong, *Graphene-based nanomaterials for versatile imaging studies.* Chem Soc Rev, 2015. **44**(14): p. 4835-52.
46. Sun, Z., et al., *VEGF-loaded graphene oxide as theranostics for multi-modality imaging-monitored targeting therapeutic angiogenesis of ischemic muscle.* Nanoscale, 2013. **5**(15): p. 6857-66.
47. Salihoglu, O., et al., *Graphene as a Reversible and Spectrally Selective Fluorescence Quencher.* Sci Rep, 2016. **6**: p. 33911.
48. Chang, H., et al., *Graphene fluorescence resonance energy transfer aptasensor for the thrombin detection.* Anal Chem, 2010. **82**(6): p. 2341-6.
49. Chen, M.L., et al., *Quantum-dot-conjugated graphene as a probe for simultaneous cancer-targeted fluorescent imaging, tracking, and monitoring drug delivery.* Bioconjug Chem, 2013. **24**(3): p. 387-97.
50. Zheng, P. and N. Wu, *Fluorescence and Sensing Applications of Graphene Oxide and Graphene Quantum Dots: A Review.* Chem Asian J, 2017. **12**(18): p. 2343-2353.
51. Dong, H., et al., *Multifunctional Poly(L-lactide)-Polyethylene Glycol-Grafted Graphene Quantum Dots for Intracellular MicroRNA Imaging and Combined Specific-Gene-Targeting Agents Delivery for Improved Therapeutics.* ACS Appl Mater Interfaces, 2015. **7**(20): p. 11015-23.
52. Lu, C.H., et al., *A graphene platform for sensing biomolecules.* Angew Chem Int Ed Engl, 2009. **48**(26): p. 4785-7.
53. Zhang, H., et al., *A turn-on fluorescence-sensing technique for glucose determination based on graphene oxide-DNA interaction.* Anal Bioanal Chem, 2014. **406**(27): p. 6925-32.
54. Song, Y., et al., *Graphene oxide: intrinsic peroxidase catalytic activity and its application to glucose detection.* Adv Mater, 2010. **22**(19): p. 2206-10.
55. Kuila, T., et al., *Recent advances in graphene-based biosensors.* Biosens Bioelectron, 2011. **26**(12): p. 4637-48.
56. Hess, L.H., et al., *Graphene transistors with multifunctional polymer brushes for biosensing applications.* ACS Appl Mater Interfaces, 2014. **6**(12): p. 9705-10.
57. Mao, H., et al., *Poly(ionic liquids) functionalized polypyrrole/graphene oxide nanosheets for electrochemical sensor to detect dopamine in the presence of ascorbic acid.* Biosens Bioelectron, 2015. **70**: p. 289-98.
58. Ou, L., et al., *Toxicity of graphene-family nanoparticles: a general review of the origins and mechanisms.* Part Fibre Toxicol, 2016. **13**(1): p. 57.
59. Zhang, S., et al., *Size-Dependent Endocytosis of Nanoparticles.* Adv Mater, 2009. **21**: p. 419-424.
60. Linares, J., et al., *Endocytic mechanisms of graphene oxide nanosheets in osteoblasts, hepatocytes and macrophages.* ACS Appl Mater Interfaces, 2014. **6**(16): p. 13697-706.
61. Leon, V., et al., *Exfoliation of graphite with triazine derivatives under ball-milling conditions: preparation of few-layer graphene via selective noncovalent interactions.* ACS Nano, 2014. **8**(1): p. 563-71.
62. Bramini, M., et al., *Graphene Oxide Nanosheets Disrupt Lipid Composition, Ca(2+) Homeostasis, and Synaptic Transmission in Primary Cortical Neurons.* ACS Nano, 2016. **10**(7): p. 7154-71.
63. Clogston, J.D. and A.K. Patri, *Zeta potential measurement.* Methods Mol Biol, 2011. **697**: p. 63-70.

64. Ferrari, A.C. and D.M. Basko, *Raman spectroscopy as a versatile tool for studying the properties of graphene.* Nat Nanotechnol, 2013. **8**(4): p. 235-46.
65. Wall, M., *The Raman Spectroscopy of Graphene and the Determination of Layer Thickness.* Thermo Scientific Application Note AN52252 2011.
66. Rauti, R., et al., *Graphene Oxide Nanosheets Reshape Synaptic Function in Cultured Brain Networks.* ACS Nano, 2016. **10**(4): p. 4459-71.
67. Fabbro, A., et al., *Graphene-Based Interfaces Do Not Alter Target Nerve Cells.* ACS Nano, 2016. **10**(1): p. 615-23.
68. Park, S.Y., et al., *Enhanced differentiation of human neural stem cells into neurons on graphene.* Adv Mater, 2011. **23**(36): p. H263-7.
69. Wang, Y., et al., *Fluorinated graphene for promoting neuro-induction of stem cells.* Adv Mater, 2012. **24**(31): p. 4285-90.
70. Li, N., et al., *Three-dimensional graphene foam as a biocompatible and conductive scaffold for neural stem cells.* Sci Rep, 2013. **3**: p. 1604.
71. Ulloa Severino, F.P., et al., *The role of dimensionality in neuronal network dynamics.* Sci Rep, 2016. **6**: p. 29640.
72. Martin, C., et al., *Graphene Improves the Biocompatibility of Polyacrylamide Hydrogels: 3D Polymeric Scaffolds for Neuronal Growth.* Sci Rep, 2017. **7**(1): p. 10942.
73. Peters, A., S.L. Palay, and H.d. Webster, *The fine structure of the nervous system : neurons and their supporting cells*. 3rd ed1991, New York: Oxford University Press. xviii, 494 p.
74. Lascola, C.D. and R.P. Kraig, *Whole-cell chloride currents in rat astrocytes accompany changes in cell morphology.* J Neurosci, 1996. **16**(8): p. 2532-45.
75. Bevan, S. and M. Raff, *Voltage-dependent potassium currents in cultured astrocytes.* Nature, 1985. **315**(6016): p. 229-32.
76. Olsen, M.L. and H. Sontheimer, *Functional implications for Kir4.1 channels in glial biology: from K+ buffering to cell differentiation.* J Neurochem, 2008. **107**(3): p. 589-601.
77. Schousboe, A. and H.S. Waagepetersen, *Role of astrocytes in glutamate homeostasis: implications for excitotoxicity.* Neurotox Res, 2005. **8**(3-4): p. 221-5.
78. MacVicar, B.A. and E.A. Newman, *Astrocyte regulation of blood flow in the brain.* Cold Spring Harb Perspect Biol, 2015. **7**(5).
79. Benfenati, V. and S. Ferroni, *Water transport between CNS compartments: functional and molecular interactions between aquaporins and ion channels.* Neuroscience, 2010. **168**(4): p. 926-40.
80. Meier, S.D., K.W. Kafitz, and C.R. Rose, *Developmental profile and mechanisms of GABA-induced calcium signaling in hippocampal astrocytes.* Glia, 2008. **56**(10): p. 1127-37.
81. Cornell-Bell, A.H., et al., *Glutamate induces calcium waves in cultured astrocytes: long-range glial signaling.* Science, 1990. **247**(4941): p. 470-3.
82. Salter, M.W. and J.L. Hicks, *ATP causes release of intracellular Ca2+ via the phospholipase C beta/IP3 pathway in astrocytes from the dorsal spinal cord.* J Neurosci, 1995. **15**(4): p. 2961-71.
83. James, G. and A.M. Butt, *P2Y and P2X purinoceptor mediated Ca2+ signalling in glial cell pathology in the central nervous system.* Eur J Pharmacol, 2002. **447**(2-3): p. 247-60.
84. Bazargani, N. and D. Attwell, *Astrocyte calcium signaling: the third wave.* Nat Neurosci, 2016. **19**(2): p. 182-9.
85. Araque, A., et al., *Calcium elevation in astrocytes causes an NMDA receptor-dependent increase in the frequency of miniature synaptic currents in cultured hippocampal neurons.* J Neurosci, 1998. **18**(17): p. 6822-9.

86. Perea, G. and A. Araque, *Astrocytes potentiate transmitter release at single hippocampal synapses.* Science, 2007. **317**(5841): p. 1083-6.
87. Carmignoto, G. and P.G. Haydon, *Astrocyte calcium signaling and epilepsy.* Glia, 2012. **60**(8): p. 1227-33.
88. Rossi, D., et al., *Defective tumor necrosis factor-alpha-dependent control of astrocyte glutamate release in a transgenic mouse model of Alzheimer disease.* J Biol Chem, 2005. **280**(51): p. 42088-96.
89. Bezzi, P., et al., *CXCR4-activated astrocyte glutamate release via TNFalpha: amplification by microglia triggers neurotoxicity.* Nat Neurosci, 2001. **4**(7): p. 702-10.
90. Pyka, M., et al., *Chondroitin sulfate proteoglycans regulate astrocyte-dependent synaptogenesis and modulate synaptic activity in primary embryonic hippocampal neurons.* Eur J Neurosci, 2011. **33**(12): p. 2187-202.
91. Kucukdereli, H., et al., *Control of excitatory CNS synaptogenesis by astrocyte-secreted proteins Hevin and SPARC.* Proc Natl Acad Sci U S A, 2011. **108**(32): p. E440-9.
92. Allen, N.J., et al., *Astrocyte glypicans 4 and 6 promote formation of excitatory synapses via GluA1 AMPA receptors.* Nature, 2012. **486**(7403): p. 410-4.
93. Albrecht, D., et al., *SPARC prevents maturation of cholinergic presynaptic terminals.* Mol Cell Neurosci, 2012. **49**(3): p. 364-74.
94. Stevens, B., et al., *The classical complement cascade mediates CNS synapse elimination.* Cell, 2007. **131**(6): p. 1164-78.
95. Schafer, D.P., et al., *Microglia sculpt postnatal neural circuits in an activity and complement-dependent manner.* Neuron, 2012. **74**(4): p. 691-705.
96. Bialas, A.R. and B. Stevens, *TGF-beta signaling regulates neuronal C1q expression and developmental synaptic refinement.* Nat Neurosci, 2013. **16**(12): p. 1773-82.
97. Loov, C., et al., *Engulfing astrocytes protect neurons from contact-induced apoptosis following injury.* PLoS One, 2012. **7**(3): p. e33090.
98. Fawcett, J.W. and R.A. Asher, *The glial scar and central nervous system repair.* Brain Res Bull, 1999. **49**(6): p. 377-91.
99. Cahoy, J.D., et al., *A transcriptome database for astrocytes, neurons, and oligodendrocytes: a new resource for understanding brain development and function.* J Neurosci, 2008. **28**(1): p. 264-78.
100. Liddelow, S.A., et al., *Neurotoxic reactive astrocytes are induced by activated microglia.* Nature, 2017. **541**(7638): p. 481-487.
101. Takumi, T., et al., *A novel ATP-dependent inward rectifier potassium channel expressed predominantly in glial cells.* J Biol Chem, 1995. **270**(27): p. 16339-46.
102. Hibino, H., et al., *Differential assembly of inwardly rectifying K+ channel subunits, Kir4.1 and Kir5.1, in brain astrocytes.* J Biol Chem, 2004. **279**(42): p. 44065-73.
103. Poopalasundaram, S., et al., *Glial heterogeneity in expression of the inwardly rectifying K(+) channel, Kir4.1, in adult rat CNS.* Glia, 2000. **30**(4): p. 362-72.
104. Olsen, M.L., S.L. Campbell, and H. Sontheimer, *Differential distribution of Kir4.1 in spinal cord astrocytes suggests regional differences in K+ homeostasis.* J Neurophysiol, 2007. **98**(2): p. 786-93.
105. Tang, X., K. Taniguchi, and P. Kofuji, *Heterogeneity of Kir4.1 channel expression in glia revealed by mouse transgenesis.* Glia, 2009. **57**(16): p. 1706-15.
106. Kalsi, A.S., et al., *Kir4.1 expression by astrocytes and oligodendrocytes in CNS white matter: a developmental study in the rat optic nerve.* J Anat, 2004. **204**(6): p. 475-85.

107. Moroni, R.F., et al., *Developmental expression of Kir4.1 in astrocytes and oligodendrocytes of rat somatosensory cortex and hippocampus.* Int J Dev Neurosci, 2015. **47**(Pt B): p. 198-205.
108. Kofuji, P. and E.A. Newman, *Potassium buffering in the central nervous system.* Neuroscience, 2004. **129**(4): p. 1045-56.
109. Djukic, B., et al., *Conditional knock-out of Kir4.1 leads to glial membrane depolarization, inhibition of potassium and glutamate uptake, and enhanced short-term synaptic potentiation.* J Neurosci, 2007. **27**(42): p. 11354-65.
110. Chever, O., et al., *Implication of Kir4.1 channel in excess potassium clearance: an in vivo study on anesthetized glial-conditional Kir4.1 knock-out mice.* J Neurosci, 2010. **30**(47): p. 15769-77.
111. Schroder, W., et al., *Functional and molecular properties of human astrocytes in acute hippocampal slices obtained from patients with temporal lobe epilepsy.* Epilepsia, 2000. **41 Suppl 6**: p. S181-4.
112. Inyushin, M., et al., *Potassium channel activity and glutamate uptake are impaired in astrocytes of seizure-susceptible DBA/2 mice.* Epilepsia, 2010. **51**(9): p. 1707-13.
113. Pivonkova, H., et al., *Impact of global cerebral ischemia on K+ channel expression and membrane properties of glial cells in the rat hippocampus.* Neurochem Int, 2010. **57**(7): p. 783-94.
114. D'Ambrosio, R., et al., *Impaired K(+) homeostasis and altered electrophysiological properties of post-traumatic hippocampal glia.* J Neurosci, 1999. **19**(18): p. 8152-62.
115. Bataveljic, D., et al., *Changes in the astrocytic aquaporin-4 and inwardly rectifying potassium channel expression in the brain of the amyotrophic lateral sclerosis SOD1(G93A) rat model.* Glia, 2012. **60**(12): p. 1991-2003.
116. Nwaobi, S.E., et al., *The role of glial-specific Kir4.1 in normal and pathological states of the CNS.* Acta Neuropathol, 2016. **132**(1): p. 1-21.
117. Tong, X., et al., *Astrocyte Kir4.1 ion channel deficits contribute to neuronal dysfunction in Huntington's disease model mice.* Nat Neurosci, 2014. **17**(5): p. 694-703.
118. Gegelashvili, G. and A. Schousboe, *Cellular distribution and kinetic properties of high-affinity glutamate transporters.* Brain Res Bull, 1998. **45**(3): p. 233-8.
119. Danbolt, N.C., *Glutamate uptake.* Prog Neurobiol, 2001. **65**(1): p. 1-105.
120. Perego, C., et al., *The GLT-1 and GLAST glutamate transporters are expressed on morphologically distinct astrocytes and regulated by neuronal activity in primary hippocampal cocultures.* J Neurochem, 2000. **75**(3): p. 1076-84.
121. Stanimirovic, D.B., et al., *Developmental regulation of glutamate transporters and glutamine synthetase activity in astrocyte cultures differentiated in vitro.* Int J Dev Neurosci, 1999. **17**(3): p. 173-84.
122. Rothstein, J.D., et al., *Localization of neuronal and glial glutamate transporters.* Neuron, 1994. **13**(3): p. 713-25.
123. Benveniste, H., et al., *Elevation of the extracellular concentrations of glutamate and aspartate in rat hippocampus during transient cerebral ischemia monitored by intracerebral microdialysis.* J Neurochem, 1984. **43**(5): p. 1369-74.
124. Erecinska, M. and I.A. Silver, *Metabolism and role of glutamate in mammalian brain.* Prog Neurobiol, 1990. **35**(4): p. 245-96.
125. Torp, R., et al., *Reduced postischemic expression of a glial glutamate transporter, GLT1, in the rat hippocampus.* Exp Brain Res, 1995. **103**(1): p. 51-8.
126. Tanaka, K., et al., *Epilepsy and exacerbation of brain injury in mice lacking the glutamate transporter GLT-1.* Science, 1997. **276**(5319): p. 1699-702.

127. Samuelsson, C., et al., *Decreased cortical levels of astrocytic glutamate transport protein GLT-1 in a rat model of posttraumatic epilepsy.* Neurosci Lett, 2000. **289**(3): p. 185-8.
128. Ye, Z.C., J.D. Rothstein, and H. Sontheimer, *Compromised glutamate transport in human glioma cells: reduction-mislocalization of sodium-dependent glutamate transporters and enhanced activity of cystine-glutamate exchange.* J Neurosci, 1999. **19**(24): p. 10767-77.
129. Trotti, D., et al., *SOD1 mutants linked to amyotrophic lateral sclerosis selectively inactivate a glial glutamate transporter.* Nat Neurosci, 1999. **2**(5): p. 427-33.
130. Rothstein, J.D., et al., *Selective loss of glial glutamate transporter GLT-1 in amyotrophic lateral sclerosis.* Ann Neurol, 1995. **38**(1): p. 73-84.
131. Mathern, G.W., et al., *Hippocampal GABA and glutamate transporter immunoreactivity in patients with temporal lobe epilepsy.* Neurology, 1999. **52**(3): p. 453-72.
132. Li, S., et al., *Glutamate transporter alterations in Alzheimer disease are possibly associated with abnormal APP expression.* J Neuropathol Exp Neurol, 1997. **56**(8): p. 901-11.
133. Jiang, R., et al., *Dysfunctional Calcium and Glutamate Signaling in Striatal Astrocytes from Huntington's Disease Model Mice.* J Neurosci, 2016. **36**(12): p. 3453-70.
134. Kucheryavykh, Y.V., et al., *Downregulation of Kir4.1 inward rectifying potassium channel subunits by RNAi impairs potassium transfer and glutamate uptake by cultured cortical astrocytes.* Glia, 2007. **55**(3): p. 274-81.
135. Verre A. F. et al., *Improving the glial differentiation of human Schwann-like adipose-derived stem cells with graphene oxide substrates.* 2017.
136. Zhou, K., et al., *Graphene Functionalized Scaffolds Reduce the Inflammatory Response and Supports Endogenous Neuroblast Migration when Implanted in the Adult Brain.* PLoS One, 2016. **11**(3): p. e0151589.
137. Leon, V., et al., *Production and stability of mechanochemically exfoliated graphene in water and culture media.* Nanoscale, 2016. **8**(30): p. 14548-55.
138. Takuma, K., A. Baba, and T. Matsuda, *Astrocyte apoptosis: implications for neuroprotection.* Prog Neurobiol, 2004. **72**(2): p. 111-27.
139. Rauniyar, N., et al., *Comparison of protein expression ratios observed by sixplex and duplex TMT labeling method.* J Proteome Res, 2013. **12**(2): p. 1031-9.
140. Thomas, P.D., et al., *PANTHER: a library of protein families and subfamilies indexed by function.* Genome Res, 2003. **13**(9): p. 2129-41.
141. Snel, B., et al., *STRING: a web-server to retrieve and display the repeatedly occurring neighbourhood of a gene.* Nucleic Acids Res, 2000. **28**(18): p. 3442-4.
142. Paco, S., et al., *Cyclic AMP signaling restricts activation and promotes maturation and antioxidant defenses in astrocytes.* BMC Genomics, 2016. **17**: p. 304.
143. Sun, D. and T.C. Jakobs, *Structural remodeling of astrocytes in the injured CNS.* Neuroscientist, 2012. **18**(6): p. 567-88.
144. Safavi-Abbasi, S., J.R. Wolff, and M. Missler, *Rapid morphological changes in astrocytes are accompanied by redistribution but not by quantitative changes of cytoskeletal proteins.* Glia, 2001. **36**(1): p. 102-15.
145. Gottipati, M.K., et al., *Changes in the morphology and proliferation of astrocytes induced by two modalities of chemically functionalized single-walled carbon nanotubes are differentially mediated by glial fibrillary acidic protein.* Nano Lett, 2014. **14**(7): p. 3720-7.
146. Patskovsky, S., et al., *Wide-field hyperspectral 3D imaging of functionalized gold nanoparticles targeting cancer cells by reflected light microscopy.* J Biophotonics, 2015. **8**(5): p. 401-7.

147. Shapero, K., et al., *Time and space resolved uptake study of silica nanoparticles by human cells.* Mol Biosyst, 2011. **7**(2): p. 371-8.
148. Mu, Q., et al., *Size-dependent cell uptake of protein-coated graphene oxide nanosheets.* ACS Appl Mater Interfaces, 2012. **4**(4): p. 2259-66.
149. Sandin, P., et al., *High-speed imaging of Rab family small GTPases reveals rare events in nanoparticle trafficking in living cells.* ACS Nano, 2012. **6**(2): p. 1513-21.
150. Bramini, M., et al., *Imaging approach to mechanistic study of nanoparticle interactions with the blood-brain barrier.* ACS Nano, 2014. **8**(5): p. 4304-12.
151. Ye, D., et al., *Nanoparticle accumulation and transcytosis in brain endothelial cell layers.* Nanoscale, 2013. **5**(22): p. 11153-65.
152. Lammel, T., et al., *Internalization and cytotoxicity of graphene oxide and carboxyl graphene nanoplatelets in the human hepatocellular carcinoma cell line Hep G2.* Part Fibre Toxicol, 2013. **10**: p. 27.
153. Li, Y., et al., *Graphene microsheets enter cells through spontaneous membrane penetration at edge asperities and corner sites.* Proc Natl Acad Sci U S A, 2013. **110**(30): p. 12295-300.
154. Michaelis, M., et al., *STIM1, STIM2, and Orai1 regulate store-operated calcium entry and purinergic activation of microglia.* Glia, 2015. **63**(4): p. 652-63.
155. Razani-Boroujerdi, S., L.D. Partridge, and M.L. Sopori, *Intracellular calcium signaling induced by thapsigargin in excitable and inexcitable cells.* Cell Calcium, 1994. **16**(6): p. 467-74.
156. Barr, V.A., et al., *Dynamic movement of the calcium sensor STIM1 and the calcium channel Orai1 in activated T-cells: puncta and distal caps.* Mol Biol Cell, 2008. **19**(7): p. 2802-17.
157. Weerth, S.H., L.A. Holtzclaw, and J.T. Russell, *Signaling proteins in raft-like microdomains are essential for Ca2+ wave propagation in glial cells.* Cell Calcium, 2007. **41**(2): p. 155-67.
158. MacFarlane, S.N. and H. Sontheimer, *Electrophysiological changes that accompany reactive gliosis in vitro.* J Neurosci, 1997. **17**(19): p. 7316-29.
159. Ferroni, S., et al., *Two distinct inwardly rectifying conductances are expressed in long term dibutyryl-cyclic-AMP treated rat cultured cortical astrocytes.* FEBS Lett, 1995. **367**(3): p. 319-25.
160. Ransom, C.B. and H. Sontheimer, *Biophysical and pharmacological characterization of inwardly rectifying K+ currents in rat spinal cord astrocytes.* J Neurophysiol, 1995. **73**(1): p. 333-46.
161. Shimamoto, K., et al., *DL-threo-beta-benzyloxyaspartate, a potent blocker of excitatory amino acid transporters.* Mol Pharmacol, 1998. **53**(2): p. 195-201.
162. Schmid, S.L. and L.L. Carter, *ATP is required for receptor-mediated endocytosis in intact cells.* J Cell Biol, 1990. **111**(6 Pt 1): p. 2307-18.
163. David, Y., et al., *Astrocytic dysfunction in epileptogenesis: consequence of altered potassium and glutamate homeostasis?* J Neurosci, 2009. **29**(34): p. 10588-99.
164. Bellot-Saez, A., et al., *Astrocytic modulation of neuronal excitability through K+ spatial buffering.* Neurosci Biobehav Rev, 2017. **77**: p. 87-97.
165. Naundorf, B., F. Wolf, and M. Volgushev, *Unique features of action potential initiation in cortical neurons.* Nature, 2006. **440**(7087): p. 1060-3.
166. Araque, A. and M. Navarrete, *Glial cells in neuronal network function.* Philos Trans R Soc Lond B Biol Sci, 2010. **365**(1551): p. 2375-81.

167. Gottipati, M.K., et al., *Chemically functionalized single-walled carbon nanotubes enhance the glutamate uptake characteristics of mouse cortical astrocytes.* Amino Acids, 2015. **47**(7): p. 1379-88.
168. Shapiro, D.L., *Morphological and biochemical alterations in foetal rat brain cells cultured in the presence of monobutyryl cyclic AMP.* Nature, 1973. **241**(5386): p. 203-4.
169. Wandosell, F., P. Bovolenta, and M. Nieto-Sampedro, *Differences between reactive astrocytes and cultured astrocytes treated with di-butyryl-cyclic AMP.* J Neuropathol Exp Neurol, 1993. **52**(3): p. 205-15.
170. Hol, E.M. and M. Pekny, *Glial fibrillary acidic protein (GFAP) and the astrocyte intermediate filament system in diseases of the central nervous system.* Curr Opin Cell Biol, 2015. **32**: p. 121-30.
171. Brahmachari, S., Y.K. Fung, and K. Pahan, *Induction of glial fibrillary acidic protein expression in astrocytes by nitric oxide.* J Neurosci, 2006. **26**(18): p. 4930-9.
172. Tian, X., et al., *Graphene Oxide Nanosheets Retard Cellular Migration via Disruption of Actin Cytoskeleton.* Small, 2017. **13**(3).
173. Zorec, R., V. Parpura, and A. Verkhratsky, *Astroglial vesicular network: evolutionary trends, physiology and pathophysiology.* Acta Physiol (Oxf), 2017.
174. Olwin, B.B. and D.R. Storm, *Calcium binding to complexes of calmodulin and calmodulin binding proteins.* Biochemistry, 1985. **24**(27): p. 8081-6.
175. Scemes, E. and C. Giaume, *Astrocyte calcium waves: what they are and what they do.* Glia, 2006. **54**(7): p. 716-25.
176. Stout, C.E., et al., *Intercellular calcium signaling in astrocytes via ATP release through connexin hemichannels.* J Biol Chem, 2002. **277**(12): p. 10482-8.
177. Koizumi, S., *Synchronization of Ca2+ oscillations: involvement of ATP release in astrocytes.* FEBS J, 2010. **277**(2): p. 286-92.
178. Golovina, V.A., *Visualization of localized store-operated calcium entry in mouse astrocytes. Close proximity to the endoplasmic reticulum.* J Physiol, 2005. **564**(Pt 3): p. 737-49.
179. Smyth, J.T., et al., *Activation and regulation of store-operated calcium entry.* J Cell Mol Med, 2010. **14**(10): p. 2337-49.
180. Dubyak, G.R. and C. el-Moatassim, *Signal transduction via P2-purinergic receptors for extracellular ATP and other nucleotides.* Am J Physiol, 1993. **265**(3 Pt 1): p. C577-606.
181. Abbracchio, M.P. and S. Ceruti, *Roles of P2 receptors in glial cells: focus on astrocytes.* Purinergic Signal, 2006. **2**(4): p. 595-604.
182. Pacheco, J., et al., *A cholesterol-binding domain in STIM1 modulates STIM1-Orai1 physical and functional interactions.* Sci Rep, 2016. **6**: p. 29634.
183. Anderson, C.M. and R.A. Swanson, *Astrocyte glutamate transport: review of properties, regulation, and physiological functions.* Glia, 2000. **32**(1): p. 1-14.
184. Reichold, M., et al., *KCNJ10 gene mutations causing EAST syndrome (epilepsy, ataxia, sensorineural deafness, and tubulopathy) disrupt channel function.* Proc Natl Acad Sci U S A, 2010. **107**(32): p. 14490-5.
185. Scarmato, P., et al., *Inhibitory effect of sodium arsenite and azide on asialoglycoprotein receptor mediated endocytosis in suspended rat hepatocytes.* Biol Cell, 1986. **56**(3): p. 255-8.
186. Elmariah, S.B., et al., *Astrocytes regulate inhibitory synapse formation via Trk-mediated modulation of postsynaptic GABAA receptors.* J Neurosci, 2005. **25**(14): p. 3638-50.
187. Min, J.O., et al., *Multi-walled carbon nanotubes change morpho-functional and GABA characteristics of mouse cortical astrocytes.* J Nanobiotechnology, 2015. **13**: p. 92.

188. Gottipati, M.K., et al., *Chemically functionalized water-soluble single-walled carbon nanotubes modulate morpho-functional characteristics of astrocytes.* Nano Lett, 2012. **12**(9): p. 4742-7.
189. Tiryaki, V.M., et al., *Nanofibrillar scaffolds induce preferential activation of Rho GTPases in cerebral cortical astrocytes.* Int J Nanomedicine, 2012. **7**: p. 3891-905.
190. Tiryaki, V.M., et al., *Differentiation of reactive-like astrocytes cultured on nanofibrillar and comparative culture surfaces.* Nanomedicine (Lond), 2015. **10**(4): p. 529-45.
191. Delgado-Rivera, R., et al., *Increased FGF-2 secretion and ability to support neurite outgrowth by astrocytes cultured on polyamide nanofibrillar matrices.* Matrix Biol, 2009. **28**(3): p. 137-47.

# 10. APPENDIX

Articles published/in publication by Martina Chiacchiaretta during the PhD course.

**Martina Chiacchiaretta**°, Mattia Bramini°, Andrea Armirotti, Anna Rocchi, Dipali Digambarrao Kale, Emanuele Giordano, Ester Vázquez, Tiziano Bandiera, Stefano Ferroni, Fabrizia Cesca and Fabio Benfenati. **Internalization of Graphene Nanosheets Leads to Morphological and Functional Alterations in Primary Brain Astrocytes.** (*in preparation*). ° Equal contribution

**M. Chiacchiaretta°,** S. Latifi°, M. Bramini, M. Fadda, A. Fassio, F. Benfenati, F. Cesca. **Neuronal hyperactivity causes $Na^+/H^+$ exchanger-induced extracellular acidification at active synapses.** Journal of Cell Science 2017. ° Equal contribution

F. Jaudon, **M. Chiacchiaretta**, F. Benfenati and F. Cesca. **Kidins220/ARMS is a novel modulator of neurotrophin and calcium signaling in astrocytes** (*in preparation*).

# Neuronal hyperactivity causes $Na^+/H^+$ exchanger-induced extracellular acidification at active synapses

Martina Chiacchiaretta[1,2,‡], Shahrzad Latifi[1,*,‡], Mattia Bramini[1], Manuela Fadda[2], Anna Fassio[1,2], Fabio Benfenati[1,2] and Fabrizia Cesca[1,§]

[1]Center for Synaptic Neuroscience and Technology, Fondazione Istituto Italiano di Tecnologia, Largo Rosanna Benzi 10, Genova 16132, Italy.
[2]Department of Experimental Medicine, University of Genova, Viale Benedetto XV 3, Genova 16132, Italy.
*Present address: Department of Neurology, David Geffen School of Medicine at UCLA, 710 Westwood Plaza, Los Angeles, CA 90095, USA.
‡These authors contributed equally to this work

Extracellular pH impacts on neuronal activity, which is in turn an important determinant of extracellular $H^+$ concentration. The aim of this study was to describe the spatio-temporal dynamics of extracellular pH at synaptic sites during neuronal hyperexcitability. To address this issue we created ex.$E^2$GFP, a membrane-targeted extracellular ratiometric pH indicator that is exquisitely sensitive to acidic shifts. By monitoring ex.$E^2$GFP fluorescence in real time in primary cortical neurons, we were able to quantify pH fluctuations during network hyperexcitability induced by convulsant drugs or high frequency electrical stimulation. Sustained hyperactivity caused a pH decrease that was reversible upon silencing of neuronal activity and located at active synapses. This acidic shift was not attributable to the outflow of synaptic vesicle $H^+$ into the cleft nor to the activity of membrane-exposed $H^+$ V-ATPase, but rather to the activity of the $Na^+/H^+$-exchanger. Our data demonstrate that extracellular synaptic pH shifts take place during

epileptic-like activity of neural cultures, emphasizing the strict links existing between synaptic activity and synaptic pH. This evidence may contribute to the understanding of the physio-pathological mechanisms associated with hyperexcitability in the epileptic brain.

# Kidins220/ARMS is a novel modulator of neurotrophin and calcium signaling in astrocytes

Fanny Jaudon[1], Martina Chiacchiaretta[1, 2], Fabio Benfenati[1, 2] and Fabrizia Cesca[1]

[1] Center for Synaptic Neuroscience, Istituto Italiano di Tecnologia, Genova, Italy
[2] Department of Experimental Medicine, University of Genova, Genova, Italy

## ABSTRACT

Through their ability to modulate synaptic transmission, glial cells are key regulators of neuronal circuits formation and activity. Kidins220/ARMS (Kinase-D interacting substrate of 220 kDa/Ankyrin repeat-rich membrane spanning) is one of the key effector proteins of the neurotrophin pathways in neurons where it is required for differentiation, survival and synaptic plasticity. However, its role in glia remains largely unknown.

Here, we showed that ablation of Kidins220 in astrocytes induces defects in BDNF-dependent TrkB signaling, as well as calcium signalling impairments. Survival and death pathways were also affected, as Kidins220$^{-/-}$ astrocytes displayed (i) impaired proBDNF-dependent activation of NFkB and caspase pathways, and (ii) were more sensitive to genotoxic stress. Furthermore, using neuro-glia co-cultures we showed that wild type neurons grown on Kidins220$^{-/-}$ astrocytes presented dendritic arborization defects and a delayed formation of GABAergic synapses compared to those grown on wild type cells. Altogether, our data reveal a previously unidentified role for astrocyte-expressed Kidins220 in the modulation of survival/death pathways in glial cells, as well as in the control of astrocyte-neuron communication.